



ATLAS CONF Note

ATLAS-CONF-2017-037

27th May 2017



Search for top squark pair production in final states with one isolated lepton, jets, and missing transverse momentum using 36 fb^{-1} of $\sqrt{s} = 13 \text{ TeV}$ pp collision data with the ATLAS detector

The ATLAS Collaboration

The results of a search for the direct pair production of top squarks, the supersymmetric partner of the top-quark, in final states with one isolated electron or muon, several energetic jets, and missing transverse momentum are reported. The search uses data from pp collisions delivered by the Large Hadron Collider in 2015 and 2016 at a centre-of-mass energy of $\sqrt{s} = 13 \text{ TeV}$ and recorded by the ATLAS detector, corresponding to an integrated luminosity of 36 fb^{-1} . A wide range of signal scenarios with different mass splittings between the top squark, the lightest neutralino and possible intermediate SUSY particles is considered, including cases where the W -bosons or the top-quarks produced in the decay chain are off-shell. The analysis also targets spin-0 mediator models, where the mediator decays into a pair of dark matter particles in association with a pair of top-quarks. No significant excess over the Standard Model prediction is observed. The null results are used to set exclusion limits at 95% confidence level in several SUSY benchmark models. For pair-produced top-squarks decaying to top quarks, a top-squark mass up to 940 GeV are excluded. Stringent exclusion limits are also derived for all other considered top-squark decay scenarios. For the spin-0 mediator models, upper limits are set on the visible cross-section.

1 Introduction

The hierarchy problem [1–4] has gained additional attention with the observation of a particle consistent with the Standard Model (SM) Higgs boson [5, 6] at the Large Hadron Collider (LHC) [7]. Supersymmetry (SUSY) [8–16], which extends the SM by introducing supersymmetric partners for every SM degree of freedom, can provide an elegant solution to the hierarchy problem. The partner particles have identical quantum numbers except for a half-unit difference in spin. The superpartners of the left- and right-handed top-quarks, \tilde{t}_L and \tilde{t}_R , mix to form the two mass eigenstates \tilde{t}_1 and \tilde{t}_2 (top squark or stop), where \tilde{t}_1 is the lighter of the two.¹ If the supersymmetric partners of the top-quarks have masses $\lesssim 1$ TeV, loop diagrams involving top-quarks, which are the dominant divergent contribution to the Higgs boson mass, can be largely cancelled [17–24].

Significant mass splitting between the \tilde{t}_1 and \tilde{t}_2 is possible due to the large top-quark Yukawa coupling. Furthermore, effects of the renormalisation group equations are strong for the third-generation squarks, usually driving their masses to significantly lower values than those of the other generations. These considerations suggest a light stop² [25, 26] which, together with the stringent LHC limits excluding other coloured supersymmetric particles up to masses above the TeV level, motivates dedicated stop searches.

SUSY models can violate the conservation of baryon number and lepton number, resulting in a proton lifetime shorter than current experimental limits [27]. This is commonly resolved by introducing a multiplicative quantum number called *R*-parity, which is 1 and -1 for all SM and SUSY particles (sparticles), respectively. A generic *R*-parity-conserving minimal supersymmetric extension of the SM (MSSM) [17, 28–31] predicts pair production of SUSY particles and the existence of a stable lightest supersymmetric particle (LSP).

The charginos $\tilde{\chi}_{1,2}^\pm$ and neutralinos $\tilde{\chi}_{1,2,3,4}^0$ are the mass eigenstates formed from the linear superposition of the charged and neutral SUSY partners of the Higgs and electroweak gauge bosons (higgsinos, winos and binos). They are referred to in the following as electroweakinos. In a large variety of SUSY models, the lightest neutralino ($\tilde{\chi}_1^0$) is the LSP, which is also the assumption throughout this note. The LSP provides a particle DM candidate, as it is stable and interacts only weakly [32, 33].

This note presents a search for direct \tilde{t}_1 pair production in final states with exactly one isolated charged lepton (electron or muon,³ henceforth referred to simply as ‘leptons’) from the decay of either a real or a virtual W -boson. In addition the search requires several jets and a significant amount of missing transverse-momentum \vec{p}_T^{miss} , the magnitude of which is referred to as E_T^{miss} , from the two weakly-interacting LSPs that escape detection. Results are also interpreted in an alternate model where a spin-0 mediator is produced in association with top quarks and subsequently decays to a pair of DM particles.

Searches for direct \tilde{t}_1 pair production have previously been reported by the ATLAS [34–38] and CMS [39–44] collaborations, as well as by the CDF and DØ collaborations (for example refs. [45, 46]) and the LEP collaborations [47]. The exclusion limits obtained by previous ATLAS searches for stop models with massless neutralinos reach ~ 750 GeV for direct two-body decays $\tilde{t}_1 \rightarrow t \tilde{\chi}_1^0$, ~ 300 GeV for the three-body

¹ Similarly the \tilde{b}_1 and \tilde{b}_2 (bottom squark or sbottom) are formed by the superpartners of the bottom-quarks, \tilde{b}_L and \tilde{b}_R .

² The masses of the superpartners of the left-handed bottom-quarks can be as light as the ones of the superpartners of the left-handed top-quarks in certain scenarios as they are both governed mostly by a single mass parameter in SUSY models at tree-level.

³ Electrons and muons from τ decays are included.

process $\tilde{t}_1 \rightarrow bW\tilde{\chi}_1^0$, and ~ 250 GeV for four-body decays $\tilde{t}_1 \rightarrow bff'\tilde{\chi}_1^0$, all at the a 95% confidence level.

2 Search strategy

2.1 Signal models

The experimental signatures of stop pair production can vary dramatically, depending on the spectrum of low-mass SUSY particles. Figure 1 illustrates two typical stop signatures: $\tilde{t}_1 \rightarrow t\tilde{\chi}_1^0$ and $\tilde{t}_1 \rightarrow b\tilde{\chi}_1^\pm$. Other decay and production modes such as $\tilde{t}_1 \rightarrow t\tilde{\chi}_2^0$ and $\tilde{t}_1 \rightarrow t\tilde{\chi}_3^0$, and sbottom direct pair production are also considered in the analysis. The analysis attempts to probe a broad range of the possible scenarios, taking the approach of defining dedicated search regions to target specific but representative SUSY models. The phenomenology of each model is largely driven by the composition of its lightest supersymmetric particles, which are considered to be some combination of the electroweakinos. In practice, this means that the most important parameters of the SUSY models considered are the masses of the electroweakinos and of the colour-charged third generation sparticles.

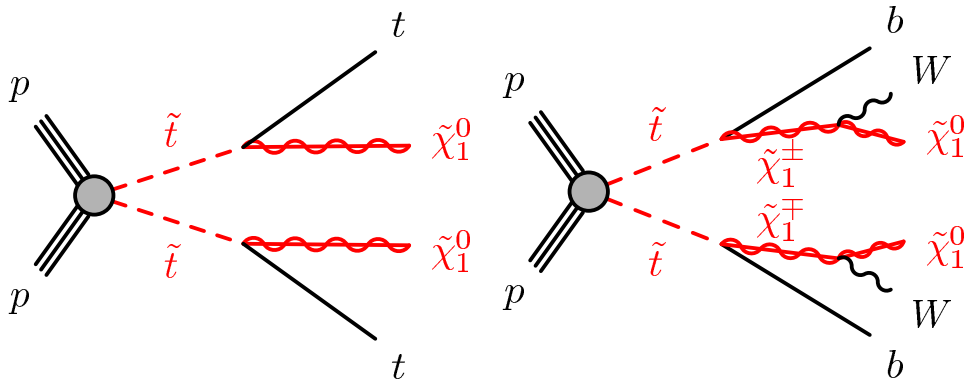


Figure 1: Diagrams illustrating the stop decay modes, which are referred to as (left) $\tilde{t}_1 \rightarrow t\tilde{\chi}_1^0$ and (right) $\tilde{t}_1 \rightarrow b\tilde{\chi}_1^\pm$. Sparticles are shown as red lines. In these diagrams, the charge-conjugate symbols are omitted for simplicity. The direct stop production begins with a top squark-antisquark pair.

In this search, the targeted signal scenarios are either simplified models [48–50], in which the masses of all sparticles are set to high values except for the few sparticles involved in the decay chain of interest, or models based on the phenomenological MSSM (pMSSM) [51, 52], in which all of the 19 pMSSM parameters are set to fixed values, except for two which are scanned. The set of models used are chosen to give a broad coverage of the possible stop decay patterns and phenomenology that can be realised in the MSSM, in order to provide as much as possible a general statement on the sensitivity of the search for direct stop production. Some of the simplified models used are designed with a goal of covering distinct phenomenologically different regions of pMSSM parameter space.

The pMSSM parameters m_{tR} and m_{q3L} specify the \tilde{t}_R and \tilde{t}_L masses, with the smaller of the two controlling the \tilde{t}_1 mass. In models where the \tilde{t}_1 is primarily composed of \tilde{t}_L , the production of light sbottoms (\tilde{b}_1) with a similar mass is also considered. The mass spectrum of electroweakinos and the gluino is given

by the running mass parameters M_1 , M_2 , M_3 , and μ , which set the masses of the bino, wino, gluino, and higgsino, respectively. If several of these parameters are comparably small, the physical LSP will be a mixed state, composed of multiple electroweakinos. Other relevant pMSSM parameters include β , which gives the ratio of vacuum expectation values (VEVs) of the up- and down-type Higgs bosons influencing the preferred decays of the stop, the SUSY breaking scale (M_S) defined as $M_S = \sqrt{m_{\tilde{t}_1} m_{\tilde{t}_2}}$, and the top-quark trilinear coupling (A_t). In addition, a maximal $\tilde{t}_L - \tilde{t}_R$ mixing condition, $X_t/M_S \sim \sqrt{6}$ (where $X_t = A_t - \frac{\mu}{\tan\beta}$), is assumed to obtain a low-mass stop (\tilde{t}_1) while maintaining the models consistent with the observed Higgs boson mass of 125 GeV [53, 54].

In this search, four LSP scenarios⁴ are considered, where each signal scenario is defined by the nature of the LSP: (a) pure bino LSP, (b) bino LSP with a light wino next-to-lightest supersymmetric particle (NLSP), (c) higgsino LSP, and (d) mixed bino/higgsino LSP, which are detailed below with the corresponding sparticle mass spectra illustrated in Figure 2. Complementary searches target scenarios where the LSP is a pure wino (yielding a disappearing track signature [55] common in anomaly-mediated models [56, 57] of SUSY breaking) as well as other LSP hypotheses (such as gauge-mediated models [58–60]), which are not discussed further.

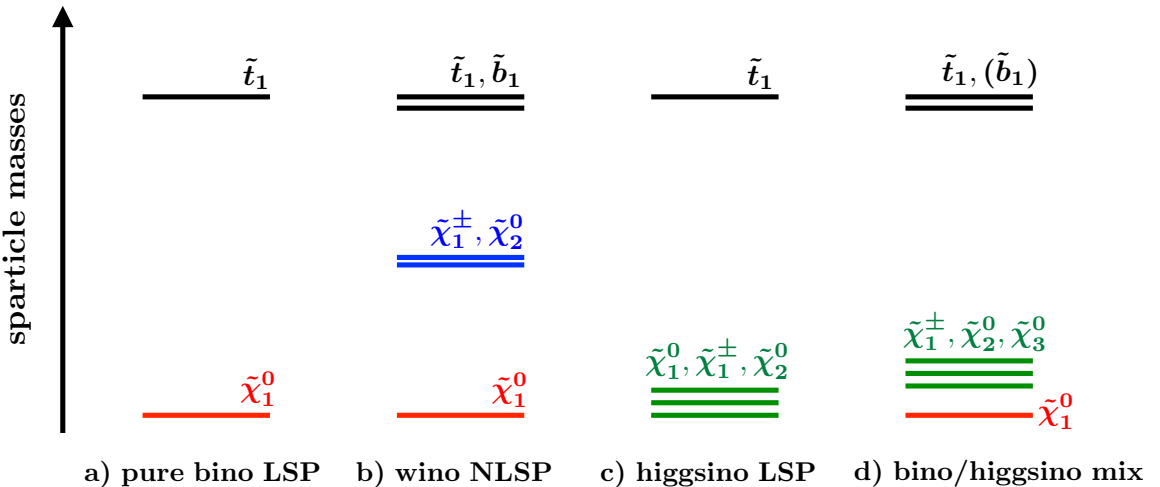


Figure 2: Illustration of the sparticle mass spectrum for various LSP scenarios: a) Pure bino LSP, b) wino NLSP, c) higgsino LSP, and d) bino/higgsino mix. The \tilde{t}_1 and \tilde{b}_1 , shown as black lines, decay to various electroweakino states: the bino state (red lines), wino state (blue lines), or higgsino state (green lines), possibly with the subsequent decay into the LSP. The light sbottom (\tilde{b}_1) is considered only for pMSSM models with $m_{q3L} < m_{tR}$.

(a) Pure bino LSP model:

A simplified model is considered for the scenario where the only light sparticles are the stop (composed mainly of \tilde{t}_R) and the lightest neutralino. When the stop mass is greater than the sum of the top-quark and the LSP masses, the dominant decay channel is via $\tilde{t}_1 \rightarrow t \tilde{\chi}_1^0$. If this decay is kinematically disallowed, the stop can undergo a three-body decay, $\tilde{t}_1 \rightarrow bW \tilde{\chi}_1^0$ when the stop

⁴ For the higgsino LSP scenarios, three sets of model assumptions are considered for the case of a higgsino LSP, each giving rise to different stop BRs for $\tilde{t}_1 \rightarrow b\tilde{\chi}_1^\pm$, $\tilde{t}_1 \rightarrow t\tilde{\chi}_1^0$, and $\tilde{t}_1 \rightarrow t\tilde{\chi}_2^0$.

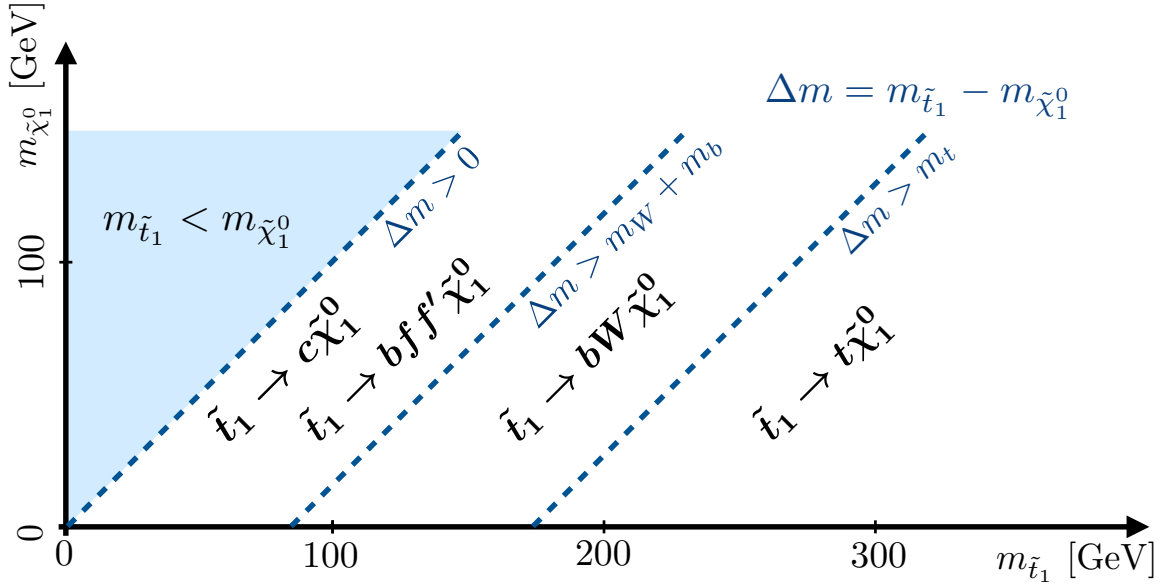


Figure 3: Illustration of the preferred stop decay modes in the plane spanned by the masses of the stop (\tilde{t}_1) and the lightest neutralino ($\tilde{\chi}_1^0$), where the latter is assumed to be the lightest supersymmetric particle. Stop decays to supersymmetric particles other than the lightest supersymmetric particle are not displayed.

mass is above the sum of masses of the bottom-quark, W -boson, and $\tilde{\chi}_1^0$. Otherwise the decay proceeds via a four-body process, $\tilde{t}_1 \rightarrow bff'\tilde{\chi}_1^0$, where f and f' are two distinct fermions, or via a flavour-changing neutral current (FCNC) process, such as the loop-suppressed $\tilde{t}_1 \rightarrow c\tilde{\chi}_1^0$. Given the very different final state, the FCNC decay is not considered further in this search. The various \tilde{t}_1 decay modes in this scenario are illustrated in Figure 3. The region of phase-space along the line of $m_{\tilde{t}_1} = m_{\tilde{\chi}_1^0} + m_t$ is especially challenging to target because of the similarity of the stop signature to the $t\bar{t}$ process, and is referred to in the following as the ‘diagonal region’.

(b) Wino NLSP model:

A pMSSM model is designed such that a wino-like chargino ($\tilde{\chi}_1^\pm$) and neutralino ($\tilde{\chi}_2^0$) are mass-degenerate, with the bino as the LSP. This scenario is motivated by models with gauge unification at the GUT scale such as the cMSSM or mSugra [61–63], where M_2 is assumed to be twice as large as M_1 , leading to the $\tilde{\chi}_1^\pm$ and $\tilde{\chi}_2^0$ having masses nearly twice as large as that of the bino-like LSP.

In this scenario, additional decay modes for the stop (composed mainly of \tilde{t}_L) become relevant, such as the decay to a bottom-quark and the lightest chargino ($\tilde{t}_1 \rightarrow b\tilde{\chi}_1^\pm$) or the decay to a top-quark and the second neutralino ($\tilde{t}_1 \rightarrow t\tilde{\chi}_2^0$). The $\tilde{\chi}_1^\pm$ and $\tilde{\chi}_2^0$ subsequently decay to $\tilde{\chi}_1^0$ via emission of a (potentially off-shell) W -boson or Z /Higgs (h) boson, respectively. The $\tilde{t}_1 \rightarrow b\tilde{\chi}_1^\pm$ decay is considered for a chargino mass above around 100 GeV since the LEP limit on the lightest chargino is $m_{\tilde{\chi}_1^\pm} > 103.5$ GeV [64].

An additional $\tilde{t}_1 \rightarrow b\tilde{\chi}_1^\pm$ decay signal model (simplified model) is designed, motivated by a scenario with close-by masses of the \tilde{t}_1 and $\tilde{\chi}_1^\pm$. The model considered assumes $\Delta m(\tilde{t}_1, \tilde{\chi}_1^\pm) = 10$ GeV and that the top decays via the process $\tilde{t}_1 \rightarrow b\tilde{\chi}_1^\pm$ with a 100% BR. In this scenario the jets originating

from the bottom-quarks are too low-energy (soft) to be reconstructed and hence the signature is characterised by large E_T^{miss} and no jets initiated by bottom quarks (referred to as b -jets).

(c) Higgsino LSP model:

‘Natural’ models of SUSY [23, 24, 65] suggest low-mass stops and a higgsino-like LSP. In such scenarios, the typical mass splitting (Δm) between the LSP and $\tilde{\chi}_1^\pm$ varies between a few hundred MeV to several tens of GeV depending mainly on the mass relation amongst the electroweakinos. For this analysis, a simplified model is designed for various $\Delta m(\tilde{\chi}_1^\pm, \tilde{\chi}_1^0)$ of up to 30 GeV satisfying the mass relation as follows:

$$\Delta m(\tilde{\chi}_1^\pm, \tilde{\chi}_1^0) = 0.5 \times \Delta m(\tilde{\chi}_2^0, \tilde{\chi}_1^0).$$

The stop decays into either $b\tilde{\chi}_1^\pm, t\tilde{\chi}_1^0$, or $t\tilde{\chi}_2^0$, followed by the $\tilde{\chi}_1^\pm$ and $\tilde{\chi}_2^0$ decay through the emission of a highly off-shell W/Z boson. Hence the signature is characterised by low-momentum objects from off-shell W/Z bosons, and the analysis benefits from reconstructing low-momentum leptons (referred to as soft-leptons). The stop decay BR strongly depends on the \tilde{t}_R and \tilde{t}_L composition of the stop. Stops composed mainly of \tilde{t}_R have a large branching fraction to $\tilde{t}_1 \rightarrow b\tilde{\chi}_1^\pm$, whereas stops composed mainly of \tilde{t}_L decay mostly into $t\tilde{\chi}_1^0$ or $t\tilde{\chi}_2^0$. In this search, both scenarios are considered separately.

(d) Bino/higgsino mix model:

The ‘Well-tempered Neutralino’ [66] scenario seeks to provide a viable dark matter candidate while simultaneously addressing the problem of naturalness by targeting a LSP that is an admixture of bino and higgsino. The mass spectrum of the electroweakinos (higgsinos and bino) is expected to be slightly compressed, with a typical mass splitting between the bino and higgsino states of 20-50 GeV. A pMSSM signal model is designed such that low fine-tuning [67, 68] of the pMSSM parameters is satisfied and the annihilation rate of neutralinos is consistent with the observed dark matter relic density⁵ ($0.10 < \Omega h^2 < 0.12$) [69].

The final state produced by many of the models described above is consistent with a $t\bar{t} + E_T^{\text{miss}}$ final state. Exploiting the similarity, signal models with a spin-0 mediator decaying into dark matter particles in association with $t\bar{t}$ are also studied assuming either a scalar (ϕ) or a pseudoscalar (a) mediator, where the couplings to the SM particles can be arranged by mixing with the SM Higgs (or extended Higgs) sector. An example diagram for this process is shown in Figure 4.

2.2 Analysis strategy

The search presented is based on 16 dedicated analyses that target the various scenarios mentioned above. Each of these analyses corresponds to a set of event selection criteria, referred to as a signal region (SR), and is optimised to target one or more signal scenarios. Two different analysis techniques are employed in the definition of the SRs, which are referred to as ‘cut-and-count’ and ‘shape-fit’. The former is based on counting events in a single region of phase-space, while the latter employs SRs split into multiple bins in a specific discriminating kinematic variable. By utilising different signal-to-background ratios in the

⁵ Ω and h are the density parameter and Planck constant, respectively.

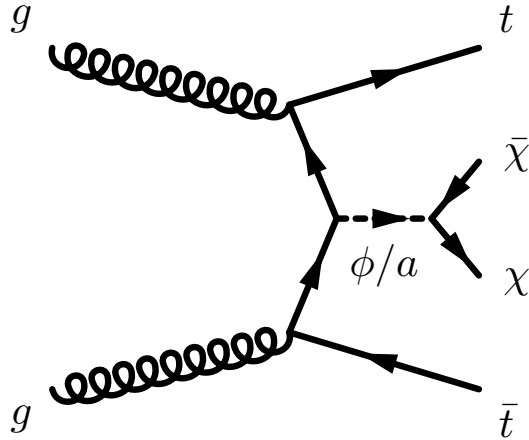


Figure 4: A representative Feynman diagram for s -channel spin-0 mediator production. The ϕ/a is the scalar/pseudoscalar mediator, which decays into a pair of dark matter (χ) particles.

various bins, the search sensitivity is enhanced in challenging scenarios where it is particularly difficult to separate signal from background. The SR selections are described in Section 7.

Specialised techniques are used to enhance the sensitivity of the analyses, such as the reconstruction of hadronically decaying top-quarks from their decay products, and the use of soft-leptons for the higgsino LSP scenario. Sections 5 and 6 describe these and other tools, chosen for their ability to discriminate signal from background. These sections are preceded by descriptions of the ATLAS detector and the dataset upon which this analysis is performed in Section 3, and the corresponding set of simulated samples in Section 4.

The main background processes after the signal selections include $t\bar{t}$, single-top Wt , $t\bar{t} + Z(\rightarrow \nu\bar{\nu})$, and $W + \text{jets}$. Each of those SM processes are estimated by building dedicated control regions (CRs) enhanced in each of the processes, making the analysis more robust against potential mis-modelling effects in simulated events and reducing the uncertainties on the background estimates. The backgrounds are then simultaneously normalised in data for each SR with its associated CRs. The background modelling as predicted by the fits is tested in a series of validation regions (VRs). The background estimation procedure, including the definition of all CRs, is detailed in Section 8.

Systematic uncertainties due to theoretical and experimental effects are considered for all background and signal processes and are described in Section 9. The final results and interpretations, both in terms of model-dependent exclusion limits on the masses of relevant SUSY particles and model-independent upper limits on the number of beyond-SM events, are presented in Section 10.

3 The ATLAS detector and data collection

The ATLAS detector [70] is a multipurpose particle physics detector with nearly 4π coverage in solid angle around the collision point.⁶ It consists of an inner tracking detector (ID), surrounded by a superconducting solenoid providing a 2 T axial magnetic field, a system of calorimeters, and a muon spectrometer (MS) incorporating three large superconducting toroid magnets. The ID provides charged-particle tracking in the range $|\eta| < 2.5$. During the LHC shutdown between Run 1 (2010–2012) and Run 2 (2015–2018), a new innermost layer of silicon pixels was added, which improves the track impact parameter resolution, vertex position resolution and b -tagging performance [71].

High-granularity electromagnetic and hadronic calorimeters cover the region $|\eta| < 4.9$. The central hadronic calorimeter is a sampling calorimeter with scintillator tiles as the active medium and steel absorbers. All the electromagnetic calorimeters, as well as the endcap and forward hadronic calorimeters, are sampling calorimeters with liquid argon as the active medium and lead, copper, or tungsten absorbers.

The MS consists of three layers of high-precision tracking chambers with coverage up to $|\eta| = 2.7$ and dedicated chambers for triggering in the region $|\eta| < 2.4$.

Events are selected by a two-level trigger system [72]: the first level is a hardware-based system and the second is a software-based system.

This analysis is based on a dataset collected in 2015 and 2016 at a collision energy of $\sqrt{s} = 13$ TeV. The data contain an average number of simultaneous pp interactions per bunch crossing, or “pileup”, of approximately 23.7 across the two years. After the application of beam, detector and data quality requirements, the total integrated luminosity is 36.1 fb^{-1} with an associated uncertainty of 3.2%. The uncertainty is derived following a methodology similar to that detailed in Ref. [73] from a preliminary calibration of the luminosity scale using a pair of x – y beam separation scans performed in August 2015 and June 2016.

The events were primarily recorded with a trigger logic that accepts events with $E_{\text{T}}^{\text{miss}}$ above a given threshold. To recover acceptance to signals with moderate $E_{\text{T}}^{\text{miss}}$, events having a well-identified lepton with a minimum p_{T} at trigger level are also accepted for several analyses. In 2015, a $E_{\text{T}}^{\text{miss}}$ threshold of 70 GeV at trigger level was used, while the $E_{\text{T}}^{\text{miss}}$ threshold in 2016 was 90 GeV at the beginning of the data taking period, and raised to 100 GeV and 110 GeV for later periods. In all periods, the trigger is fully efficient for events passing an offline-reconstructed $E_{\text{T}}^{\text{miss}} > 230$ GeV requirement, which is the minimum requirement deployed in the signal regions and control regions relying on the $E_{\text{T}}^{\text{miss}}$ triggers. Events in which the offline reconstructed $E_{\text{T}}^{\text{miss}}$ is measured to be less than 230 GeV are instead collected using single-lepton triggers. The thresholds for the single-lepton triggers are set to obtain a constant efficiency as a function of lepton- p_{T} of $\approx 90\%$ ($\approx 80\%$) for electrons (muons). In 2015, the p_{T} threshold was 24 GeV (20 GeV) for electrons (muons) while it was raised to 26 GeV for both electrons and muons in 2016.

⁶ ATLAS uses a right-handed coordinate system with its origin at the nominal interaction point (IP) in the centre of the detector and the z -axis along the beam pipe. The x -axis points from the IP to the centre of the LHC ring, and the y -axis points upwards. Cylindrical coordinates (r, ϕ) are used in the transverse plane, ϕ being the azimuthal angle around the z -axis. The pseudorapidity is defined in terms of the polar angle θ as $\eta = -\ln \tan(\theta/2)$. Angular distance is measured in units of $\Delta R \equiv \sqrt{(\Delta\eta)^2 + (\Delta\phi)^2}$. The transverse-momentum, p_{T} , is defined with respect to the beam axis (x – y plane).

4 Simulated samples

Samples of Monte Carlo (MC) simulated events are used for the description of the SM background processes and to model the signals. Details of the simulation samples used, including the matrix element (ME) generator and parton distribution function (PDF) set, the parton shower (PS) and hadronisation model, the underlying-event (UE) tune and order of the cross-section calculation, are summarised in Table 1.

Table 1: Overview of the nominal simulated samples. The single-top process includes t -, s -, and Wt channels.

Process	ME generator	ME PDF	PS and hadronisation	UE tune	Cross-section calculation
$t\bar{t}$	POWHEG-Box v2 [74]	CT10 [75]	PYTHIA 6 [76]	P2012 [77]	NNLO+NNLL [78–83]
Single-top	POWHEG-Box v2	CT10	PYTHIA 6	P2012	NNLO+NNLL [84–86]
$V+jets$ ($V = W/Z$)	SHERPA 2.2.0 [87]	NNPDF3.0 [88]	SHERPA	Default	NNLO [89]
Diboson	SHERPA 2.2.1	CT10	SHERPA	Default	NLO
$t\bar{t} + V$	MG5_aMC@NLO 2.2.2 [90]	NNPDF3.0	PYTHIA 8 [91]	A14 [92]	NLO [90]
SUSY signal	MG5_aMC@NLO 2.2 – 2.4	NNPDF2.3 [93]	PYTHIA 8	A14	NLO+NLL [94]
DM signal	MG5_aMC@NLO 2.2.2	NNPDF3.0	PYTHIA 8	A14	NLO

The samples produced with MG5_aMC@NLO [90] and POWHEG [74, 95–98] use EvtGEN v1.2.0 [99] for the modelling of b -hadron decays. The signal samples are all processed with a fast simulation [100], whereas all background samples are processed with the full simulation of the ATLAS detector [100]. All samples are produced with varying numbers of minimum-bias interactions overlaid on the hard-scattering event to simulate the effect of multiple pp interactions in the same or nearby bunch crossings. The number of interactions per bunch crossing is reweighted to match the distribution in data.

4.1 Background samples

The nominal $t\bar{t}$ sample [101] and single-top samples⁷ are calculated to next-to-next-to-leading order (NNLO) with the resummation of soft gluon emission at next-to-next-to-leading-logarithmic (NNLL) accuracy and are generated with POWHEG interfaced to PYTHIA 6 for parton showering and hadronisation. Additional $t\bar{t}$ samples are generated with MG5_aMC@NLO (NLO) interfaced to PYTHIA8, SHERPA, and POWHEG+HERWIG++ [103, 104] for modelling comparisons and evaluation of systematic uncertainties.

Additional samples for $WWbb$, $Wt + b$, and $t\bar{t}$ are generated with MG5_aMC@NLO (LO) interfaced to PYTHIA8, in order to assess the interference effect between the singly and doubly resonant processes as a part of the Wt theoretical modelling systematic uncertainty.

The $t\bar{t}V$ samples are generated with MG5_aMC@NLO (NLO) interfaced to PYTHIA8 for parton showering and hadronisation. SHERPA (NLO) samples are used to evaluate the systematic uncertainties related to the modelling of $t\bar{t}V$ production.

⁷ For the simulation of Wt process, the diagram removal (DR) scheme [102] is used.

4.2 Signal samples

Signal SUSY samples are generated at leading-order (LO) with MG5_aMC@NLO, including up to two extra partons, and interfaced to PYTHIA 8 for parton showering and hadronisation. For the pMSSM models, the sparticle mass spectra are calculated using Softsusy-3.7.3 [105, 106]. The output mass spectrum is then interfaced to HDECAY-3.4 [107] and SDECAY-1.5/1.5a [108] to generate decay tables for each of the sparticles. The decays of the $\tilde{\chi}_2^0$ and $\tilde{\chi}_1^\pm$ via highly off-shell W/Z bosons are computed by taking into account properly the mass of tau leptons and charm-quarks in the low $\Delta m(\tilde{\chi}_1^\pm/\tilde{\chi}_2^0, \tilde{\chi}_1^0)$ regime. The details of the various simulated samples in the four LSP scenarios targeted are given below. The input parameters for the pMSSM models are summarised in Table 2.

(a) Pure bino LSP:

For $\tilde{t}_1 \rightarrow t\tilde{\chi}_1^0$ samples, the stop is decayed in PYTHIA 8 using only phase-space considerations and not the full matrix element (ME). Since the decay products of the samples generated do not preserve the spin information, a polarisation reweighting is applied. For the $\tilde{t}_1 \rightarrow bW\tilde{\chi}_1^0$ and $\tilde{t}_1 \rightarrow bff'\tilde{\chi}_1^0$ samples, the stop is decayed with MadSpin [109], interfaced to PYTHIA 8. MadSpin emulates kinematic distributions such as the mass of the bW system to a good approximation without calculating the full ME. For the MadSpin samples, the stop is assumed to be composed mainly of \tilde{t}_R ($\sim 70\%$), consistent with the pure bino LSP scenario.

(b) Wino NLSP:

In the wino NLSP model, the \tilde{t}_1 is assumed to be composed mainly of \tilde{t}_L (i.e. $m_{q3L} < m_{tR}$). The stop decays into either $b\tilde{\chi}_1^\pm$ with a branching ratio (BR) of about 66%, or $t\tilde{\chi}_2^0$ with a BR of about 33%, followed by $\tilde{\chi}_1^\pm$ and $\tilde{\chi}_2^0$ decays into the LSP, in a large fraction of the phase-space. Since the coupling of \tilde{t}_L to the wino states is larger than the one to the bino state, the stop decay to the bino state ($\tilde{t}_1 \rightarrow t\tilde{\chi}_1^0$) is suppressed. The BRs can be significantly different in the regions of phase-space where one of the decays is kinematically inaccessible. In the case that a mass splitting between the \tilde{t}_1 and $\tilde{\chi}_2^0$ is smaller than the top-quark mass ($\Delta m(\tilde{t}_1, \tilde{\chi}_2^0) < m_t$), for instance, the $\tilde{t}_1 \rightarrow t\tilde{\chi}_2^0$ decay is suppressed, while the $\tilde{t}_1 \rightarrow b\tilde{\chi}_1^\pm$ decay is enhanced. Similarly, the $\tilde{t}_1 \rightarrow b\tilde{\chi}_1^\pm$ decay is suppressed when approaching the boundary of $m_{\tilde{t}_1} = m_b + m_{\tilde{\chi}_1^\pm}$ while increasing the BR for $\tilde{t}_1 \rightarrow t\tilde{\chi}_1^0$.

The signal model is constructed by performing a two-dimensional scan of the pMSSM parameters M_1 and m_{q3L} . For the models considered, $M_3 = 2.2$ TeV and $M_S = 1.2$ TeV are assumed in order to avoid the current gluino and stop mass limits.

The decay mode of the $\tilde{\chi}_2^0$ is very sensitive to the sign of μ , decaying into the lightest Higgs boson and the LSP (with BR $\sim 95\%$) if $\mu > 0$ and decaying into a Z boson and the LSP (with BR $\sim 75\%$) if $\mu < 0$. Hence both μ scenarios are separately considered.⁸

Both stop and sbottom pair production modes are included. Since the stop and sbottom masses are closely related to m_{q3L} , they have roughly the same masses. The sbottom decays largely via $\tilde{b}_1 \rightarrow t\tilde{\chi}_1^\pm$ and $\tilde{b}_1 \rightarrow b\tilde{\chi}_2^0$ with a similar BR for $\tilde{t}_1 \rightarrow b\tilde{\chi}_1^\pm$ and $\tilde{t}_1 \rightarrow t\tilde{\chi}_2^0$, respectively.

⁸ The $\tilde{\chi}_2^0$ decay to the LSP via Z /Higgs boson is kinematically suppressed in the off-shell regime. The $\tilde{\chi}_2^0$ decay is instead determined by the LSP coupling to the squarks. In m_{q3L} scenarios, the sbottom exchange with the large sbottom-bottom-LSP coupling contributes to the $\tilde{\chi}_2^0$ decay, resulting in the $\tilde{\chi}_2^0 \rightarrow b\bar{b}\tilde{\chi}_1^0$ decay with a branching ratio up to 95%.

(c) Higgsino LSP:

For the higgsino LSP case, a simplified model is used with similar input parameters to the wino NLSP pMSSM model except for the electroweakino mass parameters, M_1 , M_2 , and μ , which are changed to satisfy $\mu \ll M_1, M_2$.

The stop decay BRs in scenarios with $m_{tR} < m_{q3L}$ are found to be $\sim 50\%$ for $\tilde{t}_1 \rightarrow b\tilde{\chi}_1^\pm$ and $\sim 25\%$ for both $\tilde{t}_1 \rightarrow t\tilde{\chi}_1^0$ and $\tilde{t}_1 \rightarrow t\tilde{\chi}_2^0$, independent of $\tan \beta$. On the other hand, in scenarios with $m_{q3L} < m_{tR}$ and $\tan \beta = 20$, the $\tilde{t}_1 \rightarrow b\tilde{\chi}_1^\pm$ BR is suppressed to $\sim 10\%$ while $\tilde{t}_1 \rightarrow t\tilde{\chi}_1^0$ and $\tilde{t}_1 \rightarrow t\tilde{\chi}_2^0$ are each increased to $\sim 45\%$. A third scenario with $\tan \beta = 60$ and $m_{q3L} < m_{tR}$ is also studied. In this scenario, the stop BR is found to be $\sim 33\%$ for each of the three decay modes. The $\tilde{\chi}_1^\pm$ and $\tilde{\chi}_2^0$ subsequently decay to the $\tilde{\chi}_1^0$ via a highly off-shell W/Z boson. The exact decay BRs of $\tilde{\chi}_1^\pm$ and $\tilde{\chi}_2^0$ depend on the size of the mass splitting amongst the triplet of higgsino states. For the baseline model, $\Delta m(\tilde{\chi}_1^\pm, \tilde{\chi}_1^0) = 5$ GeV and $\Delta m(\tilde{\chi}_2^0, \tilde{\chi}_1^0) = 10$ GeV are assumed, which roughly corresponds to $M_1 = M_2 \sim 1.2 - 1.5$ TeV. An additional signal model with $\Delta m(\tilde{\chi}_1^\pm, \tilde{\chi}_1^0)$ varying between 0 and 30 GeV is considered.

In the signal generation, the stop decay BR is set to 33% for each of the three decay modes ($\tilde{t}_1 \rightarrow b\tilde{\chi}_1^\pm, \tilde{t}_1 \rightarrow t\tilde{\chi}_2^0, \tilde{t}_1 \rightarrow t\tilde{\chi}_1^0$). The polarisation and stop BRs are reweighted to match the BRs described above for each scenario. Samples were simulated down to $\Delta m(\tilde{\chi}_1^\pm, \tilde{\chi}_1^0) = 2$ GeV for the Δm scan. The $\tilde{t}_1 \rightarrow t\tilde{\chi}_1^0$ samples generated for the pure bino scenario are used in the region below 2 GeV, scaling by the square of BRs to the sum of $\tilde{t}_1 \rightarrow t\tilde{\chi}_1^0$ and $\tilde{t}_1 \rightarrow t\tilde{\chi}_2^0$.

(d) Bino/higgsino mix:

For the well-tempered neutralino, the signal model is built in a similar manner to the wino NLSP model. Signals are generated by scanning in M_1 and m_{q3L} parameter space, with $\tan \beta = 20$, $M_2 = 2.0$ TeV and $M_3 = 1.8$ TeV (corresponding to a gluino mass of ~ 2.0 TeV).⁹ M_S is varied in the range of 700-1300 GeV in the large $\tilde{t}_L - \tilde{t}_R$ mixing regime in order for the lightest Higgs boson to have a mass consistent with the observed mass. Since the dark matter relic density is very sensitive to the mass splitting $\Delta m(\mu, M_1)$, μ is chosen to satisfy $0.10 < \Omega h^2 < 0.12$ given the value of M_1 considered ($-\mu \sim M_1$), which results in $\Delta m(\mu, M_1) = 20 - 50$ GeV.

The dark matter relic density is computed using MicrOMEGAs-4.3.1f [110, 111]. Softsusy-3.3.3 is used to evaluate the level of fine-tuning (Δ) [67] of the pMSSM parameters. The signal models are required to satisfy a low level of fine-tuning corresponding to $\Delta < 100$ (at most 1% fine-tuning).

For scenarios with $m_{tR} < m_{q3L}$, only stop pair production is considered while both stop and sbottom pair production are considered in scenarios with $m_{tR} > m_{q3L}$. The sbottom mass is close to the stop mass as they are both determined mainly by m_{q3L} . The stop and sbottom decay largely into either of higgsino states, $\tilde{\chi}_1^\pm, \tilde{\chi}_2^0$, and $\tilde{\chi}_3^0$ with similar BRs to the higgsino models. The stop and sbottom decay BRs to the bino state are small.

Signal cross-sections for stop/sbottom pair production are calculated to next-to-leading order in the strong coupling constant, adding the resummation of soft gluon emission at next-to-leading-logarithmic accuracy

⁹ The light sbottom and/or stop become tachyonic when their radiative corrections are large in the low m_{q3L} regime, as the correction to squarks is proportional to $(M_3/m_{q3L})^2$, which can change the sign of the physical mass. This is an important consideration when choosing the value of M_3 .

(NLO+NLL) [112–114]. The nominal cross-section and the uncertainty are taken from an envelope of cross-section predictions using different PDF sets and factorisation and renormalisation scales, as described in Ref. [94].

Signal events for the spin-0 mediator model are generated with MG5_aMC@NLO (LO) interfaced to PYTHIA8 using the NNPDF3.0LO PDF. The couplings of the mediator to the DM and SM particles (g_χ and g_v) are assumed to be equal and a common coupling with value $g = g_\chi = g_v = 1$ is used. The kinematics of the decay do not depend strongly on the values of these couplings. The cross-section is computed at NLO [115, 116] and decreases significantly when the mediator is produced off-shell.

Table 2: Overview of the input parameters and typical stop decay branching ratios (BR) for the signal models. Round brackets are used to describe lists of mass parameters scanned. The pMSSM mass parameters (light squark masses) that are not shown below are set to > 3 TeV. The table represents seven different models that are used in the interpretation of the results (two for the wino NLSP, three for the higgsino LSP, and two for the bino/higgsino admixture). For the higgsino LSP scenarios, a simplified model is used instead of a pMSSM model, although the stop decay BRs are based on pMSSM scans with the parameters shown in the table. For the higgsino and bino/higgsino mix scenarios, the stop decay BRs change depending on the $\tilde{t}_L - \tilde{t}_R$ composition of the \tilde{t}_1 , hence the BRs for various scenarios corresponding to (a) $\tilde{t}_1 \sim \tilde{t}_R$ and (b) $\tilde{t}_1 \sim \tilde{t}_L$ (and (c) $\tilde{t}_1 \sim \tilde{t}_L$ with $\tan \beta = 60$ in the higgsino model) are shown separately. For the wino NLSP model, only the $\tilde{t}_1 \sim \tilde{t}_L$ scenario is considered. The sbottom pair production is also considered in $\tilde{b}_1 \sim \tilde{b}_L$ for the wino NLSP and bino/higgsino mix scenarios.

Scenario	Wino NLSP	Higgsino LSP	Bino/higgsino mix
Models	pMSSM	simplified	pMSSM
Mixing parameters		$X_t/M_S \sim \sqrt{6}$	
$\tan \beta$	20	20 or 60	20
M_S [TeV]	0.9-1.2	1.2	0.7-1.3
M_3 [TeV]	2.2	2.2	1.8
Scanned mass parameters	(M_1, m_{q3L})	$(\mu, m_{q3L}/m_{tR})$	$(M_1, m_{q3L}/m_{tR})$
Electroweakino masses [TeV]	$\mu = \pm 3.0$	$M_2 = M_1 = 1.5$	$M_2 = 2.0$
	$M_2 = 2M_1 \ll \mu $	$\mu \ll M_1 = M_2$	$M_1 \sim -\mu, M_1 < M_2$
Additional requirements	–	–	$0.10 < \Omega h^2 < 0.12$
	–	–	$\Delta < 100$
Sbottom pair production	considered	–	considered
\tilde{t}_1 decay modes and their BR [%]	$\tilde{t}_1 \sim \tilde{t}_L$	(a) / (b) / (c)	(a) / (b)
$\tilde{t}_1 \rightarrow t\tilde{\chi}_1^0$	< 5	$\sim 25/\sim 45/\sim 33$	$< 10/< 10$
$\tilde{t}_1 \rightarrow b\tilde{\chi}_1^\pm$	~ 65	$\sim 50/\sim 10/\sim 33$	$\sim 50/\sim 10$
$\tilde{t}_1 \rightarrow t\tilde{\chi}_2^0$	~ 30	$\sim 25/\sim 45/\sim 33$	$\sim 20/\sim 40$
$\tilde{t}_1 \rightarrow t\tilde{\chi}_3^0$	–	–	$\sim 20/\sim 40$
\tilde{b}_1 decay modes and their BR [%]	$\tilde{b}_1 \sim \tilde{t}_L$	–	$\tilde{b}_1 \sim \tilde{b}_L$
$\tilde{b}_1 \rightarrow b\tilde{\chi}_1^0$	< 5	–	< 5
$\tilde{b}_1 \rightarrow t\tilde{\chi}_1^\pm$	~ 65	–	~ 85
$\tilde{b}_1 \rightarrow b\tilde{\chi}_2^0$	~ 30	–	< 5
$\tilde{b}_1 \rightarrow b\tilde{\chi}_3^0$	–	–	< 5

5 Physics object reconstruction

Events must satisfy a series of quality criteria before being considered for further use. The primary vertex, defined as the reconstructed vertex with the highest $\sum_{\text{tracks}} p_{\text{T}}^2$, must have at least two associated tracks with $p_{\text{T}} > 400$ MeV.

Depending on the quality and kinematic requirements imposed, physics objects used are labelled either as *baseline* or *signal*, where the latter describes a subset of the former. Baseline objects are used when classifying overlapping physics objects and to compute the missing transverse-momentum. Baseline leptons (electrons and muons) are also used to apply a veto on events with more than one lepton, which suppresses backgrounds from dileptonic $t\bar{t}$ and Wt decays. Signal objects are used to count each physics object and to construct kinematic discriminating variables needed for the event selection.

Electron candidates are reconstructed from electromagnetic calorimeter cell clusters that are matched to ID tracks. Baseline electrons are required to have $p_{\text{T}} > 5$ GeV, $|\eta| < 2.47$, and to satisfy ‘VeryLoose’ likelihood identification criteria that are defined following the methodology described in Ref. [117]. Signal electrons must pass all baseline requirements and in addition satisfy the ‘LooseAndBLayer’ or ‘Tight’ likelihood identification criteria depending on the signal region selection, and are classified as ‘loose’ or ‘tight’ signal electrons, respectively. They must also have a transverse impact parameter with respect to the reconstructed primary vertex (d_0) that satisfies $|d_0|/\sigma_{d_0} < 5$, where σ_{d_0} is the uncertainty on d_0 , and the distance from this point to the primary vertex along the beam direction (z_0) satisfying $|z_0 \sin \theta| < 0.5$ mm. Furthermore, lepton isolation, defined as the sum of the transverse energy deposited in a cone with a certain radius parameter excluding the energy of the lepton itself, is required. The isolation criteria for ‘loose’ electrons uses only track-based information, obtaining 99% efficiency for signal electrons, independent of p_{T} ; the ‘tight’ electron isolation criteria rely on both track- and calorimeter-based information with a fixed cut on the isolation energy over electron p_{T} .

Muons are reconstructed from combined tracks that are formed from ID and MS tracks, ID tracks matched to MS track segments, standalone MS tracks, or ID tracks matched to an energy deposit in the calorimeter compatible with a minimum-ionising particle (referred to as calo-tagged muon) [118]. Baseline muons up to $|\eta| < 2.7$ are used and they are required to have $p_{\text{T}} > 4$ GeV and to satisfy the ‘Loose’ identification criteria as described in Ref. [119]. Signal muons must pass all baseline requirements and in addition have impact parameters $|z_0 \sin \theta| < 0.5$ mm and $|d_0|/\sigma_{d_0} < 3$, and satisfy the ‘Medium’ identification criteria. Furthermore, signal muons must be isolated according to criteria similar to those used for signal electrons, but with a fixed cut on track-based isolation energy over muon p_{T} . No separation in ‘loose’ and ‘tight’ is performed for signal muons.

Dedicated scale factors for the requirements of identification, impact parameters, and isolation are derived from $Z \rightarrow \ell\ell$ data samples for electrons and muons to correct minor mis-modelling in the MC samples [119, 120]. The p_{T} thresholds of signal leptons are raised to 25 GeV for electrons and muons in all signal regions except those that target higgsino LSP scenarios.

Jet candidates are built from topological clusters [121, 122] in the calorimeters using the anti- k_t algorithm with a jet radius parameter $R = 0.4$ [123]. Jets are corrected for contamination from pileup using the jet area method [124–126] and then calibrated to account for the detector response [127, 128]. Jets in data are further calibrated based on *in situ* measurements of the jet energy scale [129]. Baseline jets are required to have $p_{\text{T}} > 20$ GeV. Signal jets must have $p_{\text{T}} > 25$ GeV and $|\eta| < 2.5$. Furthermore, signal jets with $p_{\text{T}} < 60$ GeV and $|\eta| < 2.4$ are required to satisfy track-based criteria designed to reject jets originating from pileup [126]. Events containing a jet that does not pass specific jet quality

requirements (“jet cleaning”) are vetoed from the analysis in order to suppress detector noise and non-collision backgrounds [130, 131].

Jets containing B -hadrons are identified using the MV2c10 b -tagging algorithm (and those identified are referred to as b -tagged jets), which incorporates quantities such as the impact parameters of associated tracks and reconstructed secondary vertices [132, 133]. The algorithm is used at a working point that provides a 77% b -tagging efficiency in simulated $t\bar{t}$ events, and corresponds to a rejection factor of about 130 for jets originating from light-quark flavours and gluons (light jets) and about 6 for charm-quark induced jets. Jets and associated tracks are also used to identify hadronically decaying τ leptons using the ‘Loose’ identification criteria described in Refs. [128, 134, 135], which has a 60% (50%) efficiency for reconstructing τ leptons decaying into one (three) charged pions. These τ candidates are required to have one or three associated tracks, with total electric charge opposite to that of the selected electron or muon, $p_T > 20$ GeV, and $|\eta| < 2.5$. The τ candidate p_T requirement is applied after a dedicated energy calibration [128, 135].

To avoid labelling the same detector signature as more than one object, an overlap removal procedure is applied. The procedure is tailored for this analysis and optimised using simulation. Table 3 summarises the procedure. Given a set of baseline objects, the procedure checks for overlap based on either a shared track, ghost-matching [125], or a minimal distance¹⁰ ΔR between pairs of objects. For example, if a baseline electron and a baseline jet are found within $\Delta R = 0.2$, then the electron is retained (as stated in the ‘Precedence’ row) and the jet is discarded, unless the jet is b -tagged (as stated in the ‘Condition’ row) in which case the electron is assumed to originate from a heavy-flavor decay and is hence discarded while the jet is retained. If the matching requirement in Table 3 is not met, then both objects under consideration are kept. The order of steps in the procedure is given by the columns in Table 3, which are executed from left to right. The second (ej) and the third (μj) steps of the procedure ensure that leptons and jets have a minimum ΔR separation of 0.2. Jets overlapping with muons that satisfy one or more of the following conditions are not considered in the third step: the jet is b -tagged, the jet contains more than three tracks ($n_{\text{track}}^j > 3$), or the ratio of jet p_T to muon p_T satisfies $\frac{p_T^j}{p_T^\mu} < 0.7$. Therefore, the fourth step (ℓj) is applied to only the jets that satisfy the above criteria or that are well separated from leptons with $\Delta R > 0.2$. For the remainder of the note, all baseline and signal objects are those that have passed the overlap removal procedure.

The missing transverse-momentum is reconstructed from the negative vector sum of the transverse-momenta of baseline electrons, muons, jets, and a soft term built from high-quality tracks that are associated with the primary vertex but not with the baseline physics objects [136, 137]. Photons and hadronically decaying τ leptons are not explicitly included but enter either as jets, electrons, or via the soft term.

6 Discriminating variables

The background processes contributing to a final state with one isolated lepton, jets and E_T^{miss} are primarily semi-leptonically decaying (semi-leptonic) $t\bar{t}$ events and W +jets events. Both backgrounds can be effectively reduced by requiring the transverse mass of the event, m_T ,¹¹ to be larger than the W -boson

¹⁰ Rapidity ($y \equiv \frac{1}{2} \ln \left(\frac{E+p_Z}{E-p_Z} \right)$) is used instead of pseudo-rapidity (η) when computing ΔR in the overlap removal procedure.

¹¹ The transverse mass m_T is defined as $m_T^2 = 2p_T^\ell E_T^{\text{miss}}[1 - \cos(\Delta\phi)]$, where $\Delta\phi$ is the azimuthal angle between the lepton and the missing transverse-momentum direction. The quantity p_T^ℓ is the transverse-momentum of the charged lepton.

Table 3: Overlap removal procedure for physics objects. The first two rows list the types of overlapping objects: electron (e), muon (μ), electron or muon (ℓ), jet (j), and hadronically decaying τ lepton (τ). All objects refer to the baseline definitions, except for τ where no distinction between baseline and signal definition is made. The third row specifies when an object pair is considered to be overlapping. The fourth row describes an optional condition which must be met in addition for the pair of objects to be considered overlapping. The last row lists the precedence object. Object 1 is retained and Object 2 is discarded if the condition is not met, and vice versa. More information is given in the text.

Object 1	e	e	μ	j	e
Object 2	μ	j	j	ℓ	τ
Matching criteria	shared track	$\Delta R < 0.2$	ghost-matched	$\Delta R < \min\left(0.4, 0.04 + \frac{10}{p_T^\ell/\text{GeV}}\right)$	$\Delta R < 0.1$
Condition	calo-tagged μ	j not b -tagged	$\begin{aligned} &j \text{ not } b\text{-tagged and} \\ &\left(n_{\text{track}}^j < 3 \text{ or } \frac{p_T^\mu}{p_T^j} > 0.7\right) \end{aligned}$	–	–
Precedence	e	e	μ	j	e

mass. In most signal regions, the dominant background after this requirement arises from di-leptonically decaying (dileptonic) $t\bar{t}$ events, in which one lepton is not identified, is outside the detector acceptance, or is a hadronically decaying τ lepton. On the other hand, the m_T selection is not applied in the signal regions targeting the higgsino LSP scenarios, hence the background is dominated by the semi-leptonic $t\bar{t}$ process. A series of additional variables described below are used to discriminate between the $t\bar{t}$ background and the signal processes.

6.1 Common discriminating variables

The asymmetric m_{T2} (am_{T2}) [138–141] and m_{T2}^τ are both variants of the variable m_{T2} [142], a generalisation of the transverse mass applied to signatures where two particles are not directly detected. The am_{T2} variable targets dileptonic $t\bar{t}$ events where one lepton is not reconstructed, while the m_{T2}^τ variable targets $t\bar{t}$ events where one of the two W -bosons decays via a hadronically decaying τ lepton. In addition, the $H_{T,\text{sig}}^{\text{miss}}$ variable is used in some signal regions to reject background processes without invisible particles in the final state. It is defined as follows.

$$H_{T,\text{sig}}^{\text{miss}} = \frac{|\vec{H}_T^{\text{miss}}| - M}{\sigma_{|\vec{H}_T^{\text{miss}}|}},$$

where \vec{H}_T^{miss} is the negative vectorial sum of the momenta of the signal jets and signal lepton. The denominator is computed from the per-event jet energy uncertainties, while the lepton is assumed to be well-measured. The offset parameter M , which is a characteristic scale of the background processes, is fixed at 100 GeV in this analysis. These variables are detailed in Ref. [36]. Figure 5 show distributions of the am_{T2} and $H_{T,\text{sig}}^{\text{miss}}$ variables.

Reconstructing the hadronic top-quark decay (top-tagging) can provide additional discrimination against dileptonic $t\bar{t}$ events, which do not contain a hadronically decaying top-quark. In events where the top-quark is produced with moderate p_T , a χ^2 technique is used to reconstruct candidate hadronic top-quark decays. For every selected event with four jets of which at least one is b -tagged, the m_{top}^χ variable is defined as the invariant mass of the three jets in the event most compatible with the hadronic decay products of

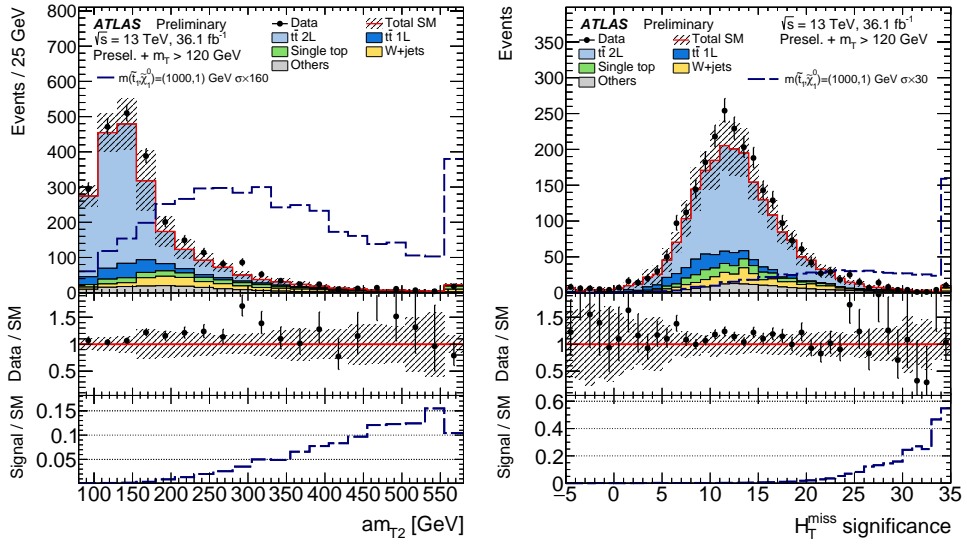


Figure 5: Distributions of discriminating variables: (left) am_{T2} and (right) $H_{T,\text{sig}}^{\text{miss}}$ after the high- E_T^{miss} preselection shown in Table 4 and $m_T > 120 \text{ GeV}$. In addition to the SM background prediction, a bino LSP signal model is shown for a stop mass of 1 TeV, with a neutralino mass of 1 GeV, in the main figure this component is scaled up for visibility. and scaled by a certain factor for visibility. The lower panels show the ratio of data over total SM background and the signal expectation over total SM background. The category labelled ‘Others’ stands for minor SM backgrounds that contribute less than 5% of the total SM background. The hashed area around the total SM prediction and the hashed band in the Data/SM ratio include statistical and experimental uncertainties. The last bin contains overflows.

a top-quark, where the three jets are selected by a χ^2 -minimisation using the jet momenta and energy resolutions.

After reconstructing the hadronic top-quark through the χ^2 -minimisation, the remaining b -tagged jet¹² is paired with the lepton to reconstruct the leptonic top-quark. Based on these objects, the azimuthal separation between the hadronic and leptonic top-quark candidates, $\Delta\phi(t_{\text{had}}^{\chi}, t_{\text{lep}}^{\chi})$ and between the $\vec{p}_{\text{T}}^{\text{miss}}$ and the hadronic top-quark candidate, $\Delta\phi(\vec{p}_{\text{T}}^{\text{miss}}, t_{\text{had}}^{\chi})$, are defined.

An alternate top-tagging method is used to target events where the top-quark is produced with a significant boost. The top-quark candidates are reconstructed by considering all small-radius jets in the event and clustering them into large-radius jets using the anti- k_t algorithm with a radius parameter $R_0 = 3.0$. The radius of each jet is then iteratively reduced to an optimal radius, $R(p_{\text{T}}) = 2 \times m_{\text{top}}/p_{\text{T}}$, that matches their p_{T} . If a candidate loses a large fraction of p_{T} in the shrinking process, it is discarded. In events where two or more top-quark candidates are found, the one with the mass closest to the top-quark mass is taken. The same algorithm is also used to define boosted hadronic W -boson candidates, where only non- b -tagged jets are considered, and the mass of the W -boson is used to define the optimal radius. The masses of the reclustered top-quark and W -boson candidates are referred to as $m_{\text{top}}^{\text{reclustered}}$ and $m_W^{\text{reclustered}}$, respectively.

The $\vec{p}_{\text{T}}^{\text{miss}}$ in semi-leptonic $t\bar{t}$ events is expected to closely align with the direction of the leptonic top-quark. After boosting the leptonic top-quark and the $\vec{p}_{\text{T}}^{\text{miss}}$ into the $t\bar{t}$ rest frame, the magnitude of the perpendicular component of the $\vec{p}_{\text{T}}^{\text{miss}}$ with respect to the leptonic top-quark is computed. This $E_{\text{T},\perp}^{\text{miss}}$ is

¹² In case that the event has exactly one b -tagged jet, the highest- p_{T} jet is used instead of the second b -tagged jet.

expected to be small for the background, as the dominant contribution to the total E_T^{miss} is due to the neutrino emitted in the leptonic top-quark decay.

6.2 Discriminating variables for BDTs

In the diagonal region where $m_{\tilde{t}_1} \approx m_t + m_{\tilde{\chi}_1^0}$, the momentum transfer from the \tilde{t}_1 to the $\tilde{\chi}_1^0$ is small, and the stop signal has very similar kinematics to the $t\bar{t}$ process. In order to achieve good separation between $t\bar{t}$ and signal, a boosted decision tree (BDT) implemented in the TMVA framework [143] is used. Additional discriminating variables are developed to use as inputs to the BDT, or as a part of the preselection in the BDT analyses.

Some of the selections targeting the diagonal region in the pure bino LSP scenarios rely on the presence of high- p_T initial state radiation (ISR) jets, which serves to boost the di-stop system. A powerful technique to discriminate these signal models from the $t\bar{t}$ background is to attempt to reconstruct the transverse-momentum ratio between the di-neutralino system and the di-stop system. This ratio α can be directly related to the ratio of the masses of the \tilde{t}_1 and the $\tilde{\chi}_1^0$ [144, 145]:

$$\alpha \equiv \frac{m_{\tilde{\chi}_1^0}}{m_{\tilde{t}_1}} \sim \frac{p_T(\tilde{\chi}_1^0 \tilde{\chi}_1^0)}{p_T(\tilde{t}_1 \tilde{t}_1)}.$$

In the 1-lepton channel, the observed E_T^{miss} will also include a contribution from the neutrino produced in the leptonic W -boson decay, in addition to that due to the LSPs. A light $\tilde{\chi}_1^0$ and a \tilde{t}_1 mass close to the mass of the top-quark will result in the neutralinos having low momenta, making the reconstruction of the neutrino momentum and its subtraction from the \vec{p}_T^{miss} vital. In the signal region targeting this scenario, a modified χ^2 -minimisation using jet momenta only is applied to define the hadronic top candidate $t_{\text{had}}^{\text{ISR}}$. One or two light jets and one b -jet are selected in such a way that they are most compatible with originating from hadronic W -boson and top-quark decays. The leading- p_T light jet is excluded, as it is assumed to originate from ISR.

Out of the two jets with the highest probabilities of being a b -jet according to the b -tagging algorithm, the one not assigned to $t_{\text{had}}^{\text{ISR}}$ is assigned to the leptonic top-quark candidate, together with the lepton. For the determination of the neutrino momentum, two hypotheses are considered: that of a $t\bar{t}$ event and that of a signal event. For the $t\bar{t}$ hypothesis, the entire \vec{p}_T^{miss} is attributed to the neutrino. Under the signal hypothesis, collinearity of each \tilde{t}_1 with both of its decay products is assumed. This results in the transverse-momentum vector of the neutrino from the leptonic W -boson decay being calculable by subtracting the momenta of the LSPs from \vec{p}_T^{miss} , when assuming a specific mass ratio α :

$$\vec{p}_T(\nu^\alpha) = (1 - \alpha)\vec{p}_T^{\text{miss}} - \alpha\vec{p}_T(t_{\text{had}}^{\text{ISR}} + b_{\text{lep}} + \ell)$$

where ν^α is the neutrino under the α assumption, b_{lep} is the b candidate assigned to the semi-leptonic top-quark candidate and ℓ is the charged lepton. The resulting momentum of ν^α is then used to calculate further variables under the signal hypothesis, like the leptonic W -boson transverse mass m_T^α or the mass of the top-quark candidate including the leptonic W -boson decay $m(t_{\text{lep}}^\alpha)$. The lepton pseudorapidity is used as a proxy for the neutrino pseudorapidity in the calculation. Further variables are the difference in m_T between the calculation under the hypothesis of a $t\bar{t}$ event and under the signal hypothesis, $\Delta m_T^\alpha = m_T - m_T^\alpha$, where m_T^α uses the lepton and ν^α , and the p_T of the reconstructed $t\bar{t}$ system under the SM hypothesis,

$p_T(t\bar{t})$. The mass ratio $\alpha = 0.135$ is used throughout the note, as is calculated from $m_{\tilde{t}_1} = 200$ GeV and $m_{\tilde{\chi}_1^0} = 27$ GeV.

Larger stop-mass values in compressed bino LSP scenarios boost the $\tilde{\chi}_1^0$ such that neglecting the neutrino momentum in the determination of α is a good approximation. A recursive jigsaw reconstruction (RJR) technique [146] is used to divide each event into an ISR hemisphere and a sparticle (S) hemisphere, where the latter contains both the invisible (I) and visible (V) decay products of the stops. Objects are grouped together based on their proximity in the lab frame's transverse plane by maximising the p_T of the S and ISR hemispheres over all choices of object assignment. In events with high- p_T ISR jets, the axis of maximum back-to-back p_T , also known as the thrust axis, should approximate the direction of the ISR and the di-stop system's back-to-back recoil.

The RJR variables used in the corresponding signal regions are the transverse mass of the S system, M_T^S , the ratio of the momenta of the I and ISR systems, R_{ISR} (an approximation of α), the azimuthal separation between the momenta of the ISR and I systems, $\Delta\phi(\text{ISR}, \text{I})$, and the number of jets assigned to the V system, N_j^V .

Figure 6 and 7 show example kinematic distributions of the variables used for the BDT trainings.

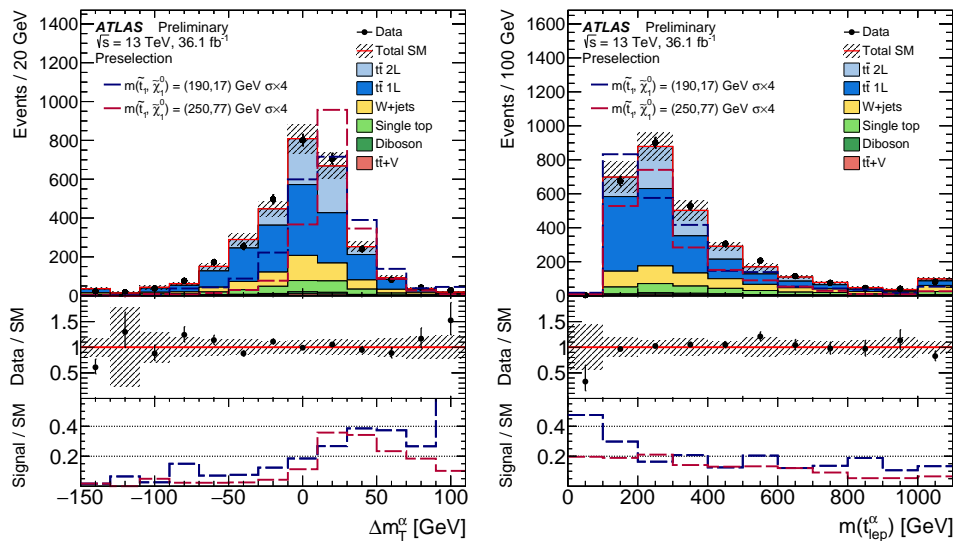


Figure 6: Distributions of discriminating variables: (left) Δm_T^α and (right) $m(t_{\text{lep}}^\alpha)$. They are used in the tN_{diag_low} signal region, which is defined in Section 7.1.2. Preselection refers to the signal region selection but without any requirements on the BDT output score. In addition to the SM background prediction, signal models are shown, denoted by $m(\tilde{t}_1, \tilde{\chi}_1^0)$, and scaled by a factor of four for visibility. The lower panels show the ratio of data over total SM background and the signal expectation over total SM background. The hashed area around the total SM prediction and the hashed band in the Data/SM ratio include statistical and experimental uncertainties. The last bin contains overflows.

7 Signal selections

Signal region (SR) selections are optimised using simulated MC event samples. The metric of the optimisation is the discovery sensitivity for the various decay modes and for different regions of SUSY

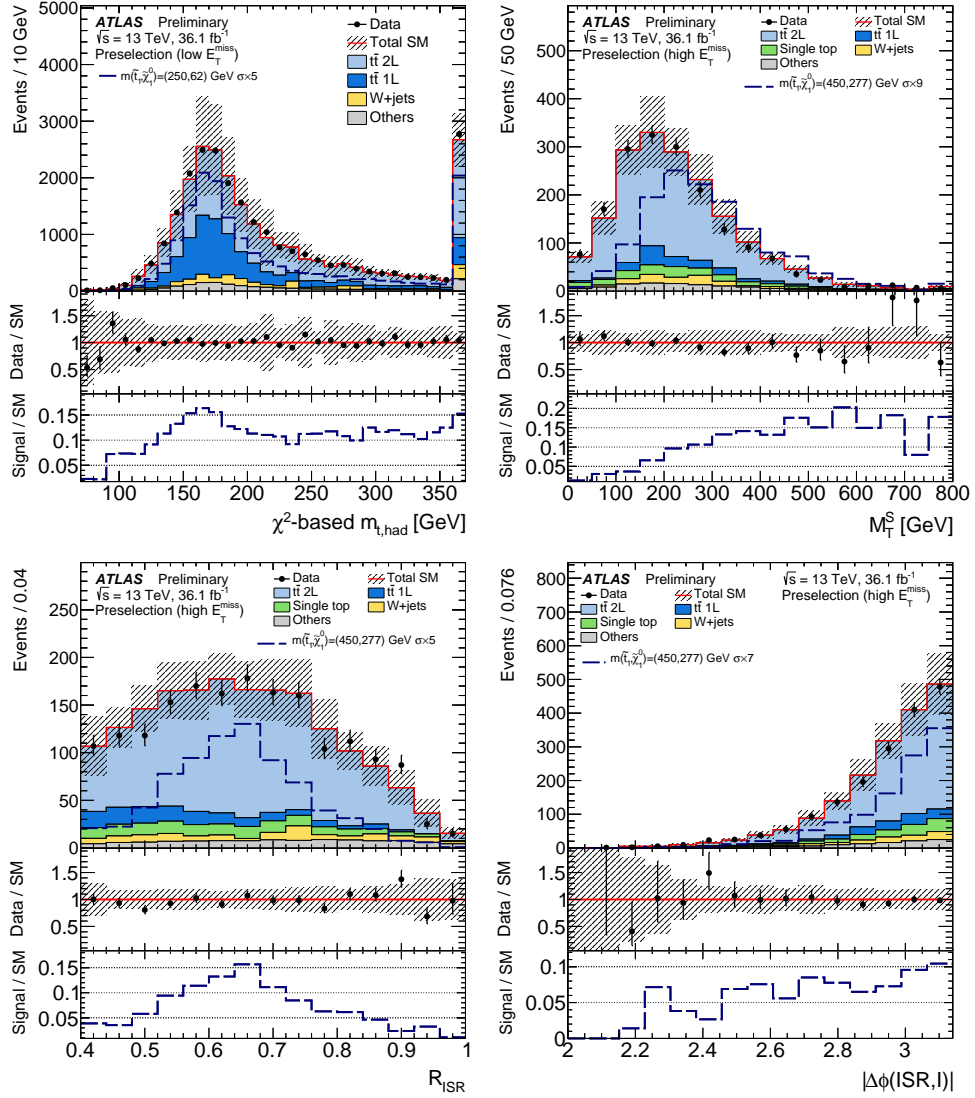


Figure 7: Distributions of discriminating variables: (top left) reconstructed mass of the hadronic top-quark with χ^2 -based minimisation method (m_{top}^χ), (top right) M_T^S , (bottom left) R_{ISR} , and (bottom right) $\Delta\phi(\text{ISR}, \text{I})$. The m_{top}^χ is used in the `tN_diag_med` and the others used in the `tN_diag_high` signal region, which are defined in Section 7.1.2. In addition to the SM background prediction, signal models are shown, denoted by $m(\tilde{t}_1, \tilde{\chi}_1^0)$, and scaled by a certain factor for visibility. The lower panels show the ratio of data over total SM background and the signal expectation over total SM background. The category labelled ‘Others’ stands for minor SM backgrounds that contribute less than 5% of the total SM background. The hashed area around the total SM prediction and the hashed band in the Data/SM ratio include statistical and experimental uncertainties. The last bin contains overflows.

parameter space and masses in the spin-0 mediator models. A set of benchmark signal models, selected to cover the various stop and spin-0 mediator scenarios, was used for the optimisation. The optimisations of signal-region selections were performed using an iterative algorithm and considering all studied discriminant variables, accounting for statistical and systematic uncertainties.

All events are required to have exactly one signal lepton (except for the $t\bar{t}Z(\rightarrow \ell\ell)$ control regions, where three signal leptons are required), no additional baseline leptons, and at least four signal jets (two jets in several SRs). In most cases, at least one b -tagged jet is also required. A set of preselection criteria (high- E_T^{miss} , low- E_T^{miss} , and soft-lepton) is defined for monitoring the MC modelling of the kinematic variables. The preselection criteria are also used as the starting point for the SR optimisation.

In the SRs relying on only the E_T^{miss} trigger, all events are required to have $E_T^{\text{miss}} > 230 \text{ GeV}$ to ensure that the trigger is fully efficient. In SRs that use a combination of E_T^{miss} and lepton triggers, this requirement is relaxed to $E_T^{\text{miss}} > 100 \text{ GeV}$. In order to reject multijet events, requirements are imposed on the transverse mass (m_T) and the azimuthal angles between the leading and sub-leading jets and $E_T^{\text{miss}} (|\Delta\phi(\text{jet}_i, \vec{p}_T^{\text{miss}})|)$ in most of SRs. For events with hadronic τ candidates, the requirement $m_{T2}^{\tau} > 80 \text{ GeV}$ is applied.

The exact preselection criteria can be found in Table 4. $|\Delta\phi(\text{jet}_i, \vec{p}_T^{\text{miss}})|$ and m_{T2}^{τ} are not included in the preselections, but are often used to define SRs. Figure 8 shows various relevant kinematic distributions at preselection level. The backgrounds are normalised to the theoretical cross-sections, except for in the E_T^{miss} distribution where the $t\bar{t}$ events are scaled with normalisation factors obtained from a simultaneous likelihood fit of the CRs, described in Section 10.

Table 4: Preselection criteria used for the high- E_T^{miss} signal regions (left), the low- E_T^{miss} signal regions (middle) and the soft-lepton signal regions (right). For the soft-lepton selection, $p_T \geq 5 \text{ GeV}$ is required for electrons. Round brackets are used to describe lists of values.

Selection	high- E_T^{miss}	low- E_T^{miss}	soft-lepton
Trigger	E_T^{miss} triggers only	E_T^{miss} and lepton triggers	E_T^{miss} triggers only
Data quality		jet cleaning, primary vertex	
Second lepton veto		no additional baseline leptons	
Number of leptons, tightness	= 1 ‘loose’ lepton	= 1 ‘tight’ lepton	= 1 ‘tight’ lepton
Lepton p_T [GeV]	≥ 25	≥ 27	≥ 4 for μ ≥ 5 for e
Number of (jets, b -tags)	$(\geq 2, \geq 0)$	$(\geq 4, \geq 1)$	$(\geq 2, \geq 1)$
Jet p_T [GeV]	$> (25, 25)$	$> (50, 25, 25, 25)$	$> (25, 25)$
E_T^{miss} [GeV]	> 230	> 100	> 230
m_T [GeV]	> 30	> 90	–

Table 5 summarises all SRs with a brief description of the targeted signal scenarios. For the pure bino LSP scenario, seven SRs are developed in total. Five SRs target the $\tilde{t}_1 \rightarrow t\tilde{\chi}_1^0$ decay. The corresponding SR labels begin with tN , which is an acronym for ‘top neutralino’. Additional text in the label describes the stop mass region. For example, tN_diag targets the diagonal region where $m_{\tilde{t}_1} \sim m_{\tilde{\chi}_1^0} + m_t$. The third part of the labels **low**, **med**, and **high** denote the targeted stop mass range, relative to other regions of the same type (for example, tN_diag_low targets a stop mass of 190 GeV, while tN_diag_high is

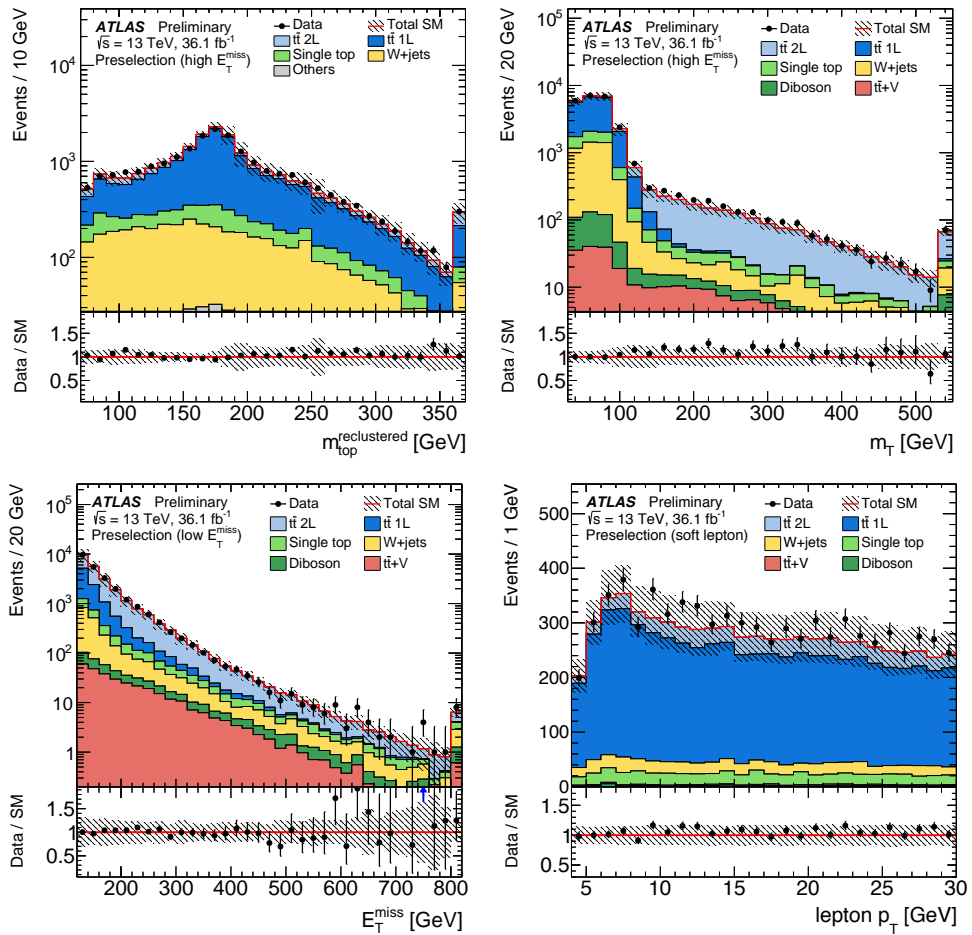


Figure 8: Various kinematic distributions after the preselection: (top left) mass of the hadronic top-quark candidate with the recursive reclustering method ($m_{\text{top}}^{\text{reclustered}}$) after the high- $E_{\text{T}}^{\text{miss}}$ preselection, (top right) m_{T} after the high- $E_{\text{T}}^{\text{miss}}$ preselection, (bottom left) $E_{\text{T}}^{\text{miss}}$ after the low- $E_{\text{T}}^{\text{miss}}$ preselection, and (bottom right) lepton p_{T} after the soft-lepton preselection. The SM background predictions are normalised to the theoretical cross-sections (pre-fit), except for in the $E_{\text{T}}^{\text{miss}}$ distribution, where the $t\bar{t}$ events are scaled by the normalisation factors obtained from a simultaneous likelihood fit of the CRs. The category Others in the top left panel stands for the sum of minor SM backgrounds that contribute less than 5% of the total SM background. The hashed area around the total SM prediction and the hashed band in the Data/SM ratio include statistical and experimental uncertainties. The last bin contains overflows, except for the lepton p_{T} distribution.

optimised for $m_{\tilde{t}_1} = 450$ GeV). Furthermore, two additional SRs labelled bWN and bffN are dedicated to the three-body ($\tilde{t}_1 \rightarrow bW\tilde{\chi}_1^0$) and four-body ($\tilde{t}_1 \rightarrow bff'\tilde{\chi}_1^0$) decay searches, respectively.

Six SRs target various $\tilde{t}_1 \rightarrow b\tilde{\chi}_1^{\pm}$ scenarios where the SR labels follow the same logic: the first two characters bC stand for ‘bottom chargino’. The consecutive labels, 2x, bv, or soft, denote the targeted electroweakino spectrum. For the wino NLSP scenario, three SRs are designed with the label bC2x denoting the mass relation $m_{\tilde{\chi}_1^{\pm}} \sim 2 \times m_{\tilde{\chi}_1^0}$ in the signal model. The label bC bv is used for the no b -tagged jets (b -veto) SR. For the higgsino LSP scenario, three SRs are labelled as bCsoft because their selections explicitly target soft-lepton signatures.

Finally, three SRs labelled as DM target the spin-0 mediator scenario, with the consecutive labels, low and

Table 5: Overview of all signal regions together with the targeted signal scenario, benchmarks used for the optimisation (with particle masses given in units of [GeV]), the analysis technique used for model-dependent exclusions, and a reference to the table with the event selection details. For the wino NLSP scenario, sbottom pair production (not shown) is also considered.

SR	Signal scenario	benchmark	Exclusion technique	Table
tN_med	Pure bino LSP ($\tilde{t}_1 \rightarrow t\tilde{\chi}_1^0$)	$m(\tilde{t}_1, \tilde{\chi}_1^0) = (600, 300)$	shape-fit (E_T^{miss})	6
tN_high	Pure bino LSP ($\tilde{t}_1 \rightarrow t\tilde{\chi}_1^0$)	$m(\tilde{t}_1, \tilde{\chi}_1^0) = (1000, 1)$	cut-and-count	6
tN_diag_low	Pure bino LSP ($\tilde{t}_1 \rightarrow t\tilde{\chi}_1^0$)	$m(\tilde{t}_1, \tilde{\chi}_1^0) = (190, 17)$	BDT cut-and-count	7
tN_diag_med	Pure bino LSP ($\tilde{t}_1 \rightarrow t\tilde{\chi}_1^0$)	$m(\tilde{t}_1, \tilde{\chi}_1^0) = (250, 62)$	BDT shape-fit	7
tN_diag_high	Pure bino LSP ($\tilde{t}_1 \rightarrow t\tilde{\chi}_1^0$)	$m(\tilde{t}_1, \tilde{\chi}_1^0) = (450, 277)$	BDT shape-fit	7
bWN	Pure bino LSP ($\tilde{t}_1 \rightarrow bW\tilde{\chi}_1^0$)	$m(\tilde{t}_1, \tilde{\chi}_1^0) = (350, 230)$	shape-fit (am_{T2})	8
bffN	Pure bino LSP ($\tilde{t}_1 \rightarrow bff'\tilde{\chi}_1^0$)	$m(\tilde{t}_1, \tilde{\chi}_1^0) = (400, 350)$	shape-fit ($p_T^\ell/E_T^{\text{miss}}$)	8
bC2x_med	Wino NLSP ($\tilde{t}_1 \rightarrow b\tilde{\chi}_1^\pm, \tilde{t}_1 \rightarrow t\tilde{\chi}_2^0$)	$m(\tilde{t}_1, \tilde{\chi}_1^\pm, \tilde{\chi}_2^0) = (750, 300, 150)$	cut-and-count	9
bC2x_diag	Wino NLSP ($\tilde{t}_1 \rightarrow b\tilde{\chi}_1^\pm, \tilde{t}_1 \rightarrow t\tilde{\chi}_2^0$)	$m(\tilde{t}_1, \tilde{\chi}_1^\pm, \tilde{\chi}_2^0) = (650, 500, 250)$	cut-and-count	9
bCbv	Wino NLSP ($\tilde{t}_1 \rightarrow b\tilde{\chi}_1^\pm, \tilde{t}_1 \rightarrow t\tilde{\chi}_2^0$)	$m(\tilde{t}_1, \tilde{\chi}_1^\pm, \tilde{\chi}_2^0) = (700, 690, 1)$	cut-and-count	9
bCsoft_diag	Higgsino LSP ($\tilde{t}_1 \rightarrow t\tilde{\chi}_1^0, \tilde{t}_1 \rightarrow t\tilde{\chi}_2^0, \tilde{t}_1 \rightarrow b\tilde{\chi}_1^\pm$)	$m(\tilde{t}_1, \tilde{\chi}_1^\pm, \tilde{\chi}_2^0) = (400, 355, 350)$	shape-fit ($p_T^\ell/E_T^{\text{miss}}$)	10
bCsoft_med	Higgsino LSP ($\tilde{t}_1 \rightarrow t\tilde{\chi}_1^0, \tilde{t}_1 \rightarrow t\tilde{\chi}_2^0, \tilde{t}_1 \rightarrow b\tilde{\chi}_1^\pm$)	$m(\tilde{t}_1, \tilde{\chi}_1^\pm, \tilde{\chi}_2^0) = (600, 205, 200)$	shape-fit ($p_T^\ell/E_T^{\text{miss}}$)	10
bCsoft_high	Higgsino LSP ($\tilde{t}_1 \rightarrow t\tilde{\chi}_1^0, \tilde{t}_1 \rightarrow t\tilde{\chi}_2^0, \tilde{t}_1 \rightarrow b\tilde{\chi}_1^\pm$)	$m(\tilde{t}_1, \tilde{\chi}_1^\pm, \tilde{\chi}_2^0) = (800, 155, 150)$	shape-fit ($p_T^\ell/E_T^{\text{miss}}$)	10
DM_low_loose	spin-0 mediator	$m(\Phi/a, \chi) = (20, 1)$	cut-and-count	11
DM_low	spin-0 mediator	$m(\Phi/a, \chi) = (20, 1)$	cut-and-count	11
DM_high	spin-0 mediator	$m(\Phi/a, \chi) = (300, 1)$	cut-and-count	11

`low_loose` for low mediator masses and `high` for high mediator masses.

With the exception of the tN and bCsoft regions, the above SRs are not designed to be mutually exclusive. A dedicated combined fit is performed using tN_med and bCsoft_med (or bCsoft_high) in the higgsino LSP and well-tempered scenarios in order to improve exclusion sensitivity. The SRs with the requirement of lepton $p_T > 25$ GeV ($p_T > 4$ GeV) are referred to as hard-lepton SRs (soft-lepton SRs) in the following sections.

7.1 Pure bino LSP scenario

The signature of stop pair production with subsequent \tilde{t}_1 decays is determined by the masses of the two sparticles, \tilde{t}_1 and $\tilde{\chi}_1^0$. It often leads to a final state similar to that of $t\bar{t}$ production, except for the additional E_T^{miss} due to the two additional $\tilde{\chi}_1^0$ s in the event. A set of event selections is defined targeting various signals.

Two signal regions are designed to target the majority of signal models in $\Delta m(\tilde{t}_1, \tilde{\chi}_1^0) > m_t$, tN_med and tN_high, which are optimised for medium and high \tilde{t}_1 mass, respectively. For the compressed region with $m_{\tilde{t}_1} \approx m_t + m_{\tilde{\chi}_1^0}$, three BDT selections (tN_diag_low, tN_diag_med, and tN_diag_high) target different \tilde{t}_1 masses. For the $\tilde{t}_1 \rightarrow bW\tilde{\chi}_1^0$ region, a signal selection (bWN) is defined by utilising the distinctive shape of the invariant mass of the bW system. For the $\tilde{t}_1 \rightarrow bff'\tilde{\chi}_1^0$ region, the signal region

(`bffN`) is defined by making use of the soft-lepton selection designed for the higgsino LSP scenarios. The event selection for each signal region is detailed in the following subsections.

7.1.1 $\tilde{t}_1 \rightarrow t\tilde{\chi}_1^0$ decay

Table 6 details the event selections for the `tN_med` and `tN_high` SRs. In addition to the high- E_T^{miss} preselection described in Table 4, at least one reconstructed hadronic top-quark candidate based on the recursive reclustered jet algorithm is required in both SRs. More stringent requirements are also imposed on E_T^{miss} , m_T and $H_{T,\text{sig}}^{\text{miss}}$. Furthermore, a requirement is placed on am_{T2} to reduce $t\bar{t}$ backgrounds. An angular separation between the highest- p_T b -tagged jet and the lepton, $\Delta R(b, \ell)$, is also required to further suppress $t\bar{t}$ and $W+\text{jets}$ backgrounds. The main background processes after all selection requirements are $ttZ(v\nu)$, dileptonic $t\bar{t}$ and $W+\text{heavy flavor}$ processes.

For the `tN_med` SR, a shape-fit technique is employed, with the SR subdivided in bins of E_T^{miss} , which allows for improved sensitivity in model-dependent exclusion fits over the cut-and-count analysis.

Table 6: Overview of the event selections for the `tN_med` and `tN_high` SRs. Round brackets are used to describe lists of values and square brackets denote intervals.

Signal region	<code>tN_med</code>	<code>tN_high</code>
Preselection	high- E_T^{miss} preselection	
Number of (jets, b -tags)	$(\geq 4, \geq 1)$	$(\geq 4, \geq 1)$
Jet p_T [GeV]	$> (60, 50, 40, 40)$	$> (100, 80, 50, 30)$
E_T^{miss} [GeV]	> 250	> 550
$E_{T,\perp}^{\text{miss}}$ [GeV]	> 230	–
$H_{T,\text{sig}}^{\text{miss}}$	> 14	> 27
m_T [GeV]		> 160
am_{T2} [GeV]		> 175
$m_{\text{top}}^{\text{reclustered}}$ [GeV]	> 150	> 130
$\Delta R(b, \ell)$		< 2.0
$ \Delta\phi(j_{1,2}, \vec{p}_T^{\text{miss}}) $		> 0.4
m_{T2}^{τ} based τ -veto [GeV]		> 80
Exclusion technique	shape-fit in E_T^{miss}	cut-and-count
Bin boundaries	$[250, 350, 450, 600, \text{inf}]$	

7.1.2 Compressed $\tilde{t}_1 \rightarrow t\tilde{\chi}_1^0$ decay

The three BDT selections (`tN_diag_low`, `tN_diag_med`, and `tN_diag_high`) are summarised in Table 7 and detailed in the following.

Table 7: Overview of the signal selections using BDTs to target compressed tN scenarios. Round brackets are used to describe lists of values and square brackets denote intervals.

Variable	tN_diag_low	tN_diag_med	tN_diag_high
Preselection	low- E_T^{miss}	low- E_T^{miss}	high- E_T^{miss}
Number of (jets, b -tags)	($\geq 4, \geq 1$)	($\geq 4, \geq 1$)	($\geq 5, \geq 1$)
Jet p_T [GeV]	$> (120, 25, 25, 25)$	$> (100, 50, 25, 25)$	$> (25, 25, 25, 25, 25)$
E_T^{miss} [GeV]	> 100	> 120	> 230
m_T [GeV]	> 90	> 120	> 120
R_{ISR}	–	–	> 0.4
$p_T(t\bar{t})$ [GeV]	> 400	–	–
$ \Delta\phi(l, t\bar{t}) $	> 1.0	–	–
$ \Delta\phi(j_{1,2}, \vec{p}_T^{\text{miss}}) $	> 0.4	> 0.4	–
m_{T2}^{τ} based τ -veto [GeV]	–	> 80	–
BDT score	BDT_low ≥ 0.55	BDT_med ≥ 0.4	BDT_high ≥ 0.6
Exclusion technique	cut-and-count	shape-fit in BDT score	shape-fit in BDT score
Bin boundaries	–	[0.4, 0.5, 0.6, 0.7, 0.8, 1.0]	[0.6, 0.7, 0.8, 1.0]

Low \tilde{t}_1 mass For \tilde{t}_1 masses close to the top-quark mass a BDT is trained for the tN_diag_low signal region. The preselection is based on the low- E_T^{miss} selection in Table 4.

The variables input to the BDT are E_T^{miss} and m_T , the difference Δm_T^α in m_T between the SM and signal hypothesis, the two top-quark candidate masses $m(t_{\text{had}}^{\text{ISR}})$ and $m(t_{\text{lep}}^\alpha)$ under the signal hypothesis, and the azimuthal angles between the lepton and the $t\bar{t}$ system, as well as between the lepton and $\vec{p}_T(\nu^\alpha)$.

The BDT output, from here on referred to as BDT_low, is used to define a single bin cut-and-count signal region, using the optimal point of $\text{BDT_low} > 0.55$, determined by maximising the expected significance. To avoid a significant extrapolation between control and signal regions an additional selection of $p_T(t\bar{t}) \geq 400$ GeV and $\Delta\phi(\ell, t\bar{t}) \geq 1.0$ is applied for all selected regions in the tN_diag_low context.

Medium \tilde{t}_1 mass Stop masses from about 200 to 400 GeV in the compressed scenario are targeted by a BDT using the the low- E_T^{miss} preselection given in Table 4. The input variables of the BDT are the E_T^{miss} and H_T^{sig} , the angular variables $\Delta\phi(\vec{p}_T^{\text{miss}}, t_{\text{had}}^\chi)$, $\Delta\phi(t_{\text{had}}^\chi, t_{\text{lep}}^\chi)$ and $\Delta R(b, \ell)$, masses m_T and m_{top}^χ , as well as the number of jets and the third and fourth jet p_T .

The BDT output score, referred to in the following as BDT_med, is used to define a signal region called tN_diag_med, based on the expected significance for a \tilde{t}_1 mass of 250 GeV. The known signal shape is exploited for the exclusion of signal models, using five bins in the BDT score.

High \tilde{t}_1 mass For compressed bino LSP scenarios with high \tilde{t}_1 mass, a BDT is trained based on the following variables: R_{ISR} , the angular variables $\Delta\phi(\text{ISR}, \ell)$, $\Delta\phi(t_{\text{had}}^\chi, t_{\text{lep}}^\chi)$, and $\Delta R(b, \ell)$, masses m_T , M_T^S and m_{top}^χ as well as the number of jets in the di-stop decay system and the third and fourth jet p_T , derived using the RJR techniques as described in Section 5. In addition to the high- E_T^{miss} preselection, a tightened

selection of $m_T > 120$ GeV is imposed to control the multijet background. An additional selection of $R_{\text{ISR}} > 0.4$ is applied to further reduce the background while retaining high efficiency for the considered signal events.

The resulting BDT output score, hereafter called BDT_high, is used to define the three signal bins of the `tN_diag_high` signal region.

7.1.3 $\tilde{t}_1 \rightarrow bW\tilde{\chi}_1^0$ and $\tilde{t}_1 \rightarrow bff'\tilde{\chi}_1^0$ decays

When the mass difference between the \tilde{t}_1 and the $\tilde{\chi}_1^0$ is smaller than the top-quark mass but greater than the sum of the W -boson and bottom-quark masses, the \tilde{t} decays dominantly through the three-body channel into a bottom-quark, a W -boson, and a $\tilde{\chi}_1^0$. The `bWN` SR is optimised to search for these events. Compared to the scenario with on-shell top-quarks, the three-body decay yields the same final-state objects but with significantly lower momenta, although typically still above the reconstruction thresholds.

The am_{T2} variable is a powerful discriminant for separating dileptonic $t\bar{t}$ background from signal models in this region of phase-space, as seen in Figure 19 in Section 10. Because $m_{\tilde{t}_1} - m_{\tilde{\chi}_1^0}$ is below the top-quark mass for signal, am_{T2} peaks at low values, while dileptonic $t\bar{t}$ decays typically saturate at values nearer to the top-quark mass. A shape-fit technique is employed, using five bins of am_{T2} , similar to the shape-fit employed in the `tN_med` SR.

When the \tilde{t}_1 mass is much closer to the $\tilde{\chi}_1^0$ mass, the stop undergoes a four-body decay with an off-shell W -boson, characterised by events with final-state objects having even lower momenta than in the three-body decay. A soft-lepton SR, `bCsoft_diag`, designed for the higgsino LSP scenario with a relaxed m_T requirement, provides good sensitivity to this scenario. A shape-fit is performed in the $p_T^\ell/E_T^{\text{miss}}$ variable, using three bins for the model-dependent exclusion fit.

The event selections for `bWN` and `bffN` are summarised in Table 8.

7.2 Wino NLSP scenario

If the wino mass M_2 is small enough, the stop may decay directly to the $\tilde{\chi}_1^\pm$ and $\tilde{\chi}_2^0$ (in addition to the $\tilde{\chi}_1^0$, as the bino is still assumed to be the LSP). In this case, the decays $\tilde{t}_1 \rightarrow b\tilde{\chi}_1^\pm$ and $\tilde{t}_1 \rightarrow t\tilde{\chi}_2^0$ become relevant, leading to a more complex phenomenology than that probed in the pure bino LSP scenario. The SRs targeting this scenario are referred to as `bC2x`.

Two SRs target the $\tilde{t}_1 \rightarrow b\tilde{\chi}_1^\pm$ decay: the `bC2x_med` and `bC2x_diag` SRs. The kinematics of the decay products are governed by the different mass splittings, with high- p_T b -jets produced from large $\Delta m(\tilde{t}_1, \tilde{\chi}_1^\pm)$ and high- p_T W -bosons from large $\Delta m(\tilde{\chi}_1^\pm, \tilde{\chi}_1^0)$.

In addition to the high E_T^{miss} preselection, more stringent selection requirements are imposed on m_T , $H_{T,\text{sig}}^{\text{miss}}$, and $|\Delta\phi(\text{jet}_i, \vec{p}_T^{\text{miss}})|$. The presence of a hadronic W -boson candidate is also required with a mass satisfying $m_W^{\text{reclustered}} > 50$ GeV in addition to the requirement of two high- p_T b -tagged jets. Furthermore, a requirement is placed on am_{T2} to reduce the $t\bar{t}$ background. The main backgrounds after the full signal selection are the $t\bar{t}Z(\nu\nu)$, dileptonic $t\bar{t}$, and single-top Wt processes.

Table 8: Overview of the event selections for the **bWN** and **bffN** SRs. Round brackets are used to describe lists of values and square brackets denote intervals. The veto on the reclustered hadronic top-quark candidate is satisfied for events where no reclustered jet candidate is found, or where the mass of the hadronic top ($m_{\text{top}}^{\text{reclustered}}$) is below a certain threshold (150 GeV).

Signal region	bWN	bffN
Preselection	high- $E_{\text{T}}^{\text{miss}}$	soft-lepton
Number of (jets, b -tags)	($\geq 4, \geq 1$)	($\geq 2, \geq 1$)
Jet p_{T} [GeV]	$> (50, 25, 25, 25)$	$> (400, 25)$
b -tagged jet p_{T} [GeV]	≥ 25	≥ 25
$E_{\text{T}}^{\text{miss}}$ [GeV]	> 300	> 300
m_{T} [GeV]	> 130	< 160
$am_{\text{T}2}$ [GeV]	< 110	–
$m_{\text{top}}^{\text{reclustered}}$ [GeV]	–	top veto
$p_{\text{T}}^{\ell}/E_{\text{T}}^{\text{miss}}$	–	< 0.02
$\Delta\phi(\vec{p}_{\text{T}}^{\text{miss}}, \ell)$	< 2.5	–
$\min(\Delta\phi(\vec{p}_{\text{T}}^{\text{miss}}, b\text{-jet}_i))$	–	< 1.5
$ \Delta\phi(j_{1,2}, \vec{p}_{\text{T}}^{\text{miss}}) $		
$m_{\text{T}2}^{\tau}$ based τ -veto [GeV]	> 80	–
Exclusion technique	shape-fit in $am_{\text{T}2}$	shape-fit in $p_{\text{T}}^{\ell}/E_{\text{T}}^{\text{miss}}$
Bin boundaries	[0, 91, 97, 106, 118, 130]	[0, 0.01, 0.015, 0.02]

An additional SR, **bCbv**, is designed for the simplified model $\tilde{t}_1 \rightarrow b\tilde{\chi}_1^{\pm}$ scenario with $\Delta m(\tilde{t}_1, \tilde{\chi}_1^{\pm}) = 10$ GeV, leading to a signature where the b -jets are too soft to be reconstructed. Tighter requirements on $E_{\text{T}}^{\text{miss}}$, m_{T} , $H_{\text{T},\text{sig}}^{\text{miss}}$, and $|\Delta\phi(\text{jet}_i, \vec{p}_{\text{T}}^{\text{miss}})|$ as well as an angular selection on $\Delta\phi(\vec{p}_{\text{T}}^{\text{miss}}, \ell)$ are also imposed to reduce the diboson backgrounds.

The event selections for **bC2x_diag**, **bC2x_med** and **bCbv** are summarised in Table 9.

7.3 Higgsino LSP scenario

The SRs optimised for the pure bino LSP scenarios such as **tN_med** have sensitivity to the higgsino model in events where a lepton is produced by a top-quark from the stop decay. However, three additional SRs, **bCsoft_diag**, **bCsoft_med**, and **bCsoft_high**, are designed to target the case when the lepton is soft, originating instead from a $\tilde{\chi}_1^{\pm}$ decay via a highly off-shell W -boson ($\tilde{\chi}_1^{\pm} \rightarrow \tilde{\chi}_1^0 + W^*(\ell\nu)$). This is particularly important in scenarios with $m_{tR} < m_{q3L}$ where the $\tilde{t}_1 \rightarrow b\tilde{\chi}_1^{\pm}$ BR is large. These soft-lepton SRs are defined to be orthogonal to the **tN_med** SR so that they can be statistically combined to profit from covering both decay chains.

The **bCsoft_diag** SR targets a region where the mass difference between the stop and higgsinos is less than the mass of the top-quark, so the stop must decay via the $\tilde{t}_1 \rightarrow b\tilde{\chi}_1^{\pm}$ mode. Since none of the decay products receive a large momentum transfer, a high- p_{T} ISR jet is required to boost the $\tilde{t}_1\tilde{t}_1$ system in order to achieve better separation of signal and background. As a result, the signature is characterised by a high- p_{T} jet, large $E_{\text{T}}^{\text{miss}}$, and a soft lepton. In addition to the preselection, a more stringent selection

Table 9: Overview of the event selections for the `bC2x_med`, `bC2x_diag`, and `bCv` SRs. Round brackets are used to describe lists of values and square brackets denote intervals.

Signal region	<code>bC2x_diag</code>	<code>bC2x_med</code>	<code>bCv</code>
Preselection	high- E_T^{miss} preselection		
Number of (jets, b -tags)	$(\geq 4, \geq 2)$	$(\geq 4, \geq 2)$	$(\geq 2, = 0)$
Jet p_T [GeV]	$> (75, 75, 75, 30)$	$> (200, 140, 25, 25)$	$> (120, 80)$
b -tagged jet p_T [GeV]	$> (30, 30)$	$> (140, 140)$	—
E_T^{miss} [GeV]	> 230	> 230	> 360
$H_{T,\text{sig}}^{\text{miss}}$	> 13	> 10	> 16
m_T [GeV]	> 180	> 120	> 200
am_{T2} [GeV]	> 175	> 300	—
$ \Delta\phi(\text{jet}_i, \vec{p}_T^{\text{miss}}) (i = 1)$	> 0.7	> 0.9	> 2.0
$ \Delta\phi(\text{jet}_i, \vec{p}_T^{\text{miss}}) (i = 2)$	> 0.7	> 0.9	> 0.8
$m_W^{\text{reclustered}}$ [GeV]	> 50	> 50	[70, 100]
$\Delta\phi(\vec{p}_T^{\text{miss}}, \ell)$	—	—	> 1.2
$ \Delta\phi(j_{1,2}, \vec{p}_T^{\text{miss}}) $		> 0.4	
m_{T2}^{τ} based τ -veto [GeV]	> 80	> 80	—
exclusion technique	cut-and-count	cut-and-count	cut-and-count

requirement is imposed on the E_T^{miss} and an upper cut on m_T is required to reduce the background from on-shell W -bosons. Furthermore, an angular requirement is placed on $\min(\Delta\phi(\vec{p}_T^{\text{miss}}, b\text{-jet}_i))$ to reduce $t\bar{t}$ backgrounds. The main background after all selection requirements is semi-leptonic $t\bar{t}$ and $W+\text{jets}$ processes. The `bCsoft_diag` SR with relaxed m_T requirement is found to be sensitive to the $\tilde{t}_1 \rightarrow bff'\tilde{\chi}_1^0$ signature and is described further in Section 7.1.3.

The second SR, `bCsoft_med`, targets generic higgsino models where each of the decays $\tilde{t}_1 \rightarrow b\tilde{\chi}_1^\pm$, $\tilde{t}_1 \rightarrow t\tilde{\chi}_1^0$, and $\tilde{t}_1 \rightarrow t\tilde{\chi}_2^0$ are allowed. In particular, it is designed to select the large fraction of events that produce “mixed” decays, where one \tilde{t}_1 decays via a chargino and the other via a neutralino. In such cases, the $\tilde{t}_1 \rightarrow b\tilde{\chi}_1^\pm$ decay produces a high- p_T b -jet, while the b -jet from the other branch, $\tilde{t}_1 \rightarrow t\tilde{\chi}_1^0$ or $\tilde{t}_1 \rightarrow t\tilde{\chi}_2^0$, can be much softer. The third SR, `bCsoft_high`, targets the higher stop masses, focusing on the $\tilde{t}_1 \rightarrow b\tilde{\chi}_1^\pm$ signature. The $\tilde{\chi}_1^\pm$ is boosted due to the large mass difference between the stop and higgsino states, and therefore the signature is characterised by two high- p_T b -jets, large E_T^{miss} , and a soft-lepton. In addition to the preselection, cuts on p_T^W , am_{T2} , $\min(\Delta\phi(\vec{p}_T^{\text{miss}}, b\text{-jet}_i))$, and $\Delta R(b_1, b_2)$ are required to reduce backgrounds. The remaining background after all signal selection requirements is dominated by semi-leptonic $t\bar{t}$, single-top Wt , and $W+\text{heavy flavor}$ events.

In all three SRs, $p_T^\ell/E_T^{\text{miss}}$ is a powerful discriminant as the higgsino signature is characterised by low- p_T leptons and large E_T^{miss} , while the SM backgrounds are dominated by events with leptonic W decays, producing lepton p_T and E_T^{miss} of a similar magnitude. The shape-fit in $p_T^\ell/E_T^{\text{miss}}$ employs three bins for the model-dependent exclusion fit ([0, 0.01, 0.015, 0.02] for the `bCsoft_diag` region and [0, 0.015, 0.03, 0.1] for both `bCsoft_med` and `bCsoft_high`), similar to the shape-fits implemented for the `tN_med` and `bWN` SRs.

The event selections for `bCsoft_diag`, `bCsoft_med`, and `bCsoft_high` are detailed in Table 10.

Table 10: Overview of the event selections for the `bCsoft_diag`, `bCsoft_med`, and `bCsoft_high` SRs. Round brackets are used to describe lists of values and square brackets denote intervals. For `bCsoft_diag` SR, the leading jet is required not to be b -tagged.

Signal region	<code>bCsoft_diag</code>	<code>bCsoft_med</code>	<code>bCsoft_high</code>
Preselection	soft-lepton preselection		
Number of (jets, b -tags)	$(\geq 2, \geq 1)$	$(\geq 3, \geq 2)$	$(\geq 2, \geq 2)$
Jet p_T [GeV]	$> (400, 25)$	$> (120, 60, 40, 25)$	$> (100, 100)$
b -tagged jet p_T [GeV]	> 25	$> (120, 60)$	$> (100, 100)$
E_T^{miss} [GeV]	> 300	> 230	> 230
m_T [GeV]	< 50	< 160	< 160
p_T^W [GeV]	–	> 400	> 500
$p_T^\ell/E_T^{\text{miss}}$	< 0.02	< 0.03	< 0.03
am_{T2} [GeV]	–	> 200	> 300
$\min(\Delta\phi(\vec{p}_T^{\text{miss}}, b\text{-jet}_i))$	< 1.5	> 0.8	> 0.4
$\Delta R(b_1, b_2)$	–	–	> 0.8
$ \Delta\phi(j_{1,2}, \vec{p}_T^{\text{miss}}) $		> 0.4	
Exclusion technique	shape-fit in $p_T^\ell/E_T^{\text{miss}}$	shape-fit in $p_T^\ell/E_T^{\text{miss}}$	shape-fit in $p_T^\ell/E_T^{\text{miss}}$
Bin boundaries	[0, 0.01, 0.015, 0.02]	[0, 0.015, 0.03, 0.1]	[0, 0.015, 0.03, 0.1]

7.4 Bino/higgsino mix scenario

For the bino/higgsino mix scenario, the SRs designed for other scenarios are found to have good sensitivity for this scenario, and are therefore used.

7.5 Spin-0 mediator scenario

Two SRs, `DM_low` and `DM_high`, are designed to search for dark matter that is pair-produced via a spin-0 mediator (either scalar or pseudo-scalar) in association with a $t\bar{t}$ process. The `DM_low` SR is optimised for mediator masses around $m_\phi = 20$ GeV, while the `DM_high` SR targets mediator masses around $m_\phi = 300$ GeV.

In addition, a predecessor to the `DM_low` signal region, originally designed for a search using a smaller data set (13.2 fb^{-1}), has been retained, as the number of observed events exceeded the background prediction by 3.3 standard deviations [147]. This signal region, which was previously called `DM_low`, is referred to here as `DM_low_loose`.

Table 11 details the event selections for each of the three SRs. In addition to the high- E_T^{miss} preselection, more stringent requirements are also imposed on E_T^{miss} , m_T , and $H_{T,\text{sig}}^{\text{miss}}$. At least one reconstructed hadronic top-quark candidate is required with $m_{\text{top}}^{\text{reclustered}} > 130$ GeV in the newly defined SRs. A high am_{T2} requirement and an angular selection requirement of $|\Delta\phi(\text{jet}_i, \vec{p}_T^{\text{miss}})|$ are further imposed to reduce

the $t\bar{t}$ background. The main backgrounds after all signal selection requirements are the $t\bar{t}Z(\nu\nu)$, dileptonic $t\bar{t}$, and W +heavy flavor processes.

The event selections for DM_low_loose, DM_low, and DM_high are summarised in Table 11.

Table 11: Overview of the event selections for the DM_low_loose, DM_low, and DM_high SRs. Round brackets are used to describe lists of values.

Signal region	DM_low_loose	DM_low	DM_high
Preselection	high- E_T^{miss} preselection		
Number of (jets, b -tags)	$(\geq 4, \geq 1)$	$(\geq 4, \geq 1)$	$(\geq 4, \geq 1)$
Jet p_T [GeV]	$> (60, 60, 40, 25)$	$> (120, 85, 65, 25)$	$> (125, 75, 65, 25)$
b -tagged jet p_T [GeV]	> 25	> 60	> 25
E_T^{miss} [GeV]	> 300	> 320	> 380
m_T [GeV]	> 120	> 170	> 225
$H_{T,\text{sig}}^{\text{miss}}$	> 14	> 14	–
am_{T2} [GeV]	> 140	> 160	> 190
$m_{\text{top}}^{\text{reclustered}}$ [GeV]	–	> 130	> 130
$\Delta\phi(\vec{p}_T^{\text{miss}}, \ell)$	> 0.8	> 1.2	> 1.2
$ \Delta\phi(\text{jet}_i, \vec{p}_T^{\text{miss}}) $	> 1.4	> 1.0	> 1.0
$ \Delta\phi(j_{1,2}, \vec{p}_T^{\text{miss}}) $		> 0.4	
m_{T2}^{τ} based τ -veto [GeV]		> 80	
exclusion technique	cut-and-count	cut-and-count	cut-and-count

8 Background estimates

The dominant background processes in this analysis originate from $t\bar{t}$, single-top Wt , $t\bar{t} + Z(\rightarrow \nu\bar{\nu})$, and W +jets production. Most of the $t\bar{t}$ and Wt events in the hard-lepton signal regions have both W -bosons decaying leptonically (one of which is ‘lost’, meaning it is either not reconstructed, not identified, or removed by the overlap removal procedure) or one W -boson decaying leptonically and the other via a hadronically decaying τ lepton. This is in contrast to the soft-lepton signal regions, where most of the $t\bar{t}$ and Wt contribution arises from semi-leptonic decays.

The $t\bar{t}$ background is treated separately in the decay components discussed above, referred to as 1L and 2L, which also includes dileptonic $t\bar{t}$ process where a W -boson decays to τ lepton subsequently decaying hadronically. The $t\bar{t} + Z$ background combined with a subdominant $t\bar{t} + W$ contribution is referred to as $t\bar{t} + V$. Other background processes considered are dibosons, Z +jets, and multijet events. The multijet background is estimated from data using a fake-factor method [148]. It is found to be negligible in all regions. All other backgrounds are determined from simulation, normalised to the most accurate theoretical cross-sections available.

The main background processes are estimated via a dedicated CR, used to normalise the simulation to the data with a simultaneous fit, discussed in Section 10. The CRs are defined as event selections that are kinematically close to the SRs but with a few key variable requirements inverted to significantly reduce the

potential signal contamination and enhance the yield and purity of a particular background. Each SR has dedicated CRs for the background processes that have the largest contributions. The following background processes are normalised in dedicated CRs: semi-leptonic $t\bar{t}$ (T1LCR), dileptonic $t\bar{t}$ (T2LCR), W +jets (WCR), single-top (STCR), and $t\bar{t} + W/Z$ (TZCR) processes.

Several signal regions (bWN, tN_diag_low, and tN_diag_high) that are dominated exclusively by either semi-leptonic or dileptonic $t\bar{t}$ events have only one associated CR, denoted generically TCR. Signal regions can have a fewer number of associated CRs when the fractional contribution of the corresponding background is small. For the shape-fit analyses, the CRs of each background are not binned and only one normalisation factor is extracted for each background process, which is applied in all SR bins.¹³

The background estimates are tested using VRs, which are disjoint from both the CRs and SRs. Background normalisations determined in the CRs are extrapolated to the VRs and compared with the observed data. Each SR has associated VRs for the $t\bar{t}$ (T1LVR and T2LVR) and W +jets (WVR) processes, which are constructed by inverting or relaxing the selection requirements to be orthogonal to the corresponding SR and CRs. A single-top Wt VR (STVR) is defined for the bCsoft_med and bCsoft_high SRs, where Wt is one of the dominant background processes.

The VRs are not used to constrain parameters in the fit, but provide a statistically independent test of the background estimates made using the CRs. The potential signal contamination in the VRs is studied for all considered signal models and mass ranges, and found to be less than a few percent in most of VRs, and less than 15% in VRs for the tN_diag SRs.

In the analysis, the background estimates are categorised into several different approaches. The requirement of the presence of hadronic top-quark candidates (top-tagging) is a key for the background estimate in the SRs targeting signals with high- p_T top-quarks. Similarly hadronic W -boson reconstruction (W -tagging) is employed for the background estimate in the SRs targeting signals with high- p_T W -bosons decaying hadronically. In the following subsections the two approaches are described in detail together with the background estimates for the remaining SRs. Table 12 summarises the approaches for each SR with a brief description of the targeted signal scenarios, and each of those approaches are detailed in the following Sections 8.1-8.5.

8.1 Hadronic top-tagging approach

In SRs targeting signals with high- p_T top-quarks (tN_med, tN_high, DM_low, and DM_high), a requirement is made that events contain a recursively reclustered jet with a mass consistent with the top-quark mass. While the requirement on $m_{\text{top}}^{\text{reclustered}}$ is powerful for identifying signals, it is also useful in defining CRs that are enriched in background processes with hadronically decaying top-quarks (“top-tagged”) or depleted in such backgrounds (“top-vetoed”).

The CR for dileptonic $t\bar{t}$ (T2LCR) requires m_T above the W -boson endpoint. The requirement on am_{T2} is inverted (to select events with values below the top-quark mass) and a hadronic top-quark veto is required to reduce the potential signal contamination and improve the purity. The semi-leptonic $t\bar{t}$ CR (T1LCR) requires a hadronic top-tagging and that the m_T be within a window around the W -boson mass. The background from semi-leptonic $t\bar{t}$ events is negligible in the SR but can be sizeable in the other CRs.

¹³ The binned CR approach is tested by comparing the results to a one-bin CR. The normalisation factors are found to be consistent with each other within the statistical uncertainties.

Table 12: Overview of various approaches for the background estimates in all signal regions together with the targeted signal scenario. The $t\bar{t} + Z(\ell\ell)$ control region (CR) described in Section 8.6 is also defined in the top-tagging and W -tagging approaches, except for the bC_b SR where the contribution of the $t\bar{t} + V$ background is negligible.

SR	Signal scenario	background strategy	Sections
tN _{med}	Pure bino LSP	top-tagging + $t\bar{t}Z$ CR	8.1
tN _{high}	Pure bino LSP	top-tagging + $t\bar{t}Z$ CR	8.1
tN _{diag_low}	Pure bino LSP	BDT	8.2
tN _{diag_med}	Pure bino LSP	BDT	8.2
tN _{diag_high}	Pure bino LSP	BDT	8.2
bWN	Pure bino LSP	three-body	8.3
bffN	Pure bino LSP	soft-lepton	8.5
bC2x _{med}	Wino NLSP	W -tagging + $t\bar{t}Z$ CR	8.4
bC2x _{diag}	Wino NLSP	W -tagging + $t\bar{t}Z$ CR	8.4
bC _b	Wino NLSP	W -tagging	8.4
bCsoft _{diag}	Higgsino LSP	soft-lepton	8.5
bCsoft _{med}	Higgsino LSP	soft-lepton	8.5
bCsoft _{high}	Higgsino LSP	soft-lepton	8.5
DM _{low_loose}	DM+ $t\bar{t}$	top-tagging + $t\bar{t}Z$ CR	8.1
DM _{low}	DM+ $t\bar{t}$	top-tagging + $t\bar{t}Z$ CR	8.1
DM _{high}	DM+ $t\bar{t}$	top-tagging + $t\bar{t}Z$ CR	8.1

The CRs for W -jets (WCR) and single-top (STCR) require m_T to be below the W -boson mass. Both CRs also require large am_{T2} and a hadronic top-quark veto. The STCR requires additionally two b -tagged jets to reduce the W -jets contribution while increasing the fraction of Wt against $t\bar{t}$ events, and a minimum separation between the b -tagged jets, $\Delta R(b_1, b_2) > 1.2$. This latter requirement is useful to suppress the semi-leptonic $t\bar{t}$ contribution, which can evade the am_{T2} endpoint when a charm-quark from the hadronic W -boson decay is mis-identified as a b -tagged jet, often leading to a small separation among the two identified b -tagged jets. Events with exactly one b -tagged jet or $\Delta R(b_1, b_2) < 1.2$ are assigned to the WCR. In order to increase the W -jets purity only events with a positively charged lepton are selected. This requirement exploits the asymmetry in the production of W^+ over W^- events in LHC proton–proton collisions. The asymmetry is further enhanced by the requirement of large E_T^{miss} , as neutrinos from decays of the mostly left-handed W^+ boson are preferentially emitted in the direction of the W -boson.

In addition, the background contribution from $t\bar{t} + V$ is large and a dedicated control region is designed, which is described in Section 8.6.

Figure 9 shows various kinematic distributions of the CRs associated to the tN_{med} SR. The backgrounds are scaled with normalisation factors obtained from a simultaneous likelihood fit of the CRs, described in Section 10.

A set of VRs associated with the corresponding CRs is defined by modifying the requirements on the m_T , am_{T2} , and hadronic top-tagging variables. The semi-leptonic $t\bar{t}$ validation region (T1LVR) and W -jets validation region (WVR) slide the m_T window to 90–120 GeV. The dileptonic $t\bar{t}$ VR (T2LVR) inverts the requirement of the hadronic top-quark veto (so that a hadronic top-quark tag is required) and relaxes the

requirement on am_{T2} . Since $t\bar{t}$ events are dominated by dileptonic $t\bar{t}$ after the large m_T requirement, the purity of dileptonic $t\bar{t}$ events remains high, despite the hadronic top-quark tag requirement. The relaxed am_{T2} cut significantly reduces the potential signal contamination. There is no single-top Wt VR (STVR) for these CRs. The m_T window for the STCR extends to 120 GeV in order to increase the number of data events entering the CR.

In Figure 9, various kinematic distributions of the VRs associated with tN_{med} are compared to the observed data. The backgrounds are scaled with normalisation factors obtained from a simultaneous likelihood fit of the CRs, described in Section 10.

Table 13 and 14 detail the definitions of the CRs and VRs associated with the SRs tN_{med} , tN_{high} , DM_{low} , and DM_{high} .

8.2 BDT analyses

For the signal regions $tN_{\text{diag_low}}$, $tN_{\text{diag_med}}$ and $tN_{\text{diag_high}}$, control regions use the signal selections but change the requirements on the BDT output scores. Due to its large fractional contribution, only the $t\bar{t}$ background is constrained using data, with all other backgrounds use predictions from samples of simulated events.

Although the main background is always the $t\bar{t}$ process in all three SRs, the fraction of dileptonic $t\bar{t}$ events varies. Therefore, a different strategy is employed for each SR.

For the signal regions $tN_{\text{diag_low}}$ and $tN_{\text{diag_high}}$, the $t\bar{t}$ background is treated as a single component, with a single normalisation factor being derived. One $t\bar{t}$ control region (TCR) is used for $tN_{\text{diag_low}}$, while three control-region bins (TCR1, TCR2, and TCR3) are used for $tN_{\text{diag_high}}$ in order to improve the stability of the simultaneous fit by reducing the correlation between the signal and $t\bar{t}$ background.

For $tN_{\text{diag_med}}$, the $t\bar{t}$ background is split into semi-leptonic and dileptonic $t\bar{t}$ contributions. Two control-region bins (TCR1 and TCR2) are defined to constrain the $t\bar{t}$ background and determine two separate normalisation factors for its two components in all fits to the data. Selected kinematic distributions of the $tN_{\text{diag_low}}$ and $tN_{\text{diag_med}}$ CRs are shown in Figure 10.

An overview of the CR selections for the BDT analyses can be found in Table 15.

8.3 $\tilde{t}_1 \rightarrow bW\tilde{\chi}_1^0$ analysis

Almost all of the background in the bWN SR consists of dileptonic $t\bar{t}$ events (where one of the leptons is lost or a hadronically decaying tau lepton). Therefore, a single high-purity TCR is defined by relaxing the selection requirements of E_T^{miss} and am_{T2} . In addition, the cut on $\Delta\phi(\vec{p}_T^{\text{miss}}, \ell)$ is inverted to reduce the potential signal contamination. The TVR is defined by sliding the am_{T2} window to 110 – 130 GeV in order to validate the background normalisation obtained from the TCR.

Figure 11 shows kinematic distributions in the CRs associated with the bWN SR. Table 16 details the corresponding CR and VR selections together with the SR selection.

Table 13: Overview of the selections for the `tN_med` and `tN_high` signal regions as well as the associated control and validation regions. The control regions include the semi-leptonic $t\bar{t}$ control region (T1LCR), the dileptonic $t\bar{t}$ control region (T2LCR), the W +jets control region (WCR), and the single-top Wt control region (STCR). The validation regions include the semi-leptonic $t\bar{t}$ validation region (T1LVR), the dileptonic $t\bar{t}$ validation region (T2LVR), and the W +jets validation region (WVR). Round brackets are used to describe lists of values and square brackets denote intervals. The veto on the reclustered hadronic top-quark candidate is satisfied for events where no reclustered jet candidate is found, or where the mass of the hadronic top-quark ($m_{\text{top}}^{\text{reclustered}}$) is below the specified tag threshold. For the WCR, $\Delta R(b_1, b_2) < 1.2$ is not required when the event has only 1 b -tagged jet. The selection of the $t\bar{t} + V$ control region (TZCR) is detailed in Section 8.6.

	<code>tN_med</code>	T1LCR/VR	T2LCR/VR	WCR/VR	STCR
Preselection	high- $E_{\text{T}}^{\text{miss}}$ preselection				
Number of (jets, b -tags)	$(\ge 4, \ge 1)$	$(\ge 4, \ge 1)$	$(\ge 4, \ge 1)$	$(\ge 4, \ge 1)$	$(\ge 4, \ge 2)$
Jet p_{T} [GeV]			$> (60, 50, 40, 40)$		
b -tagged jet p_{T} [GeV]			> 25		$> (25, 25)$
$E_{\text{T}}^{\text{miss}}$ [GeV]			> 250		
$E_{\text{T},\perp}^{\text{miss}}$ [GeV]			> 230		
m_{T} [GeV]	> 160	$[30, 90] / [90, 120]$	> 120	$[30, 90] / [90, 120]$	$[30, 120]$
$H_{\text{T},\text{sig}}^{\text{miss}}$	> 14	> 10	> 10	> 10	> 10
$m_{\text{top}}^{\text{reclustered}}$ [GeV]	> 150	> 150	top veto / > 150	top veto	top veto
$am_{\text{T}2}$ [GeV]	> 175	< 200	$< 200 / < 130$	> 200	> 200
$\Delta R(b, \ell)$	< 2.0	–	–	–	–
$\Delta R(b_1, b_2)$	–	–	–	< 1.2	> 1.2
lepton charge	–	–	–	+1	–
$ \Delta\phi(j_{1,2}, \vec{p}_{\text{T}}^{\text{miss}}) $			> 0.4		
$m_{\text{T}2}^{\tau}$ based τ -veto [GeV]			> 80		
	<code>tN_high</code>	T1LCR/VR	T2LCR/VR	WCR/VR	STCR
Preselection	high- $E_{\text{T}}^{\text{miss}}$ preselection				
Number of (jets, b -tags)	$(\ge 4, \ge 1)$	$(\ge 4, \ge 1)$	$(\ge 4, \ge 1)$	$(\ge 4, \ge 1)$	$(\ge 4, \ge 2)$
Jet p_{T} [GeV]			$> (100, 80, 50, 30)$		
b -tagged jet p_{T} [GeV]			> 25		$> (25, 25)$
$E_{\text{T}}^{\text{miss}}$ [GeV]	> 550	> 350	> 350	> 350	> 350
m_{T} [GeV]	> 160	$[30, 90] / [90, 120]$	> 120	$[30, 90] / [90, 120]$	$[30, 120]$
$H_{\text{T},\text{sig}}^{\text{miss}}$	> 27	> 10	> 10	> 10	> 10
$m_{\text{top}}^{\text{reclustered}}$ [GeV]	> 130	> 130	top veto / > 130	top veto	top veto
$am_{\text{T}2}$ [GeV]	> 175	< 200	$< 200 / < 130$	> 200	> 200
$\Delta R(b, \ell)$	< 2.0	–	–	–	–
$\Delta R(b_1, b_2)$	–	–	–	< 1.2	> 1.2
lepton charge	–	–	–	+1	–
$ \Delta\phi(j_{1,2}, \vec{p}_{\text{T}}^{\text{miss}}) $			> 0.4		
$m_{\text{T}2}^{\tau}$ based τ -veto [GeV]			> 80		

8.4 Hadronic W -tagging approach

Control regions for the `bC2x_diag` and `bC2x_med` SRs exploit hadronic W -boson tagging (W -tagging) with the $m_W^{\text{reclustered}}$ variable, closely following the strategy described in Section 8.1. The CRs invert two out of three requirements on m_{T} , $am_{\text{T}2}$, and the hadronic W -boson candidate mass.

For the `bC2v` SR, since the veto on b -tagged jets is required in the signal-region selection, a different CR

Table 14: Overview of the selections for the **DM_low** and **DM_high** signal regions as well as the associated control and validation regions. The control regions include the semi-leptonic $t\bar{t}$ control region (T1LCR), the dileptonic $t\bar{t}$ control region (T2LCR), the $W+jets$ control region (WCR), and the single-top Wt control region (STCR). The validation regions include the semi-leptonic $t\bar{t}$ validation region (T1LVR), the dileptonic $t\bar{t}$ validation region (T2LVR), and the $W+jets$ validation region (WVR). Round brackets are used to describe lists of values and square brackets denote intervals. The veto on the reclustered hadronic top-quark candidate is satisfied for events where no reclustered jet candidate is found, or where the mass of the hadronic top-quark ($m_{top}^{reclustered}$) is below a certain threshold. For the WCR, $\Delta R(b_1, b_2) < 1.2$ is not required when the event has only 1 b -tagged jet. The selection of the $t\bar{t} + V$ control region (TZCR) is detailed in Section 8.6.

	DM_low	T1LCR/VR	T2LCR/VR	WCR/VR	STCR
Preselection	high- E_T^{miss} preselection				
Number of (jets, b -tags)	$(\ge 4, \ge 1)$	$(\ge 4, \ge 1)$	$(\ge 4, \ge 1)$	$(\ge 4, \ge 1)$	$(\ge 4, \ge 2)$
Jet p_T [GeV]			$> (120, 85, 65, 60)$		
b -tagged jet p_T [GeV]			> 25		$> (25, 25)$
E_T^{miss} [GeV]	> 320	> 250	> 230	> 250	> 250
m_T [GeV]	> 170	$[30, 90] / [90, 120]$	> 120	$[30, 90] / [90, 120]$	$[30, 120]$
$H_{T,\text{sig}}^{\text{miss}}$	> 14	> 10	> 10	> 10	> 10
$m_{top}^{\text{reclustered}}$ [GeV]	> 130	> 130	top veto / > 130	top veto	top veto
am_{T2} [GeV]	> 160	< 200	< 160	> 160	> 200
$\Delta\phi(\vec{p}_T^{\text{miss}}, \ell)$	> 1.2	–	> 1.2	–	–
$ \Delta\phi(\text{jet}_i, \vec{p}_T^{\text{miss}}) $	> 1.0	–	–	–	–
$\Delta R(b_1, b_2)$	–	–	–	< 1.2	> 1.2
lepton charge	–	–	–	+1	–
$ \Delta\phi(j_{1,2}, \vec{p}_T^{\text{miss}}) $			> 0.4		
m_{T2}^{τ} based τ -veto [GeV]			> 80		
	DM_high	T1LCR/VR	T2LCR/VR	WCR/VR	STCR
Preselection	high- E_T^{miss} preselection				
Number of (jets, b -tags)	$(\ge 4, \ge 1)$	$(\ge 4, \ge 1)$	$(\ge 4, \ge 1)$	$(\ge 4, \ge 1)$	$(\ge 4, \ge 2)$
Jet p_T [GeV]			$> (125, 75, 65, 25)$		
b -tagged jet p_T [GeV]			> 25		$> (25, 25)$
E_T^{miss} [GeV]	> 380	> 280	> 280	> 280	> 280
m_T [GeV]	> 225	$[30, 90] / [90, 120]$	> 120	$[30, 90] / [90, 120]$	$[30, 120]$
$m_{top}^{\text{reclustered}}$ [GeV]	> 130	> 130	top veto / > 130	top veto	top veto
am_{T2} [GeV]	> 190	< 200	$< 200 / < 190$	> 190	> 200
$\Delta\phi(\vec{p}_T^{\text{miss}}, \ell)$	> 1.2	–	> 1.2	–	–
$ \Delta\phi(\text{jet}_i, \vec{p}_T^{\text{miss}}) $	> 1.0	> 1.0	–	> 1.0	–
$\Delta R(b_1, b_2)$	–	–	–	< 1.2	> 1.2
lepton charge	–	–	–	+1 / –	–
$ \Delta\phi(j_{1,2}, \vec{p}_T^{\text{miss}}) $			> 0.4	$> 0.4 / -$	> 0.4
m_{T2}^{τ} based τ -veto [GeV]			> 80		

strategy is used. The WCR and TCR remove the selection requirement on $\Delta\phi(\vec{p}_T^{\text{miss}}, \ell)$ and select a m_T window of $30 - 90$ GeV to increase the number of events in the region while suppressing potential signal contamination. A b -tagged jet is further required in the TCR to improve the purity of $t\bar{t}$ events.

Figure 12 shows selected kinematic distributions of associated CRs for **bC2x_med**.

A set of VRs associated to the CRs is defined following the approach taken for the top-tagging VRs in Section 8.1, i.e. by modifying the requirements on the m_T , am_{T2} , and hadronic W -tagging variables.

Table 15: Overview of signal region and control region (CR) definitions for the BDT analyses targeting the compressed bino LSP scenarios. The selections described in Table 7 are applied, except for the BDT score. Square brackets denote intervals.

Signal Region	<code>tN_diag_low</code>	<code>tN_diag_med</code>	<code>tN_diag_high</code>			
BDT score	≥ 0.55	≥ 0.4	≥ 0.6			
Associated CRs	TCR	TCR1	TCR2	TCR1	TCR2	
BDT score	[−1, 0.1]	[−1, −0.4]	[−0.4, 0.4]	[−1, −0.5]	[−0.5, 0]	[0, 0.4]

Table 16: Overview of the selections for the `bWN` signal region and associated CR. Round brackets are used to describe lists of values and square brackets denote intervals.

	<code>bWN</code>	TCR/VR
Preselection	high- E_T^{miss} preselection	
Number of (jets, b -tags)	($\geq 4, \geq 1$)	($\geq 4, \geq 1$)
Jet p_T [GeV]	$> (50, 25, 25, 25)$	
b -tagged jet p_T [GeV]	> 25	
E_T^{miss} [GeV]	> 300	> 230
m_T [GeV]	> 130	> 130
am_{T2} [GeV]	< 110	$[130, 170] / [110, 130]$
$\Delta\phi(\vec{p}_T^{\text{miss}}, \ell)$	< 2.5	> 2.5
$ \Delta\phi(j_{1,2}, \vec{p}_T^{\text{miss}}) $		> 0.4
m_{T2}^{τ} based τ -veto [GeV]		> 80

Tables 17 and 18 detail the CR and VR selections for the corresponding SRs.

8.5 Soft-lepton analyses

For the soft-lepton SRs (`bCsoft_diag`, `bCsoft_med`, `bCsoft_high`, and `bffN`), a single TCR, dominated by semi-leptonic $t\bar{t}$ events, is defined for the $t\bar{t}$ background as the fraction of dileptonic $t\bar{t}$ background is small compared to the other SRs because there is no m_T requirement.

For `bCsoft_med` and `bCsoft_high` SRs, three CRs (TCR, WCR, and STCR) are defined by inverting the requirements on am_{T2} , $p_T^\ell/E_T^{\text{miss}}$, and the number of b -tagged jets, while requiring the same p_T^W threshold as the corresponding SR to ensure similar kinematics in the SR and CRs for the p_T of the top-quark and the W -boson, which can be poorly modelled by the simulation. The TCR is designed by inverting the selection requirement on am_{T2} and relaxing $p_T^\ell/E_T^{\text{miss}}$ to minimise the potential signal contamination while improving the purity. Similarly, the STCR and WCR are defined by relaxing $p_T^\ell/E_T^{\text{miss}}$. For the WCR, exactly one b -tagged jet is also required to make it orthogonal to STCR.

For the `bCsoft_diag` SR, the CR strategy with the top-tagging is employed, based on the $m_{\text{top}}^{\text{reclustered}}$ variable as described in Section 8.1. The TCR is defined by requiring a tagged hadronic top-quark candidate and relaxing the requirement on m_T to increase the number of $t\bar{t}$ events, while the WCR is defined by requiring a hadronic top-quark veto. For the WCR, an additional requirement is imposed on $\min(\Delta\phi(\vec{p}_T^{\text{miss}}, b\text{-jet}_i))$ to increase the purity of W +jets events. The STCR is not defined for this SR, as the Wt contribution is small compared to other backgrounds. The CRs for the `bffN` SR are identical to the ones for `bCsoft_diag` because of the similarity in the SR selections.

Table 17: Overview of the selections for the `bC2x_diag` and `bC2x_med` signal regions as well as the associated control and validation regions. The control regions include the semi-leptonic $t\bar{t}$ control region (T1LCR), the dileptonic $t\bar{t}$ control region (T2LCR), the W +jets control region (WCR), and the single-top Wt control region (STCR). The validation regions include the semi-leptonic $t\bar{t}$ validation region (T1LVR), the dileptonic $t\bar{t}$ validation region (T2LVR), and the W +jets validation region (WVR). Round brackets are used to describe lists of values and square brackets denote intervals. The veto on the reclustered hadronic W -boson candidate is satisfied for events where no reclustered jet candidate is found, or where the mass of the hadronic top-quark ($m_{\text{top}}^{\text{reclustered}}$) is below the specified tag threshold. For the WCR, $\Delta R(b_1, b_2) < 1.2$ is not required when the event has only 1 b -tagged jet. The selection of the $t\bar{t} + V$ control region (TZCR) is detailed in Section 8.6.

	<code>bC2x_diag</code>	T1LCR/VR	T2LCR/VR	WCR/VR	STCR
Preselection		high- $E_{\text{T}}^{\text{miss}}$ preselection			
Number of (jets, b -tags)	$(\geq 4, \geq 2)$	$(\geq 4, \geq 2)$	$(\geq 4, \geq 2)$	$(\geq 4, \geq 1)$	$(\geq 4, \geq 2)$
Jet p_{T} [GeV]			$> (75, 75, 75, 30)$		
b -tagged jet p_{T} [GeV]	$> (30, 30)$	$> (30, 30)$	$> (30, 30)$	$> (30, -)$	$> (30, 30)$
$E_{\text{T}}^{\text{miss}}$ [GeV]			> 230		
$H_{\text{T},\text{sig}}^{\text{miss}}$	> 13	> 13	> 10	> 13	> 10
m_{T} [GeV]	> 180	$[30, 90] / [90, 120]$	> 120	$[30, 90] / [90, 120]$	$[30, 120]$
$am_{\text{T}2}$ [GeV]	> 175	< 200	$< 200 / < 130$	> 200	> 200
$ \Delta\phi(\text{jet}_i, \vec{p}_{\text{T}}^{\text{miss}}) (i = 1, 2)$			> 0.7		
$m_W^{\text{reclustered}}$ [GeV]	> 50	> 50	W veto / > 50	W veto	W veto
$\Delta R(b_1, b_2)$	–	–	–	< 1.2	> 1.2
Lepton charge	–	–	–	$= +1$	–
$ \Delta\phi(j_{1,2}, \vec{p}_{\text{T}}^{\text{miss}}) $			> 0.4		
$m_{\text{T}2}^{\tau}$ based τ -veto [GeV]			> 80		
	<code>bC2x_med</code>	T1LCR/VR	T2LCR/VR	WCR/VR	STCR
Preselection		high- $E_{\text{T}}^{\text{miss}}$ preselection			
Number of (jets, b -tags)	$(\geq 4, \geq 2)$	$(\geq 4, \geq 2)$	$(\geq 4, \geq 1)$	$(\geq 4, \geq 1)$	$(\geq 4, \geq 2)$
Jet $p_{\text{T}} >$ [GeV]			$> (200, 140, 25, 25)$		
b -tagged jet $p_{\text{T}} >$ [GeV]	$> (140, 140)$	$> (140, 140)$	$> (140, -)$	$> (140, -)$	$> (140, 140)$
$E_{\text{T}}^{\text{miss}}$ [GeV]			> 230		
$H_{\text{T},\text{sig}}^{\text{miss}}$	> 10	> 10	> 10	> 10	> 6
m_{T} [GeV]	> 120	$[30, 90] / [90, 120]$	> 120	$[30, 90] / [90, 120]$	$[30, 120]$
$am_{\text{T}2}$ [GeV]	> 300	< 200	$< 200 / < 130$	> 200	> 200
$ \Delta\phi(\text{jet}_i, \vec{p}_{\text{T}}^{\text{miss}}) (i = 1, 2)$			> 0.9		
$m_W^{\text{reclustered}}$ [GeV]	> 50	> 50	W veto / > 50	W veto	W veto
$\Delta R(b_1, b_2)$	–	–	–	< 1.2	> 1.2
Lepton charge	–	–	–	$= +1$	–
$ \Delta\phi(j_{1,2}, \vec{p}_{\text{T}}^{\text{miss}}) $			> 0.4		
$m_{\text{T}2}^{\tau}$ based τ -veto [GeV]			> 80		

Figure 13 shows selected kinematic distributions of the CRs associated with `bCsoft_med`. The backgrounds are scaled with normalisation factors obtained from the simultaneous likelihood fit of the CRs as described in Section 10.

A set of VRs associated with corresponding CRs is also defined by inverting the requirement on $p_{\text{T}}^{\ell}/E_{\text{T}}^{\text{miss}}$. For the soft-lepton SRs, a STVR is defined together with the TVR and WVR. In Figure 13, selected kinematic distributions of the VRs associated with `bCsoft_high` are compared to the observed data. The backgrounds are scaled with normalisation factors. Table 19 and 20 detail the soft-lepton CR and VR

Table 18: Overview of the selections for the bC_bv signal region, as well as the associated control regions for $t\bar{t}$ (TCR) and W +jets (WCR), and the validation regions targeting $t\bar{t}$ (TVR) and W +jets (WVR) backgrounds. Round brackets are used to describe lists of values and square brackets denote intervals.

	bC _b v	TCR/VR	WCR/VR
Preselection	high- E_T^{miss} preselection		
Lepton p_T [GeV]		> 60	
Number of (jets, b -tags)	$(\geq 2, = 0)$	$(\geq 2, \geq 1)$	$(\geq 2, = 0)$
Jet p_T [GeV]		$> (120, 80)$	
b -tagged jet p_T [GeV]	$-$	> 25	$-$
E_T^{miss} [GeV]		> 360	
$H_{T,\text{sig}}^{\text{miss}}$		> 16	
m_T [GeV]	> 200	$[30, 90] / [90, 120]$	$[30, 90] / [90, 120]$
$ \Delta\phi(\text{jet}_i, \vec{p}_T^{\text{miss}}) (i = 1)$		> 2.0	
$ \Delta\phi(\text{jet}_i, \vec{p}_T^{\text{miss}}) (i = 2)$		> 0.8	
$\Delta\phi(\vec{p}_T^{\text{miss}}, \ell)$	> 1.2	$-$	$-$
$m_W^{\text{reclustered}}$ [GeV]		$[70, 100]$	
$ \Delta\phi(j_{1,2}, \vec{p}_T^{\text{miss}}) $		> 0.4	

Table 19: Overview of the selections for the bCsoft_diag and bffN signal regions, as well as the associated control regions for $t\bar{t}$ (TCR) and W +jets (WCR), and the validation regions targeting $t\bar{t}$ (TVR) and W +jets (WVR) backgrounds. Round brackets are used to describe lists of values and square brackets denote intervals. The veto on the reclustered hadronic top-quark candidate is satisfied for events where no reclustered jet candidate is found, or where the mass of the hadronic top-quark ($m_{\text{top}}^{\text{reclustered}}$) is below a certain threshold. The leading jet is required not to be b -tagged in all regions.

	bCsoft_diag/bffN	TCR/VR	WCR/VR
Preselection	soft-lepton preselection		
Number of (jets, b -tags)	$(\geq 2, \geq 1)$	$(\geq 2, \geq 1)$	$(\geq 2, = 1)$
Jet p_T [GeV]		$> (120, 25)$	
b -tagged jet p_T [GeV]		> 25	
E_T^{miss} [GeV]		> 300	
m_T [GeV]		< 160	< 160
$p_T^\ell/E_T^{\text{miss}}$	< 0.02	$[0.03, 0.10] / < 0.03$	$[0.03, 0.10] / < 0.03$
$m_{\text{top}}^{\text{reclustered}}$ [GeV]	top veto	> 150	top veto
$\min(\Delta\phi(\vec{p}_T^{\text{miss}}, b\text{-jet}_i))$	< 1.5	< 1.5	> 1.5
$ \Delta\phi(j_{1,2}, \vec{p}_T^{\text{miss}}) $		> 0.4	

selections.

Table 20: Overview of the selections for the `bCsoft_med` and `bCsoft_high` signal regions, as well as the associated control regions for $t\bar{t}$ (TCR) and W +jets (WCR), and the validation regions targeting $t\bar{t}$ (TVR) and W +jets (WVR) backgrounds. Round brackets are used to describe lists of values and square brackets denote intervals. The soft-lepton preselection as described in Table 4 is applied to the signal regions.

	<code>bCsoft_med</code>	TCR/VR	WCR/VR	STCR/VR
Preselection	soft-lepton preselection			
Number of (jets, b -tags)	$(\geq 3, \geq 2)$	$(\geq 3, \geq 2)$	$(\geq 3, = 1)$	$(\geq 3, \geq 2)$
Jet p_T [GeV]			$> (120, 60, 40, 25)$	
b -tagged jet p_T [GeV]	$> (120, 60)$	$> (120, 60)$	> 120	$> (120, 60)$
E_T^{miss} [GeV]			> 230	
m_T [GeV]			< 160	
p_T^W [GeV]			> 400	
$p_T^\ell/E_T^{\text{miss}}$	< 0.03	$> 0.03 / < 0.03$	$> 0.20 / [0.1, 0.2]$	$> 0.20 / [0.1, 0.2]$
am_{T2} [GeV]	> 200	< 200	> 200	> 200
$\min(\Delta\phi(\vec{p}_T^{\text{miss}}, b\text{-jet}_i))$	> 0.8	—	$[0.8, 2.5]$	> 0.8
$\Delta R(b_1, b_2)$	—	—	—	> 1.2
$ \Delta\phi(j_{1,2}, \vec{p}_T^{\text{miss}}) $			> 0.4	
	<code>bCsoft_high</code>	TCR/VR	WCR/VR	STCR/VR
Preselection	soft-lepton preselection			
Number of (jets, b -tags)	$(\geq 2, \geq 2)$	$(\geq 2, \geq 2)$	$(\geq 2, = 1)$	$(\geq 2, \geq 2)$
Jet p_T [GeV]			$> (100, 100)$	
b -tagged jet p_T [GeV]			$> (100, 100)$	
E_T^{miss} [GeV]			> 230	
m_T [GeV]			< 160	
p_T^W [GeV]			> 500	
$p_T^\ell/E_T^{\text{miss}}$	< 0.03	$> 0.10 / < 0.10$	$[0.1, 0.4] / < 0.10$	$> 0.30 / [0.1, 0.3]$
am_{T2} [GeV]	> 300	< 300	> 300	> 300
$\min(\Delta\phi(\vec{p}_T^{\text{miss}}, b\text{-jet}_i))$			> 0.4	
$\Delta R(b_1, b_2)$	> 0.8	> 0.8	—	> 0.8
$\Delta R(b, \ell)$	—	—	> 0.8	—
$ \Delta\phi(j_{1,2}, \vec{p}_T^{\text{miss}}) $			> 0.4	

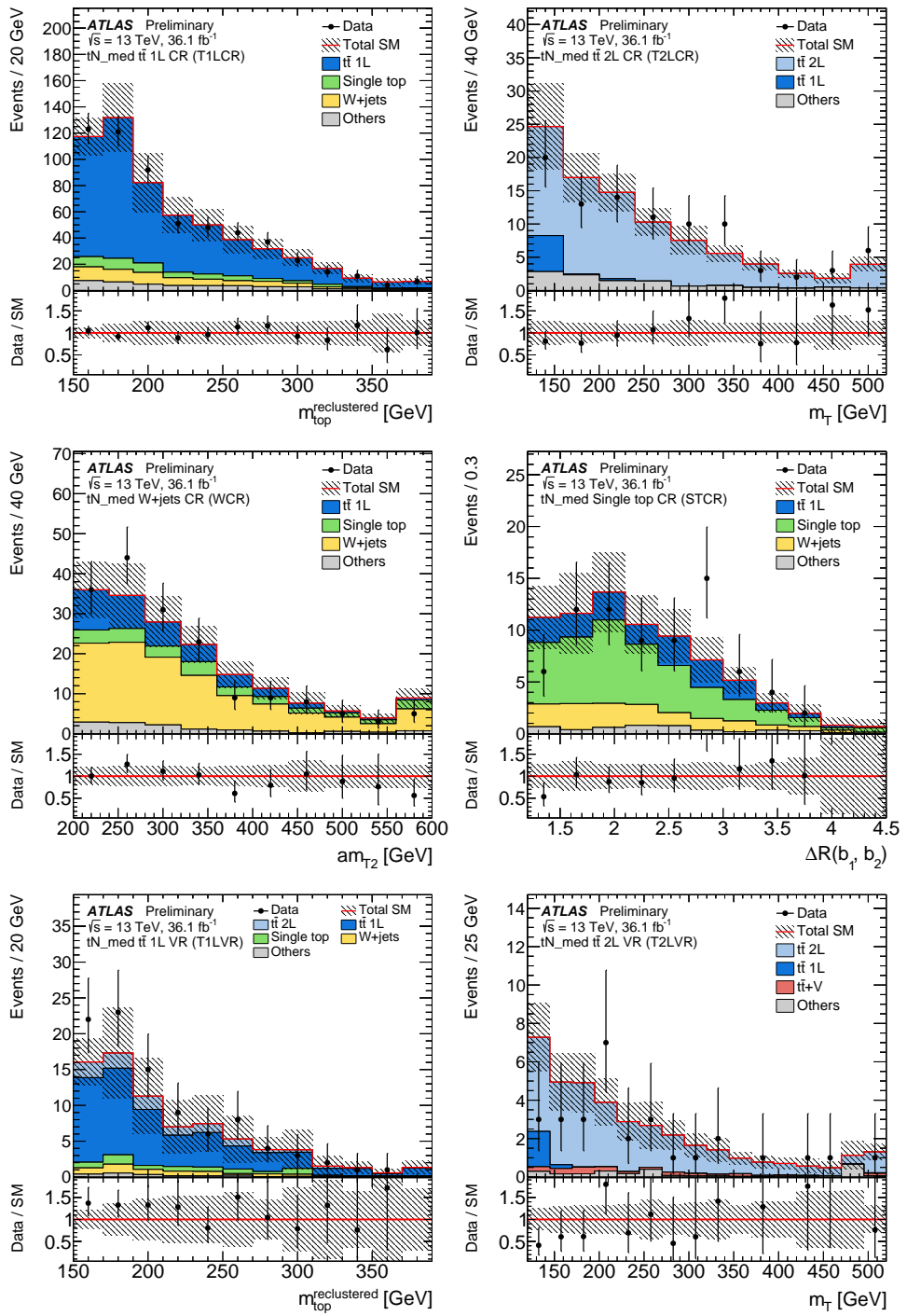


Figure 9: Various kinematic distributions in the tN_{med} control and validation regions: (top left) reclustered jet mass ($m_{\text{top}}^{\text{reclustered}}$) in the semi-leptonic $t\bar{t}$ control region, (top right) m_T in the dileptonic $t\bar{t}$ control region, (middle left) am_{T2} in the W +jets control region, (middle right) $\Delta R(b_1, b_2)$ in the single-top control region, (bottom left) reclustered jet mass ($m_{\text{top}}^{\text{reclustered}}$) in the semi-leptonic $t\bar{t}$ validation region, and (bottom right) m_T in the dileptonic $t\bar{t}$ validation region. Each of those backgrounds is scaled by normalisation factors obtained from a simultaneous likelihood fit of the CRs. The category labelled ‘Others’ stands for minor SM backgrounds that contribute less than 5% of the total SM background. The hashed area around the total SM prediction and the hashed band in the Data/SM ratio include statistical and experimental uncertainties. The last bin contains overflows.

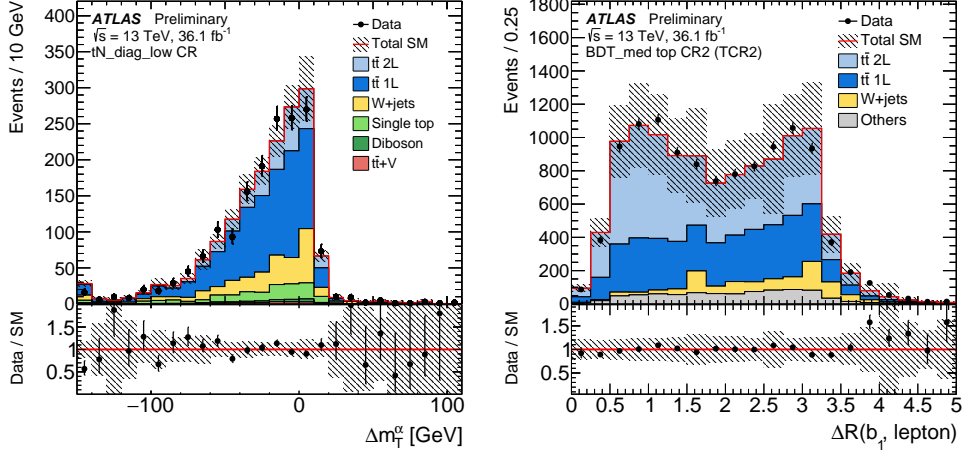


Figure 10: Kinematic distributions of the $tN_{\text{diag_low}}$ and $tN_{\text{diag_med}}$ control regions: (left) Δm_T^α in the $tN_{\text{diag_low}}$ top control region (TCR) and (right) $\Delta R(b_1, \ell)$ in the $tN_{\text{diag_med}}$ top control region (TCR2). Values of $m_{\tilde{t}_1} = 200$ GeV and $m_{\tilde{\chi}_1^0} = 27$ GeV are used, resulting in $\alpha = 0.135$. The $t\bar{t}$ background is scaled by a normalisation factor obtained from the control region. The category labelled ‘Others’ stands for minor SM backgrounds that contribute less than 5% of the total SM background. The hashed area around the total SM prediction and the hashed band in the Data/SM ratio include statistical and experimental uncertainties. The last bin contains overflows.

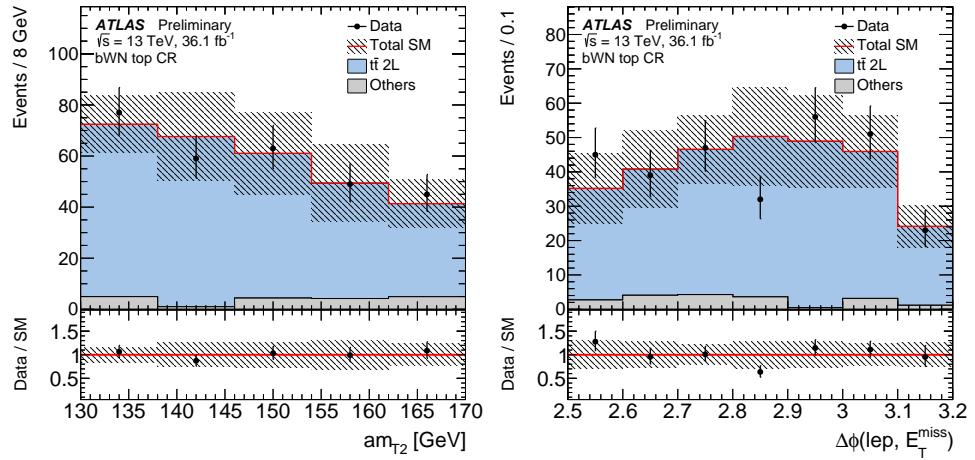


Figure 11: Kinematic distributions of the bWN top control region (TCR): (left) am_{T2} (right) and $\Delta\phi(p_T^{\text{miss}}, \ell)$. The $t\bar{t}$ process is scaled by a normalisation factor obtained in the corresponding control region. The category labelled ‘Others’ stands for minor SM backgrounds that contribute less than 5% of the total SM background. The hashed area around the total SM prediction and the hashed band in the Data/SM ratio include statistical and experimental uncertainties. The last bin contains overflows.

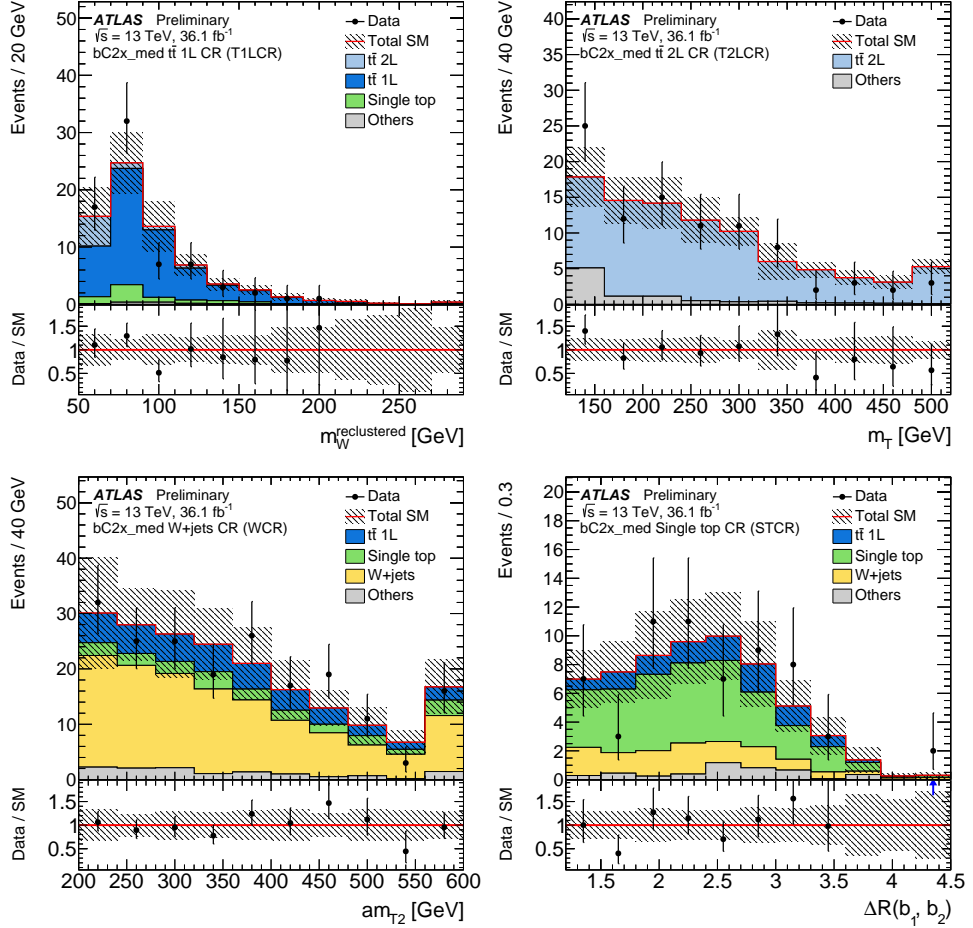


Figure 12: Kinematic distribution of the $bC2x_med$ control regions: (top left) reclustered jet mass ($m_W^{\text{reclustered}}$) in the semi-leptonic $t\bar{t}$ control region, (top right) m_T in the dileptonic $t\bar{t}$ control region, (bottom left) am_{T2} in the W -jets control region, and (bottom right) $\Delta R(b_1, b_2)$ in the single-top control region. Each of these backgrounds is scaled by normalisation factors obtained from the corresponding control region. The category labelled ‘Others’ stands for minor SM backgrounds that contribute less than 5% of the total SM background. The hashed area around the total SM prediction and the hashed band in the Data/SM ratio include statistical and experimental uncertainties. The last bin contains overflows.

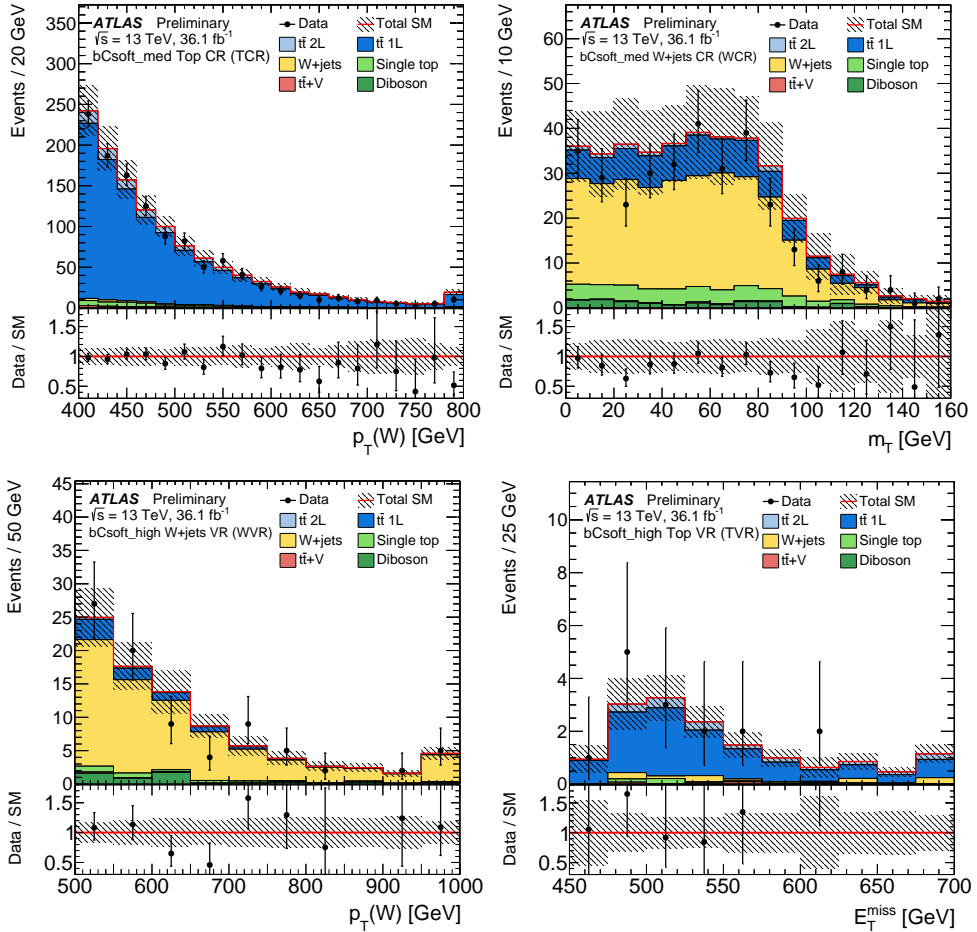


Figure 13: Kinematic distributions of the control regions associated with bCsoft_med and the validation regions associated with bCsoft_high: (top left) p_T^W in the top control region, (top right) m_T in the $W+jets$ control region, (bottom left) p_T of the leptonically decaying W -boson (p_T^W) in the $W+jets$ validation region, and (bottom right) E_T^{miss} in the top validation region. Each of those backgrounds is scaled by normalisation factors obtained from the corresponding control region. The hashed area around the total SM prediction and the hashed band in the Data/SM ratio include statistical and experimental uncertainties. The last bin contains overflows.

8.6 Control regions for $t\bar{t} + W/Z$

Top-quark pair production in association with a Z boson that decays into neutrinos is an irreducible background to the $t\bar{t} + E_T^{\text{miss}}$ signature. In order to estimate the $t\bar{t} + Z$ contribution in the SRs, Z boson decays to charged leptons are exploited to define high-purity CRs (TZCR). The $t\bar{t} + W/Z$ CRs require exactly three loose signal leptons, at least one of which must also satisfy the tight criteria. Two leptons are required to have same flavour and opposite charge, and the mass of the dilepton system ($m_{\ell\ell}$) is required to be in the range $81 \text{ GeV} < m_{\ell\ell} < 101 \text{ GeV}$. In addition, at least four jets, one of which is b -tagged, are required. The minimum jet p_T of the four leading jets is required to match the thresholds used in the corresponding SR. The diboson process ($WZ \rightarrow \ell\nu\ell\ell$) is a dominant background in the TZCR, and is normalised to data in a region identical to the TZCR, except for the requirement that no jet is b -tagged. A constant diboson normalisation factor of 0.8, derived in this region, is applied to all TZCRs.

The $t\bar{t} + Z$ control region is defined for SRs where the $t\bar{t} + Z$ contribution is sizeable: tN_{med} , tN_{high} , $bC2x_{\text{med}}$, $bC2x_{\text{diag}}$, DM_{low} , and DM_{high} . The purity of the TZCR is $\approx 75\%$, with remaining events due to diboson and tZ single-top production. Figure 14 shows the $p_T^{\ell\ell}$ distribution in the TZCR associated to tN_{med} , as well as $m_{\ell\ell}$ prior to the cut. The $t\bar{t} + Z(\ell\ell)$ method is cross-checked with an alternative method using the $t\bar{t} + \gamma$ process.

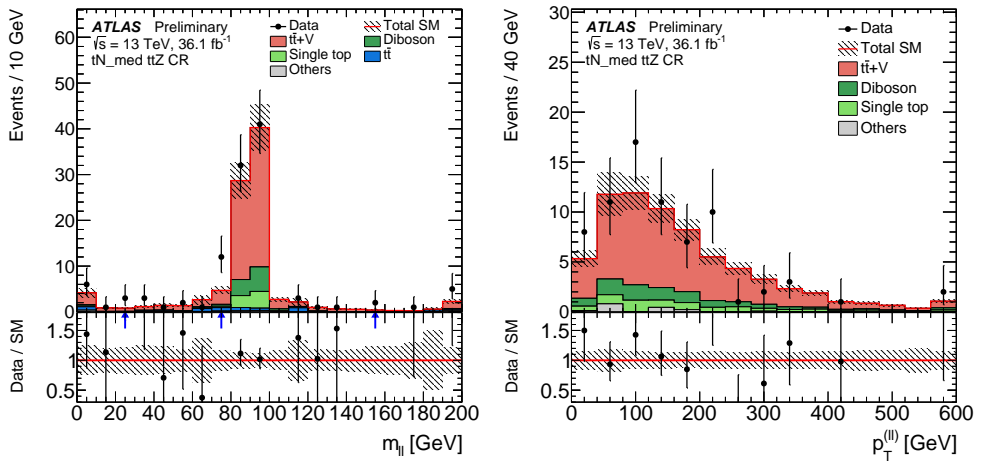


Figure 14: Distribution of (left) the dilepton mass and (right) $p_T^{\ell\ell}$ corresponding to the p_T of the reconstructed Z boson in the $t\bar{t} + Z$ control region (TZCR) associated to the tN_{med} signal region. The $t\bar{t} + Z/W$ processes are normalised in the TZCR. The diboson background is normalised to data events with zero b -tagged jets. The hashed area around the total SM prediction and the hashed band in the Data/SM ratio include statistical and experimental uncertainties. The last bin contains overflows.

9 Systematic uncertainties

The systematic uncertainties in the signal and background estimates arise both from experimental sources and from the uncertainties in the theoretical predictions and modelling. Since the yields from the dominant background sources, $t\bar{t}$, single top, $t\bar{t}V$, and $W+\text{jets}$, are all obtained in dedicated CRs, the uncertainties for these processes affect only the extrapolation from the CRs into the SRs (and amongst the various CRs), but not the overall normalisation. The systematic uncertainties are included as nuisance parameters with

Gaussian constraints and profiled in the likelihood fits. The uncertainties are not reduced as a result of the profiling.

The dominant experimental uncertainties arise from imperfect knowledge of the jet energy scale (JES) and jet energy resolution (JER) [128, 149], the modelling of the b -tagging efficiencies and mistag rates [150, 151], as well as the contribution of the E_T^{miss} soft term. From these sources, the resulting uncertainties expressed as relative uncertainties on the total predicted background yield in the SRs are in the range 1.4–7% for JES, 1.5–7% for JER, 1.6–13% for b -tagging, and 0.8–7% for the E_T^{miss} soft term. Other sources of experimental uncertainty include the modelling of the lepton energy scales, energy resolutions, reconstruction and identification efficiencies, trigger efficiencies, and the modelling of pileup and the integrated luminosity. These uncertainties have a small impact on the final results.

The uncertainties in the modelling of the single-top and $t\bar{t}$ backgrounds include effects related to the MC event generator, the hadronisation and fragmentation modelling, and the amount of initial- and final-state radiation [101]. The MC generator uncertainty is estimated by comparing events produced with Powheg-Box+Herwig++ v2.7.1 with either MG5_aMC@NLO v2.2.3+Herwig++ v2.7.1 (NLO) or SHERPA v2.2. Events generated with Powheg-Box are hadronised with either Pythia6 or Herwig++ to estimate the effect from the modelling of the fragmentation and hadronisation. The impact of altering the amount of initial- and final-state radiation is estimated from comparisons of Powheg-Box+Pythia6 samples with different parton-shower radiation, NLO radiation, and modified factorisation and renormalisation scales. An additional uncertainty stems from the modelling of the interference between the $t\bar{t}$ and Wt processes. The uncertainty is estimated using inclusive $WWbb$ events, generated using MG5_aMC@NLO v2.2.3 (LO), which are compared with the sum of the resonant $t\bar{t}$ and Wt processes [101]. The resulting uncertainties from all the aforementioned sources on the CR to SR extrapolation factors from the $t\bar{t}$ and Wt CRs to the SRs are 10–45% for $t\bar{t}$, and 10–47% for Wt events, where the latter is dominated by the interference term.

The uncertainty on the modelling of the $t\bar{t} + Z$ background is estimated from independent variations of the renormalisation and factorisation scales, and PDF variations. A MC generator uncertainty is estimated by comparing events produced with MG5_aMC@NLO v2.2.3+Pythia8 (NLO) and SHERPA v2.2. The resulting modelling uncertainties on the extrapolation factors are 10–37%, dominated by the MC generator comparison.

The uncertainty on the W +jets background from the choice of MC generator is estimated by comparing SHERPA with MG5_aMC@NLO v2.2.3+Pythia8 (NLO). In addition, the effects of varying the scales for the matching scheme related to the merging of matrix elements and parton showers, renormalisation, factorisation, and resummation are estimated. The total uncertainty is found to be 4–44%.

The sources of uncertainty considered for the diboson background are the effects of varying the renormalisation, factorisation, and resummation scales. Since the diboson background is not normalised in a CR, the analysis is also sensitive to the uncertainty in the total cross-section. The resulting theoretical uncertainty ranges from 13–32%.

For the BDT analyses, a smoothing procedure in BDT score is applied to evaluate the uncertainties on the modelling of $t\bar{t}$ and single-top Wt processes. The procedure gives a reliable estimate of the uncertainties against the statistical fluctuations of the background samples, based on merging statistically insignificant bins and smoothing the result with a gaussian kernel.

The SUSY signal cross-section uncertainty is taken from an envelope of cross-section predictions using different PDF sets and factorisation and renormalisation scales, as described in Ref. [94], and the resulting

uncertainties range from 13% to 23%. The uncertainty on the DM production cross-section is estimated from the effect of varying the renormalisation, factorisation, and matching scales, as well as the PDF choice. The uncertainty is found to be between 12% and 20%.

Table 21 summarises the dominant systematic uncertainties in selected signal regions. The dominant source of uncertainties are background modelling and JES/JER uncertainties in most of SRs. The contribution of mis b -tagged jet becomes large in the `bCsoft_med`. This is because the single-top Wt or semi-leptonic $t\bar{t}$ backgrounds going over the am_{T2} endpoint often have an associated charm-quark mis-identified as a b -tagged jet.

Table 21: Summary of the dominant systematic uncertainties on the total predicted background yields, obtained by the background-fits as described in Section 10.1, in several representative signal regions: `tN_med`, `bWN`, `bC2x_med`, and `bCsoft_med`. Numbers are given as percentages of the total background estimate.

Signal region	<code>tN_med</code>	<code>bWN</code>	<code>bC2x_med</code>	<code>bCsoft_med</code>
$t\bar{t}Z$ modelling	10.6	2.3	1.2	< 1.0
$t\bar{t}$ radiation	4.3	12.8	1.9	4.6
$t\bar{t}$ generator	3.6	7.8	1.7	4.6
$t\bar{t}$ fragmentation	2.5	12.1	5.8	3.9
$Wt - t\bar{t}$ interference	< 1.0	< 1.0	12.6	< 1.0
single-top generator	< 1.0	< 1.0	4.9	< 1.0
single-top fragmentation	< 1.0	< 1.0	10.6	< 1.0
diboson modelling	10.6	< 1.0	< 1.0	< 1.0
JER	2.8	1.5	6.8	2.4
JES	2.8	6.6	1.4	2.1
mis b -tag (c)	2.3	1.6	4.9	12.8
mis b -tag (l)	2.0	< 1.0	2.0	4.6
pile-up	2.5	1.2	3.8	2.0
E_T^{miss} soft-term	< 1.0	< 1.0	1.7	7.1
Total systematic uncertainty	18.2	22.2	27.7	15.1

10 Results

10.1 Observed data and predicted backgrounds

In order to determine the SM background yields in the SRs, a likelihood fit is performed for each SR. The fit can be configured to use only the CRs to constrain the fit parameters corresponding to the normalisations of $t\bar{t}$, single-top, W +jets, and $t\bar{t} + W/Z$ processes in the dedicated CRs. This fit configuration is referred to as the background-only fit.

The number of observed events and the predicted number of SM background events from the background-only fits in all SRs and VRs are shown in Figures 15 and 16. The set of SRs are not mutually exclusive and are therefore not statistically independent among themselves. In all SRs, the distributions indicate good compatibility between the data and the SM background estimate. The largest excesses over the

background-only hypothesis are 1.6σ and 1.4σ , observed in `tN_high` and `tN_med`, respectively. The previously observed excess of 3.3σ in `DM_low_loose` is reduced with the inclusion of more data to the level of 1.5σ .

The number of observed events together with the predicted number of SM background events in all 16 SRs are summarised in Tables 22 and 23, showing the breakdown of the various backgrounds that contribute to the SRs. The tables also list the results for the four fit parameters that control the normalisation of the four main backgrounds (normalisation factors, NFs), together with the associated fit uncertainties including the theoretical modelling uncertainties. To quantify the compatibility of the SM background-only hypothesis with the observations in the SRs, a profile likelihood ratio test is performed. All limits are calculated using the CL_s prescription [152]. The resulting p -values (p_0) are also presented in the tables. Table 24 also details the number of observed events and the predicted number of SM background events for each bin of the shape-fit SRs. The NFs are compatible with the unity in most cases, except for the single-top NFs in `bCsoft_med` and `bCsoft_high`. The single-top NFs are significantly below unity, possibly due to the effect of Wt interference with $t\bar{t}$ events at the NLO.

Figures 17, 18, and 19 show comparisons between the observed data and the SM background prediction with all SR selections applied except the requirement on the plotted variable. The expected distributions from representative signal benchmark models are overlaid.

10.2 Exclusion limits

As no significant excess is observed, exclusion limits are set based on profile-likelihood fits for the stop pair production models and the simplified model for top-quarks produced in association with dark matter particles.

The signal uncertainties and potential signal contributions to all regions are taken into account. All uncertainties except those on the theoretical signal cross-section are included in the fit. Exclusion limits at 95% CL are obtained by selecting *a priori* the signal region with the lowest expected CL_s value for each signal model and the exclusion contours are derived by interpolating in the CL_s value.

Figures 20 and 21 show the expected and observed exclusion contours as a function of stop and neutralino mass for the pure bino LSP scenario. The $\pm 1\sigma_{\text{exp}}$ uncertainty band indicates the impact on the expected limit of the systematic and statistical uncertainties included in the fit. The $\pm 1\sigma_{\text{theory}}^{\text{SUSY}}$ uncertainty lines around the observed limit illustrate the change in the observed limit as the nominal signal cross-section is scaled up and down by the theoretical cross-section uncertainty. The exclusion limits are obtained under the hypothesis of mostly right-handed stops in the pure bino LSP scenario.

The results extend previous exclusion limits by excluding the stop mass region up to 940 GeV for a massless lightest neutralino under the assumption of $\text{BR}(\tilde{t}_1 \rightarrow t\tilde{\chi}_1^0) = 100\%$. In the three-body scenario, stop masses are excluded up to 500 GeV for a LSP mass of about 300 GeV. In the four-body scenario, stop masses are excluded up to 370 GeV for a mass splitting between the stop and the LSP down to 20 GeV.

The non-excluded area between the three- and four-body decay regions is due to a reduction in search sensitivity as the kinematic properties of the signal change significantly when transitioning from a four-body to a three-body decay. In particular, approaching this boundary from the three-body side, the momenta of the two b -jets decrease to zero and hence the acceptance of the p_T requirement on the b -tagged jet in the bWN signal region decrease rapidly.

The kinematic properties change again at the kinematic boundary between the three-body and on-shell top-quark decay modes. When approaching this diagonal from the on-shell top-quark side, the search sensitivity usually worsens due to the difficulty in disentangling signal from the $t\bar{t}$ background. However, the dedicated BDT analysis (here in particular `tN_diag_high`) recovers the sensitivity.

Limits are also set on the masses of the \tilde{t}_1 and $\tilde{\chi}_1^0$ in the wino NLSP scenario. Figure 22 shows the exclusion contours based on the combination of all SRs targeting this scenario for positive and negative values of the μ parameter. The stop mass region up to 885 GeV (940 GeV) is excluded in scenarios with $\mu < 0$ ($\mu > 0$) and a 200 GeV neutralino. Figure 23 shows the exclusion limit for the simplified model $\tilde{t}_1 \rightarrow b\tilde{\chi}_1^\pm$ scenario with $m_{\tilde{t}_1} - m_{\tilde{\chi}_1^\pm} = 10$ GeV. The stop mass region is excluded up to 840 GeV for a massless neutralino.

Assuming the higgsino LSP scenario, limits are also set on the masses of the \tilde{t}_1 and $\tilde{\chi}_1^0$ as shown in Figures 24–26. In Figures 24 and 26, the exclusion contours are shown for various signal scenarios, $m_{tR} < m_{q3L}$, $m_{q3L} < m_{tR}$, and $m_{q3L} < m_{tR}$ with large $\tan\beta$ as described in Section 4, based on the combination of two orthogonal hard- and soft-lepton SRs. The stop decay branching ratios to $t\tilde{\chi}_1^0$, $b\tilde{\chi}_1^\pm$ and $t\tilde{\chi}_2^0$, vary in these three scenarios. In the scenario with $m_{tR} < m_{q3L}$, the sensitivity is mostly driven by the `bCsoft_med` and `bCsoft_high` SRs, as the branching ratio of the $\tilde{t}_1 \rightarrow b\tilde{\chi}_1^\pm$ decay (with soft-leptons) is large, whereas the sensitivity is driven by the `tN_med` SR for the scenario with $m_{q3L} < m_{tR}$, as the branching ratio of the $\tilde{t}_1 \rightarrow t\tilde{\chi}_1^0$ and $\tilde{t}_1 \rightarrow t\tilde{\chi}_2^0$ decays (with high p_T leptons from the leptonically decaying top-quark) are dominant. The third scenario, $m_{q3L} < m_{tR}$ with large $\tan\beta$, benefits from both soft- and hard-lepton SRs, with equal branching ratios to all three decay modes.

In Figure 25, the $\tilde{t}_1 \rightarrow b\tilde{\chi}_1^\pm$ decay is considered with 100% branching ratio, and the exclusion limit is set by a single soft-lepton SR, `bCsoft_diag`. In the gaps between the exclusion contour and diagonal dashed lines indicating the kinematic boundaries ($m_{\tilde{t}_1} = m_b + m_{\tilde{\chi}_1^\pm}$ and $m_{\tilde{t}_1} = m_t + m_{\tilde{\chi}_1^0}$), the simplified model may not be accurate due to the phase-space effects, hence these regions are not considered in the interpretation.

In Figures 24 and 25, $\Delta m(\tilde{\chi}_1^0, \tilde{\chi}_1^\pm)$ is fixed to 5 GeV and $\Delta m(\tilde{\chi}_1^0, \tilde{\chi}_2^0)$ is fixed to 10 GeV. In Figure 26, the mass relation $\Delta m(\tilde{\chi}_2^0, \tilde{\chi}_1^0) = 2 \times \Delta m(\tilde{\chi}_1^\pm, \tilde{\chi}_1^0)$ and $m_{\tilde{\chi}_1^\pm} = 150$ GeV are assumed, while $\Delta m(\tilde{\chi}_1^\pm, \tilde{\chi}_1^0)$ is varied between 0 GeV and 30 GeV. For the region below $\Delta m(\tilde{\chi}_1^\pm, \tilde{\chi}_1^0) = 2$ GeV, only the $\tilde{t}_1 \rightarrow t\tilde{\chi}_1^0$ process is simulated, with the branching ratio set to account for both $\tilde{t}_1 \rightarrow t\tilde{\chi}_1^0$ and $\tilde{t}_1 \rightarrow t\tilde{\chi}_2^0$ decays. In Figure 24, the stop mass region up to 890 GeV (800 GeV) is excluded in scenarios with $m_{q3L} < m_R$ ($m_R < m_{q3L}$).

Limits are also set on the masses of the \tilde{t}_1 and $\tilde{\chi}_1^0$ in the well-tempered neutralino scenario. Figure 27 shows the exclusion contours based on the combination of all SRs for two signal scenarios. In the scenario with $m_{q3L} < m_{tR}$, the expected sensitivity is better than the scenario with $m_{tR} < m_{q3L}$ as sbottom pair production can also contribute to the $m_{q3L} < m_{tR}$ scenario, roughly doubling the signal acceptance. No observed limit is set in the $m_{tR} < m_{q3L}$ scenario, as a mild excess of observed data is seen above the predicted SM background yield in the `bCsoft_high` SR (shape-fit, as shown in Figure 19), which drives the sensitivity for this scenario. On the other hand, the stop mass region up to 810 GeV is excluded in scenarios with $m_{q3L} < m_{tR}$.

Figure 28 shows the upper limit on the ratio of the DM+ $t\bar{t}$ production cross-section to the theoretical cross-section. Limits are shown under the hypothesis of a scalar or pseudoscalar mediator, and for a fixed DM candidate mass or for a fixed mediator mass. A scalar (pseudo-scalar) mediator mass of up to

65 GeV (220 GeV) is excluded at 95% confidence level, assuming a 1 GeV dark matter particle mass and a common coupling to SM and dark matter particles of $g = 1$.

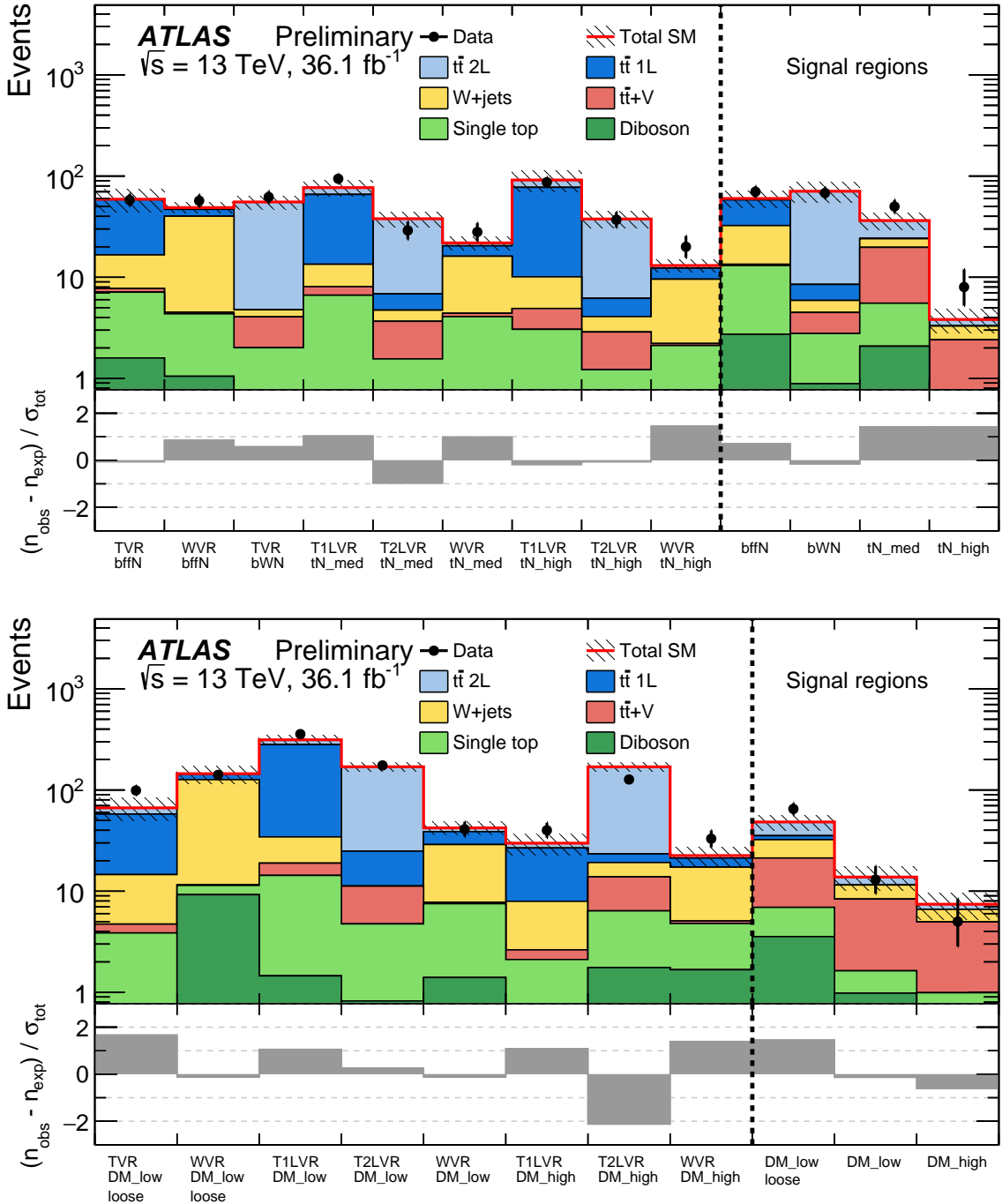


Figure 15: Comparison of the observed data (n_{obs}) with the predicted SM background (n_{exp}) in (top) the tN_{med} , tN_{high} , bWN and $bffN$ signal regions, and (bottom) the $DM_{\text{low_loose}}$, DM_{low} , and DM_{high} signal regions, and associated VRs. The background predictions are obtained using the background-only fit configuration, and the hashed area around the SM prediction includes all uncertainties. The bottom panels show the difference between data and the predicted SM background divided by the total uncertainty (σ_{tot}).

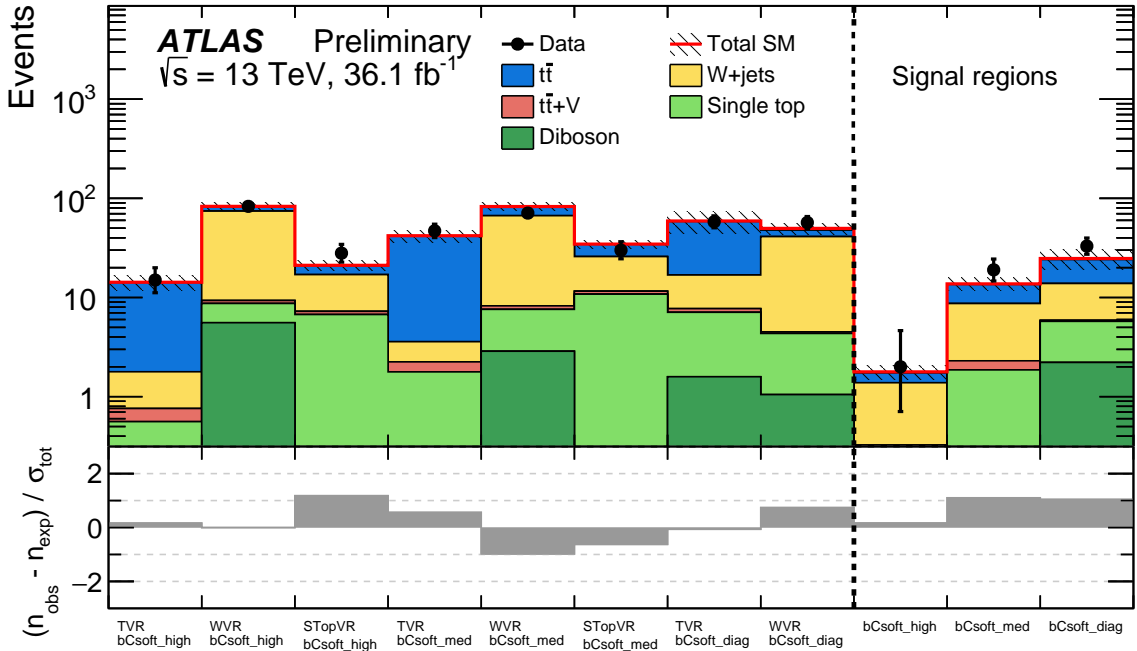
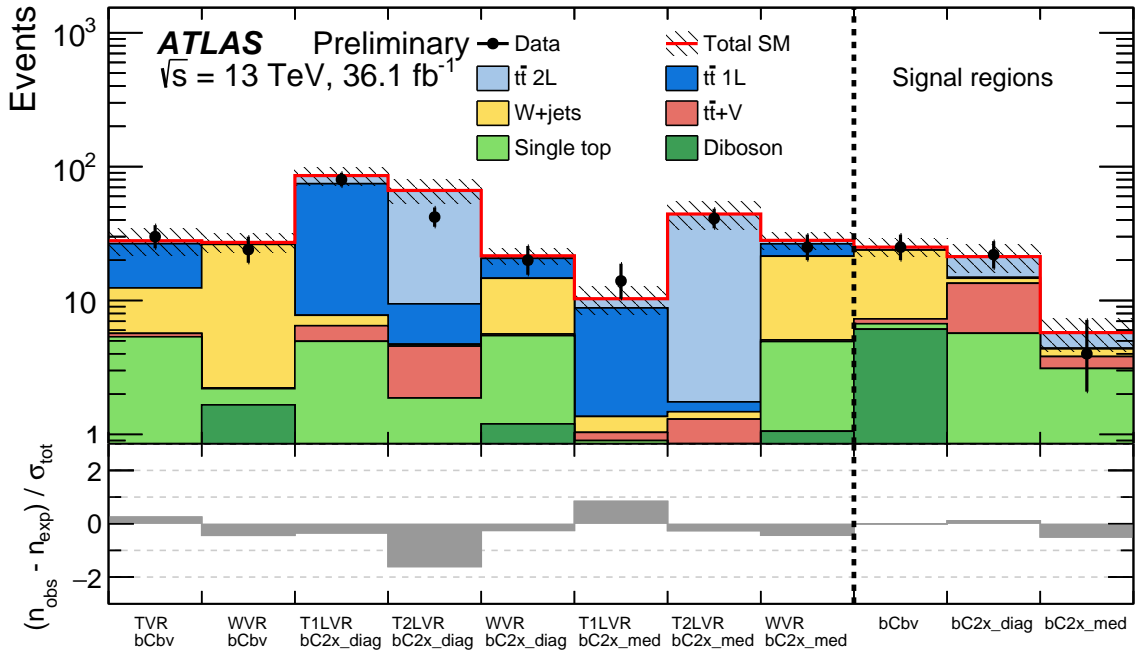


Figure 16: Comparison of the observed data (n_{obs}) with the predicted SM background (n_{exp}) in (top) the $b\text{C}2x_{\text{med}}$, $b\text{C}2x_{\text{diag}}$, and $b\text{C}b\text{v}$ signal regions, (bottom) the $b\text{C}soft_{\text{diag}}$, $b\text{C}soft_{\text{med}}$, and $b\text{C}soft_{\text{high}}$ signal regions, together with associated VRs. The background predictions are obtained using the background-only fit configuration, and the hashed area around the SM prediction includes all uncertainties. The bottom panels show the difference between data and the predicted SM background divided by the total uncertainty (σ_{tot}).

Table 22: The numbers of observed events in the pure bino LSP discovery SRs together with the expected numbers of background events and their uncertainties as predicted by the background-only fits, the normalisation factors (NF) for the background predictions obtained in the fit, and the probabilities (represented by p_0 values) that the observed numbers of events are compatible with the background-only hypothesis.

Signal region	tN_high	tN_med	tN_diag_high	tN_diag_med	tN_diag_low	bWN	bffN
Observed	8	50	6	115	34	68	70
Total background	3.8 ± 1.0	36.3 ± 6.6	7.4 ± 1.6	115 ± 31	30.3 ± 5.9	71 ± 16	60.5 ± 6.1
$t\bar{t} 2\ell$	0.51 ± 0.18	12.1 ± 2.9	6.51 ± 0.87	65.1 ± 9.4	8.5 ± 2.3	65 ± 16	25.5 ± 5.5
$t\bar{t} 1\ell$	0.020 ± 0.001	0.19 ± 0.05	-	35.0 ± 8.9	17.5 ± 4.1	-	-
$t\bar{t} + W/Z$	1.86 ± 0.90	14.2 ± 5.5	0.23 ± 0.08	2.5 ± 1.6	0.34 ± 0.20	1.7 ± 1.7	0.35 ± 0.06
Single top	0.13 ± 0.10	3.5 ± 1.2	0.54 ± 0.21	8.1 ± 1.1	2.3 ± 1.2	$1.9^{+2.0}_{-1.9}$	10.3 ± 4.4
$W + \text{jets}$	0.88 ± 0.24	4.3 ± 1.1	0.09 ± 0.08	3.8 ± 1.9	$1.7^{+2.0}_{-1.7}$	1.41 ± 0.88	19.6 ± 4.9
Diboson	0.42 ± 0.16	2.08 ± 0.70	0.07 ± 0.02	$0.69^{+0.73}_{-0.69}$	$0.07^{+0.24}_{-0.07}$	0.89 ± 0.28	2.72 ± 0.99
$Z + \text{jets}$	-	-	-	-	-	-	1.9 ± 1.8
$t\bar{t} 2\ell$ NF	1.01 ± 0.15	0.96 ± 0.13	1.05 ± 0.06	1.16 ± 0.16	0.85 ± 0.10	1.04 ± 0.07	-
$t\bar{t} 1\ell$ NF	0.97 ± 0.08	1.05 ± 0.09	-	1.16 ± 0.28	0.85 ± 0.10	1.04 ± 0.07	0.73 ± 0.11
$t\bar{t} + W/Z$ NF	1.11 ± 0.35	1.13 ± 0.32	-	-	-	-	-
Single top NF	0.64 ± 0.37	1.19 ± 0.37	-	-	-	-	-
$W + \text{jets}$ NF	0.82 ± 0.17	0.85 ± 0.18	-	-	-	-	1.19 ± 0.26
$p_0 (\sigma)$	$0.05 (1.6)$	$0.07 (1.4)$	$0.5 (0)$	$0.5 (0)$	$0.33 (0.46)$	$0.5 (0)$	$0.17 (0.95)$
$N_{\text{non-SM exp.}}^{\text{limit}}$	5.8	19	6.1	58	19	33	21
$N_{\text{non-SM obs.}}^{\text{limit}}$	10	31	7.2	58	17	31	28

Table 23: The numbers of observed events in DM+ $t\bar{t}$, wino NLSP, bC_b, and higgsino LSP discovery SRs together with the expected numbers of background events and their uncertainties as predicted by the background-only fits, the normalisation factors (NF) for the background predictions obtained in the fit, and the probabilities (represented by p_0 values) that the observed numbers of events are compatible with the background-only hypothesis.

Signal region	DM_high	DM_low	DM_low_loose	bC2x_diag	bC2x_med	bC _b	bCsoft_diag	bCsoft_med	bCsoft_high
Observed	5	13	65	22	4	25	33	19	2
Total background	7.4 ± 2.1	13.8 ± 3.6	48.3 ± 8.2	21.3 ± 5.0	5.8 ± 1.6	25.1 ± 3.8	24.7 ± 3.1	13.7 ± 2.1	1.8 ± 0.3
$t\bar{t} 2\ell$	0.82 ± 0.27	2.21 ± 0.58	16.0 ± 5.7	6.4 ± 2.4	1.36 ± 0.49	1.25 ± 0.65	10.3 ± 2.4	4.9 ± 1.5	0.36 ± 0.15
$t\bar{t} 1\ell$	0.0 ± 0.0	0.07 ± 0.03	-	0.28 ± 0.18	$0.04^{+0.13}_{-0.04}$	-	-	-	-
$t\bar{t} + W/Z$	4.0 ± 2.0	6.7 ± 3.2	14.3 ± 5.9	7.8 ± 3.3	0.71 ± 0.38	0.58 ± 0.16	0.14 ± 0.06	0.44 ± 0.10	0.05 ± 0.02
Single top	0.33 ± 0.16	0.65 ± 0.57	3.4 ± 1.3	5.5 ± 2.4	3.0 ± 1.5	0.60 ± 0.54	3.5 ± 1.5	1.6 ± 0.5	0.23 ± 0.11
$W + \text{jets}$	1.64 ± 0.53	3.2 ± 1.3	11.0 ± 2.8	1.22 ± 0.35	0.54 ± 0.14	16.5 ± 3.1	8.0 ± 2.0	6.4 ± 2.0	1.06 ± 0.24
Diboson	0.66 ± 0.21	0.98 ± 0.33	3.6 ± 1.3	0.23 ± 0.08	0.07 ± 0.04	6.1 ± 2.0	2.21 ± 0.93	0.31 ± 0.16	0.04 ± 0.01
$Z + \text{jets}$	-	-	-	-	-	-	0.60 ± 0.55	0.17 ± 0.16	0.04 ± 0.04
$t\bar{t} 2\ell$ NF	1.19 ± 0.13	1.06 ± 0.12	1.13 ± 0.21	1.28 ± 0.17	1.58 ± 0.22	0.78 ± 0.28	0.73 ± 0.11	0.92 ± 0.07	0.93 ± 0.16
$t\bar{t} 1\ell$ NF	1.08 ± 0.14	0.95 ± 0.04	1.13 ± 0.21	0.96 ± 0.08	0.75 ± 0.15	0.78 ± 0.28	0.73 ± 0.11	0.92 ± 0.07	0.93 ± 0.16
$t\bar{t} + W/Z$ NF	0.98 ± 0.38	1.06 ± 0.38	1.10 ± 0.32	1.18 ± 0.39	0.95 ± 0.52	-	-	-	-
Single top NF	0.94 ± 0.37	1.05 ± 0.35	1.22 ± 0.27	1.59 ± 0.45	1.17 ± 0.37	-	-	0.47 ± 0.14	0.37 ± 0.15
$W + \text{jets}$ NF	1.08 ± 0.21	1.04 ± 0.18	0.93 ± 0.10	0.80 ± 0.24	1.11 ± 0.25	1.07 ± 0.09	1.19 ± 0.26	1.35 ± 0.24	1.11 ± 0.19
$p_0 (\sigma)$	0.5 (-)	0.5 (-)	0.07 (1.5)	0.45 (0.11)	0.5 (-)	0.5 (-)	0.25 (0.68)	0.12 (1.17)	0.44 (0.16)
$N_{\text{non-SM exp.}}^{\text{limit}}$	7.2	11	23	14	6.4	13	13	9.6	4.1
$N_{\text{non-SM obs.}}^{\text{limit}}$	5.7	10	37	14	5.2	13	20	14	4.3

Table 24: The numbers of observed events in each bin of the shape-fit SRs together with the expected numbers of total background events and their uncertainties as predicted by the background-only fits. The bin i ($i = 1 - 5$) corresponds to i -th bin (from left to right) of the variable used in the shape-fit. The bin boundaries of the shape-fits are detailed in Table 6, 7, 8, and 10.

Signal region	Fitted variable		bin1	bin2	bin3	bin4	bin5
tN_med	E_T^{miss}	Observed	21	17	8	4	–
		Total background	14.6 ± 2.8	11.2 ± 2.2	7.3 ± 1.7	3.16 ± 0.74	–
tN_diag_high BDT_high		Observed	40	41	19	–	–
		Total background	47.3 ± 3.6	37.5 ± 3.5	18.3 ± 2.2	–	–
tN_diag_med BDT_med		Observed	970	678	366	211	40
		Total background	886 ± 83	618 ± 86	440 ± 71	210 ± 30	51 ± 10
bWN	am_{T2}	Observed	13	19	22	30	36
		Total background	16.5 ± 4.5	16.0 ± 6.0	25.6 ± 5.3	40.1 ± 8.1	38.5 ± 8.3
bffN	$p_T^\ell/E_T^{\text{miss}}$	Observed	9	27	34	–	–
		Total background	4.6 ± 1.1	22.9 ± 3.1	32.5 ± 4.1	–	–
bCsoft_diag	$p_T^\ell/E_T^{\text{miss}}$	Observed	4	16	13	–	–
		Total background	1.69 ± 0.47	9.3 ± 2.1	13.6 ± 2.8	–	–
bCsoft_med	$p_T^\ell/E_T^{\text{miss}}$	Observed	4	15	57	–	–
		Total background	4.92 ± 0.90	8.9 ± 1.3	52.9 ± 6.2	–	–
bCsoft_high	$p_T^\ell/E_T^{\text{miss}}$	Observed	1	1	15	–	–
		Total background	0.67 ± 0.13	1.11 ± 0.22	6.98 ± 0.81	–	–

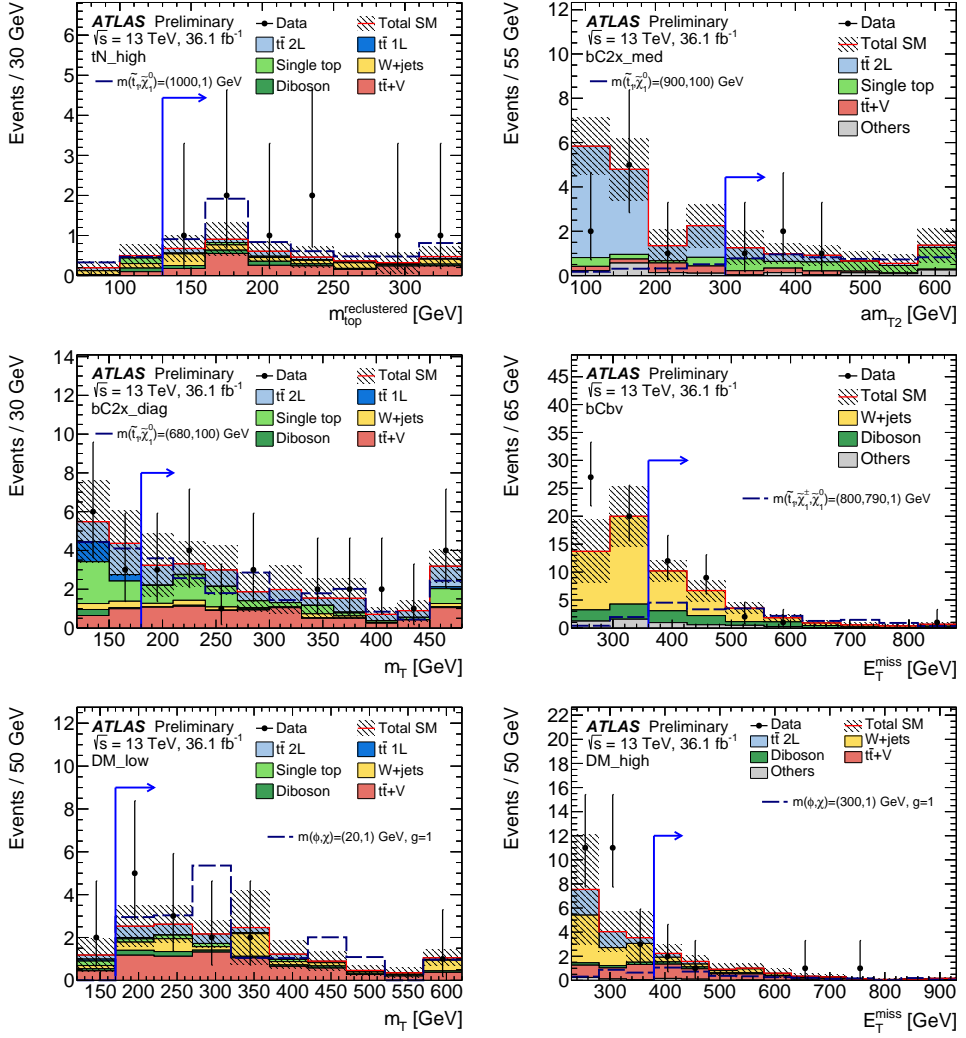


Figure 17: Kinematic distributions in the signal regions: (top left) $m_{\text{top}}^{\text{reclustered}}$ in tN_{high} , (top right) aM_{T2} in $bC2x_{\text{med}}$, (middle left) m_T in $bC2x_{\text{diag}}$, (middle right) E_T^{miss} in $bC bv$, (bottom left) m_T in DM_{low} , and (bottom right) E_T^{miss} in DM_{high} . The full event selection in the corresponding signal region is applied, except for the requirement (indicated by an arrow) that is imposed on the variable being plotted. The predicted SM backgrounds are scaled with the normalisation factors obtained from the corresponding control regions in Tables 22 and 23. In addition to the background prediction, a signal model is shown on each plot. In the $DM+t\bar{t}$ signal model a coupling of $g = 1$ is assumed. The category labelled ‘Others’ stands for minor SM backgrounds that contribute less than 5% of the total SM background. The hashed area around the total SM prediction includes statistical and experimental uncertainties. The last bin contains overflows.

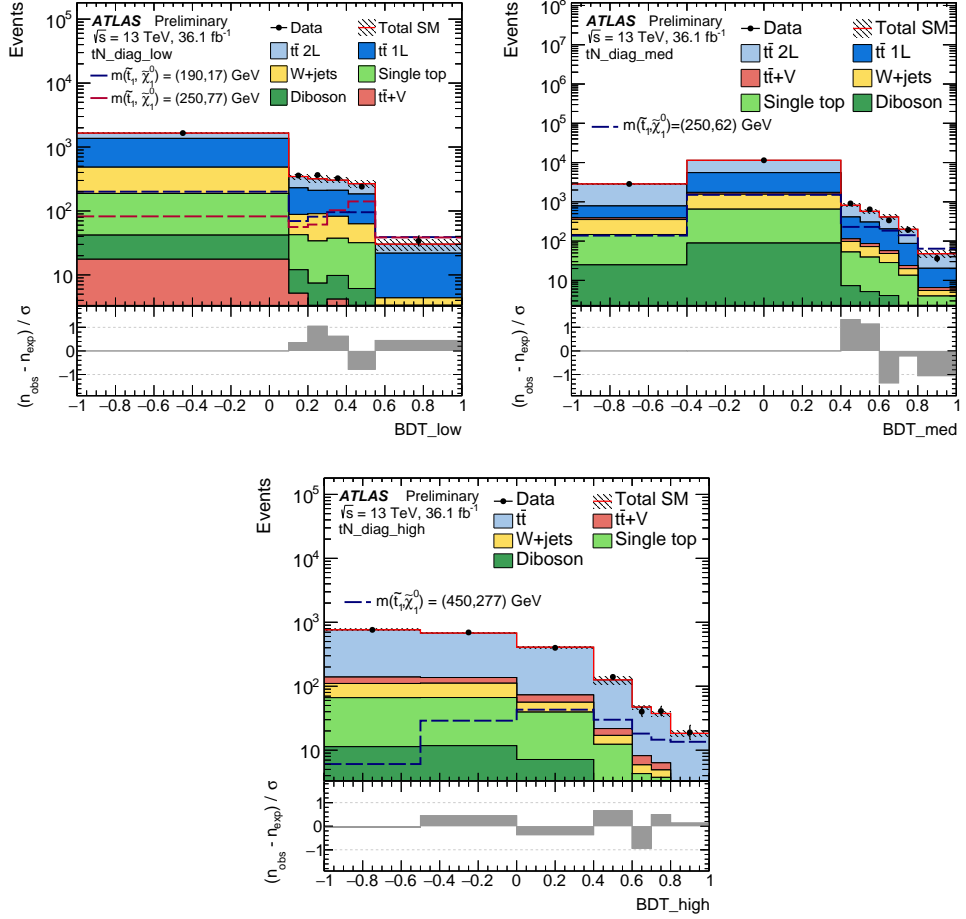


Figure 18: Distributions of BDT score for the $tN_{\text{diag_low}}$ (top left), $tN_{\text{diag_med}}$ (top right), and $tN_{\text{diag_high}}$ (bottom) regions. The SM background predictions are obtained using the background-only fit configuration, and the hashed area around the total SM background prediction includes all uncertainties. In addition to the background prediction, signal models are shown, denoted by $m(\tilde{t}_1, \tilde{\chi}_1^0)$. The bottom panels show the difference between data and the predicted SM background divided by the total uncertainty (σ_{tot}).

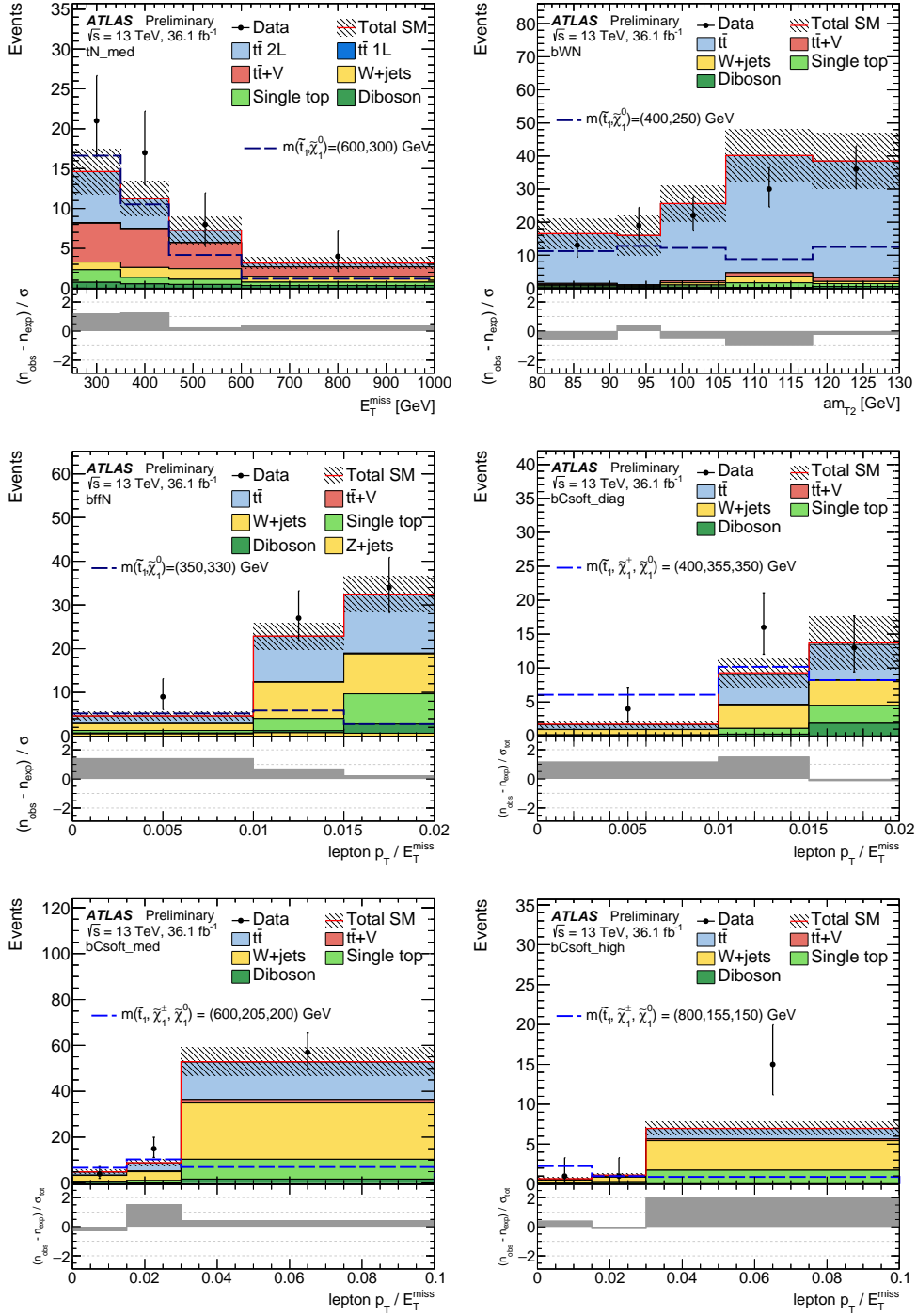


Figure 19: Kinematic distributions for the shape-fit analyses: (top left) E_T^{miss} in tN_{med} , (top right) am_{T2} in bWN , (middle left) $p_T^{\ell}/E_T^{\text{miss}}$ in $bffN$, (middle right) $p_T^{\ell}/E_T^{\text{miss}}$ in $bCsoft_{\text{diag}}$, (bottom left) $p_T^{\ell}/E_T^{\text{miss}}$ in $bCsoft_{\text{med}}$, and (bottom right) $p_T^{\ell}/E_T^{\text{miss}}$ in $bCsoft_{\text{high}}$. The full event selection in the corresponding signal region is applied, except for the requirement that is imposed on the variable being plotted. The predicted SM backgrounds are scaled with the normalisation factors obtained from the corresponding control regions in Tables 22 and 23. The hashed area around the total SM prediction includes statistical and experimental uncertainties. The last bin contains overflows. Benchmark signal models are overlaid for comparison. The bottom panels show the difference between data and the predicted SM background divided by the total uncertainty (σ_{tot}).

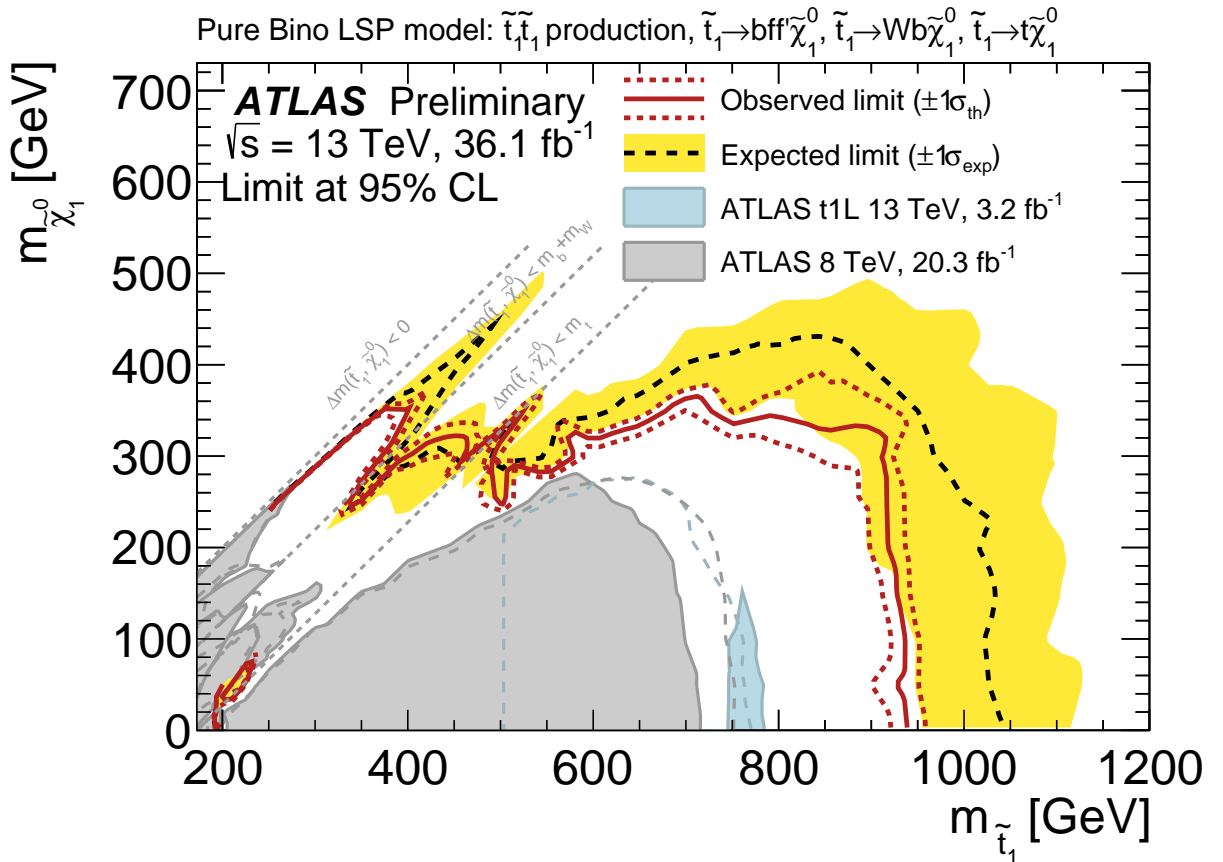


Figure 20: Expected (black dashed) and observed (red solid) 95% excluded regions in the plane of $m_{\tilde{t}_1}$ versus $m_{\tilde{\chi}_1^0}$ for the direct stop pair production assuming either $\tilde{t}_1 \rightarrow t\tilde{\chi}_1^0$, $\tilde{t}_1 \rightarrow bW\tilde{\chi}_1^0$, or $\tilde{t}_1 \rightarrow bff'\tilde{\chi}_1^0$ decay with a branching ratio of 100%. The excluded regions from previous publications [36, 38] are shown with the grey and blue shaded areas.

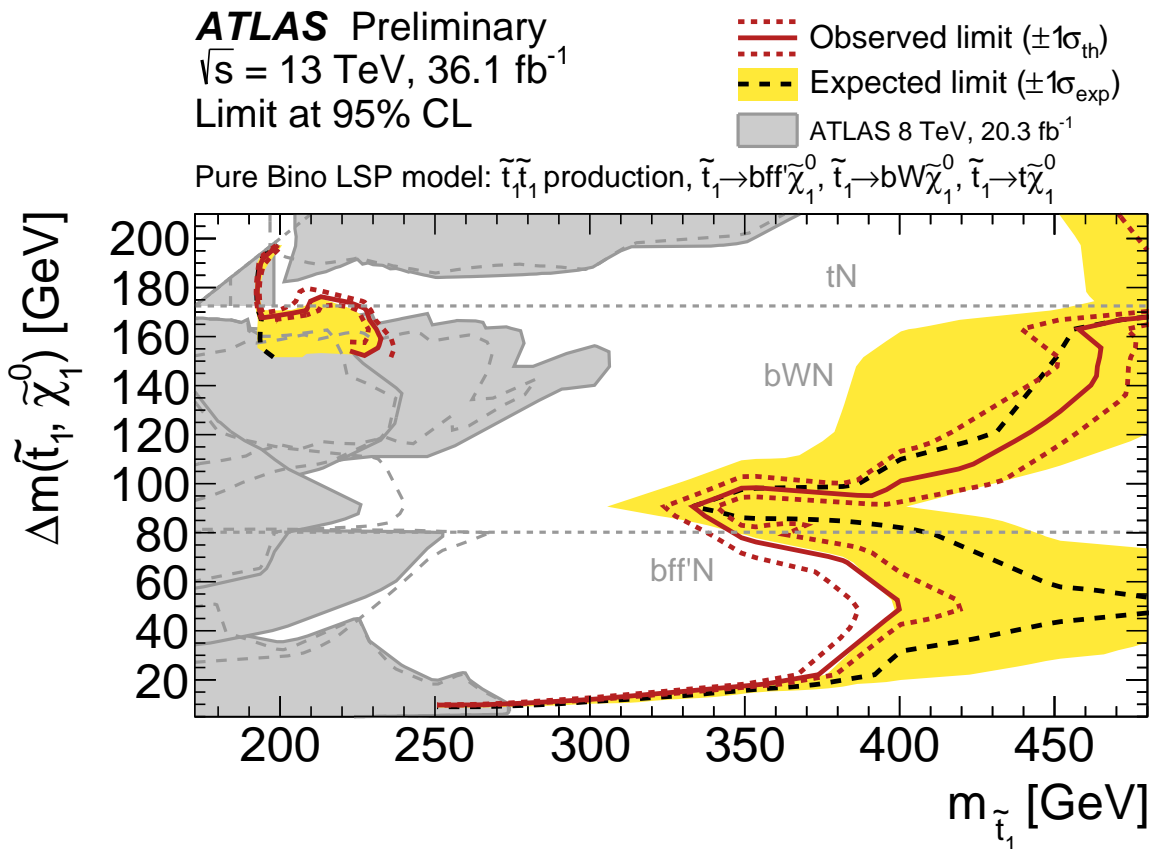


Figure 21: Expected (black dashed) and observed (red solid) 95% excluded regions in the plane of $m_{\tilde{t}_1}$ versus $\Delta m(\tilde{t}_1, \tilde{\chi}_1^0)$ for the direct stop pair production assuming either $\tilde{t}_1 \rightarrow t \tilde{\chi}_1^0$, $\tilde{t}_1 \rightarrow b W \tilde{\chi}_1^0$, or $\tilde{t}_1 \rightarrow b f f' \tilde{\chi}_1^0$ decay with a branching ratio of 100%. The excluded regions from previous publications [36, 38] are shown with the grey shaded area. In the region of phase-space above the line, only the $\tilde{t}_1 \rightarrow t \tilde{\chi}_1^0$ decay is allowed.

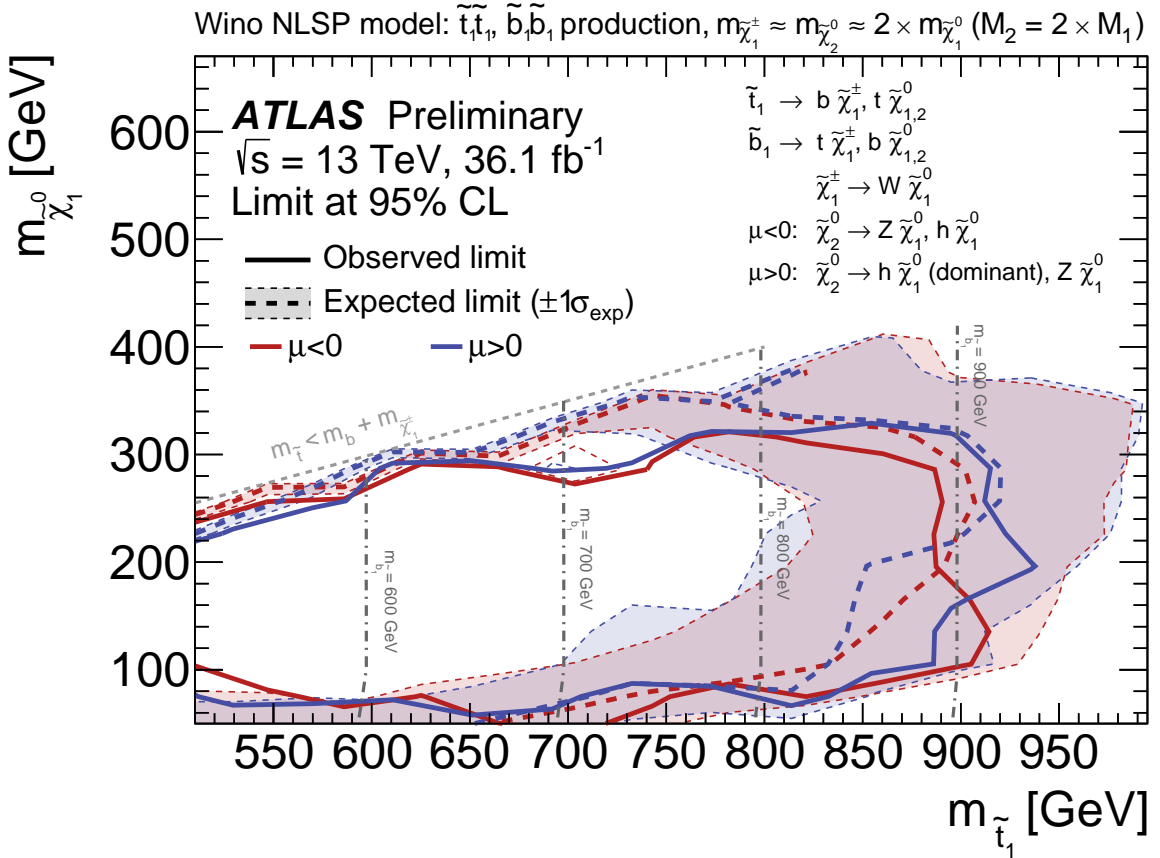


Figure 22: Expected (dashed) and observed (solid) 95% excluded regions in the plane of $m_{\tilde{t}_1}$ versus $m_{\tilde{\chi}_1^0}$ for the direct stop/sbottom pair production in the wino NLSP model under the hypothesis of $m_{q3L} < m_{tR}$, where various decay modes ($\tilde{t}_1 \rightarrow b \tilde{\chi}_1^\pm, \tilde{t}_1 \rightarrow t \tilde{\chi}_1^0, \tilde{t}_1 \rightarrow t \tilde{\chi}_2^0, \tilde{b}_1 \rightarrow t \tilde{\chi}_1^\pm, \tilde{b}_1 \rightarrow b \tilde{\chi}_1^0$, and $\tilde{b}_1 \rightarrow b \tilde{\chi}_2^0$) are considered with different branching ratios for each signal point. $\tilde{\chi}_2^0$ decays to $\tilde{\chi}_1^0$ predominantly via either Z boson or Higgs boson depending on the sign of the μ parameter. Contours for the $\mu > 0$ and $\mu < 0$ hypotheses are shown as blue and red lines, respectively. In this model, the $\tilde{\chi}_1^\pm$ and $\tilde{\chi}_2^0$ masses are assumed to be nearly twice as large as the LSP ($\tilde{\chi}_1^0$) mass. The grey vertical dash-dotted lines show the corresponding sbottom mass. The dashed line $m_{\tilde{t}_1} = m_b + m_{\tilde{\chi}_1^\pm}$ is a physical boundary of the $\tilde{t}_1 \rightarrow b \tilde{\chi}_1^\pm$ decay.

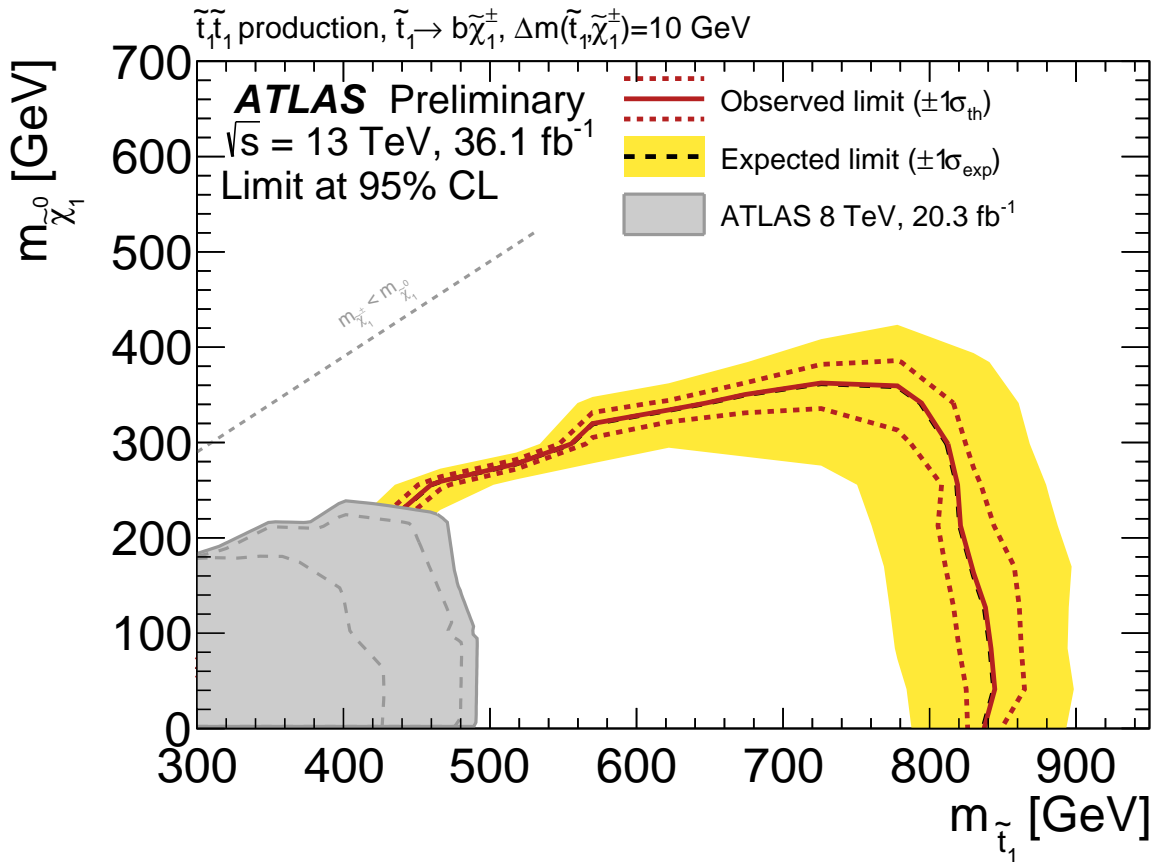


Figure 23: Expected (black dashed) and observed (red solid) 95% excluded regions in the plane of $m_{\tilde{t}_1}$ versus $m_{\tilde{\chi}_1^0}$ for direct stop pair production assuming $b\tilde{\chi}_1^\pm$ decay with a branching ratio of 100%. The chargino mass is assumed to be close to the stop mass, $m_{\tilde{\chi}_1^\pm} = m_{\tilde{t}_1} - 10$ GeV.

ATLAS Preliminary
 $\sqrt{s} = 13 \text{ TeV}, 36.1 \text{ fb}^{-1}$
 Limit at 95% CL

— Observed limit

— Expected limit ($\pm 1\sigma_{\text{exp}}$)

— $\tilde{t}_1 \approx \tilde{t}_L$ — $\tilde{t}_1 \approx \tilde{t}_L$ (large $\tan\beta$) — $\tilde{t}_1 \approx \tilde{t}_R$

Higgsino LSP model: $\tilde{t}_1 \tilde{t}_1$ production, $m_{\tilde{\chi}_1^\pm} = m_{\tilde{\chi}_1^0} + 5 \text{ GeV}$, $m_{\tilde{\chi}_2^0} = m_{\tilde{\chi}_1^0} + 10 \text{ GeV}$

$\tilde{t}_1 \rightarrow b \tilde{\chi}_1^\pm, t \tilde{\chi}_{1,2}^0$
 $\tilde{\chi}_1^\pm \rightarrow W \tilde{\chi}_1^0$ $\tilde{\chi}_2^0 \rightarrow h \tilde{\chi}_1^0, Z \tilde{\chi}_1^0$
 $\text{BR}(\tilde{t}_1^0, b\tilde{\chi}_1^\pm, t\tilde{\chi}_1^0) \approx$
 \tilde{t}_L , small $\tan\beta$: (45, 10, 45)%
 \tilde{t}_L , large $\tan\beta$: (33, 33, 33)%
 \tilde{t}_R : (25, 50, 25)%

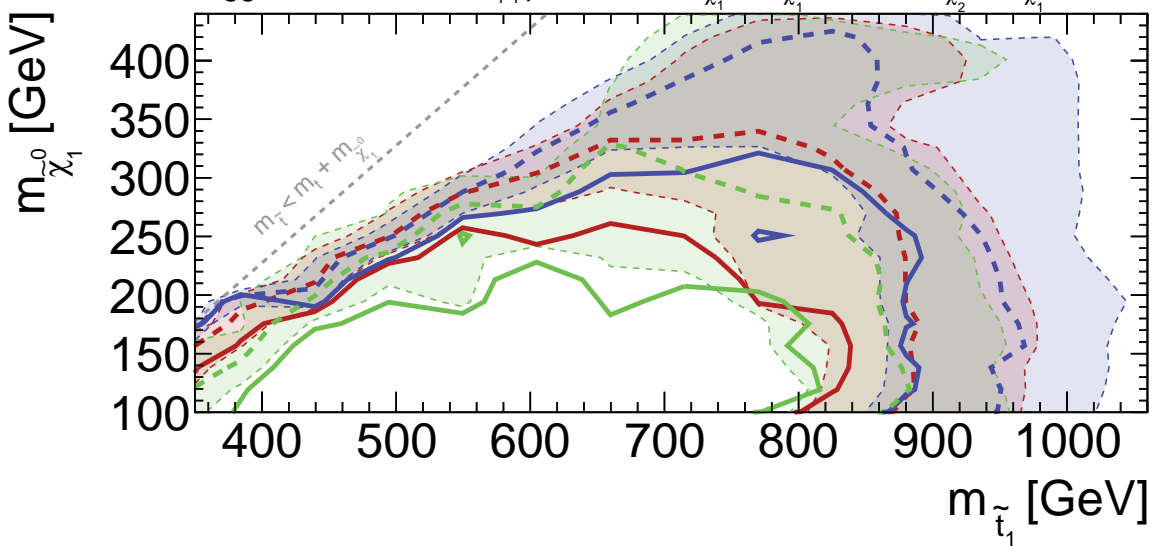


Figure 24: Expected (dashed) and observed (solid) 95% excluded regions in the plane of $m_{\tilde{t}_1}$ versus $m_{\tilde{\chi}_1^0}$ for direct stop pair production in the higgsino LSP model where various decay modes ($\tilde{t}_1 \rightarrow b\tilde{\chi}_1^\pm$, $\tilde{t}_1 \rightarrow t\tilde{\chi}_1^0$, $\tilde{t}_1 \rightarrow t\tilde{\chi}_2^0$) are considered with different branching ratios depending on the hypothesis being considered. In this model, $\Delta m(\tilde{\chi}_1^\pm, \tilde{\chi}_1^0) = 5 \text{ GeV}$ and $\Delta m(\tilde{\chi}_2^0, \tilde{\chi}_1^0) = 10 \text{ GeV}$ are assumed.

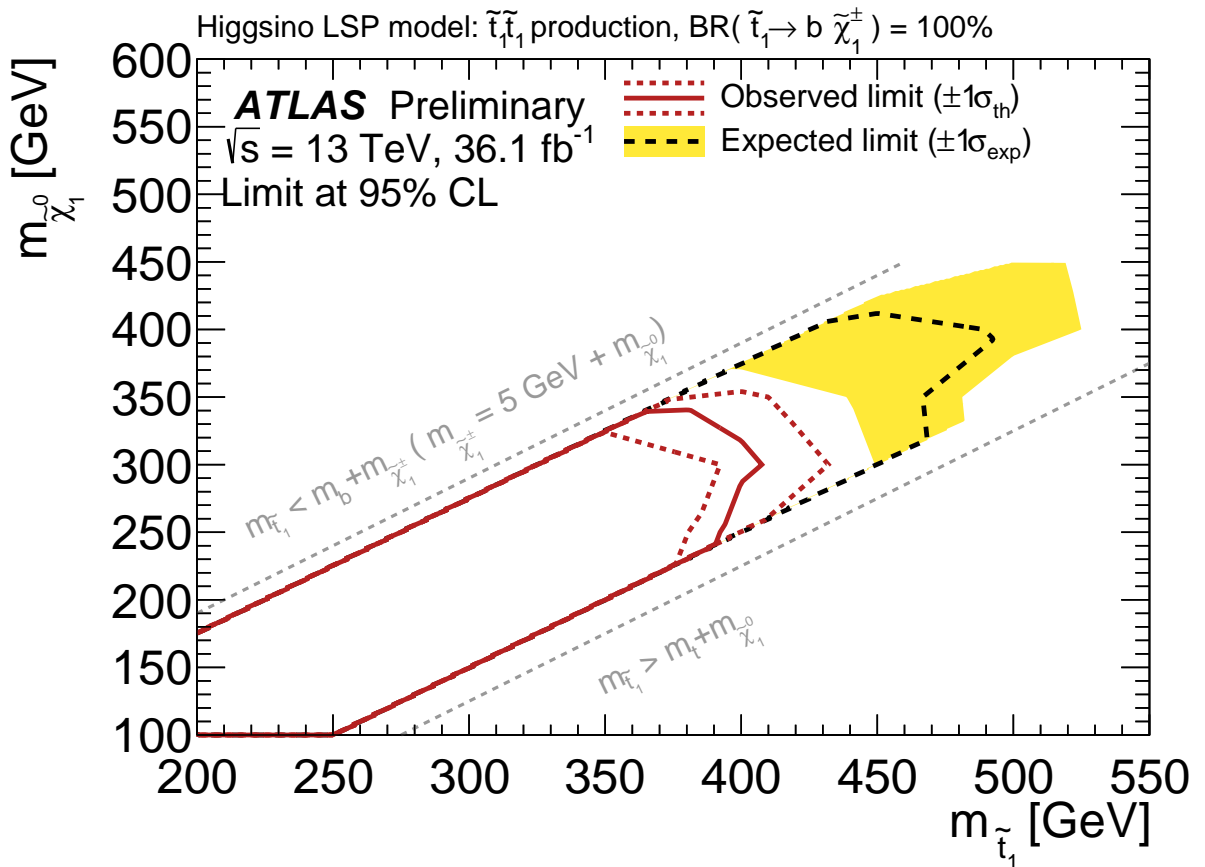


Figure 25: Expected (dashed) and observed (solid) 95% excluded regions in the plane of $m_{\tilde{t}_1}$ versus $m_{\tilde{\chi}_1^0}$ for direct stop pair production in the higgsino LSP model where only the $\tilde{t}_1 \rightarrow b \tilde{\chi}_1^\pm$ decay mode is kinematically allowed due to the phase-space constraint. In this model, $\Delta m(\tilde{\chi}_1^\pm, \tilde{\chi}_1^0) = 5 \text{ GeV}$ is assumed.

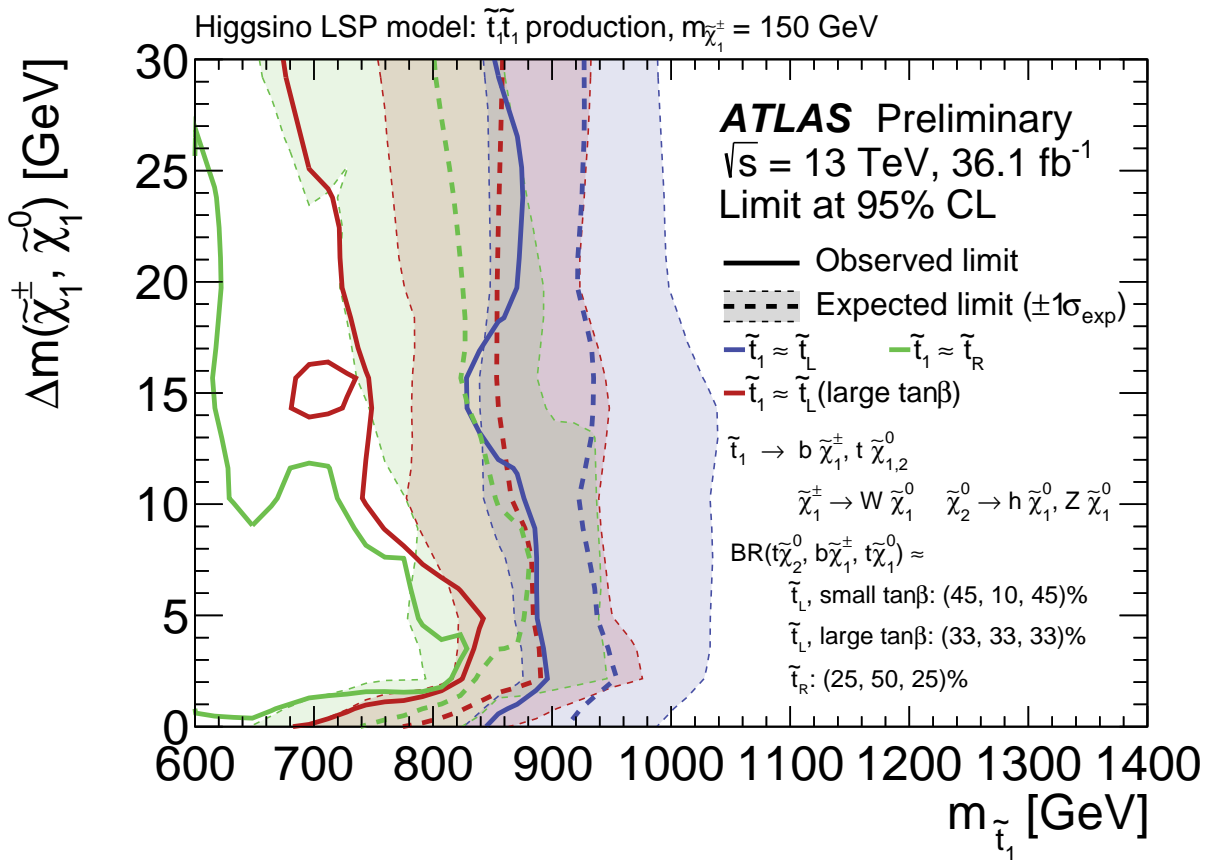


Figure 26: Expected (dashed) and observed (solid) 95% excluded regions in the plane of $m_{\tilde{t}_1}$ versus $\Delta m(\tilde{\chi}_1^\pm, \tilde{\chi}_1^0)$ for direct stop pair production in the fixed $m_{\tilde{\chi}_1^\pm} = 150$ GeV higgsino LSP model where various decay modes ($\tilde{t}_1 \rightarrow b\tilde{\chi}_1^\pm$, $\tilde{t}_1 \rightarrow t\tilde{\chi}_1^0$, $\tilde{t}_1 \rightarrow t\tilde{\chi}_2^0$) are considered with different branching ratio, depending on the hypothesis being considered, and overlaid. In this model, the mass relation of $\Delta m(\tilde{\chi}_2^0, \tilde{\chi}_1^0) = 2 \times \Delta m(\tilde{\chi}_1^\pm, \tilde{\chi}_1^0)$ is assumed, varying $\Delta m(\tilde{\chi}_1^\pm, \tilde{\chi}_1^0)$ from 0 GeV to 30 GeV. For the region below $\Delta m(\tilde{\chi}_1^\pm, \tilde{\chi}_1^0) = 2$ GeV, only the $\tilde{t}_1 \rightarrow t\tilde{\chi}_1^0$ decay is considered while the branching ratio is set, accounting for both $\tilde{t}_1 \rightarrow t\tilde{\chi}_1^0$ and $\tilde{t}_1 \rightarrow t\tilde{\chi}_2^0$ decays.

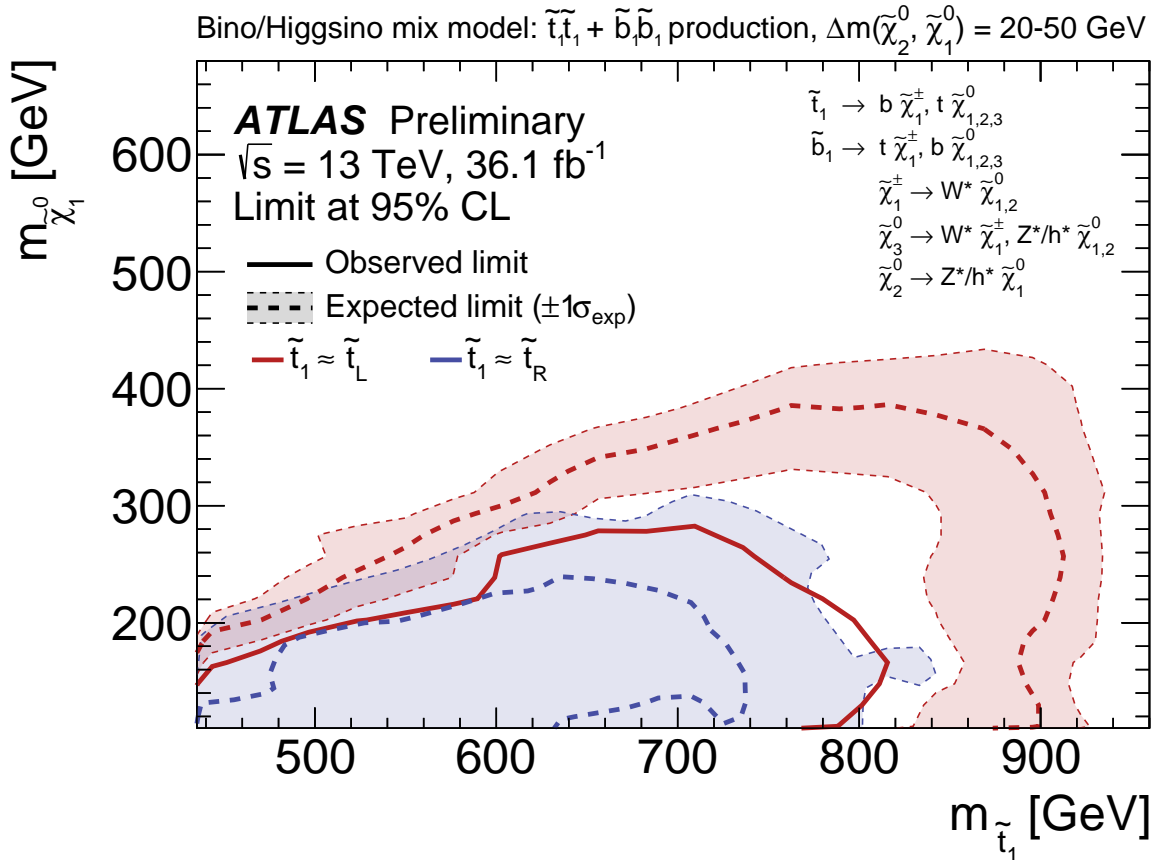


Figure 27: Expected (dashed) and observed (solid) 95% excluded regions in the plane of $m_{\tilde{t}_1}$ versus $m_{\tilde{\chi}_1^0}$ for the direct stop/sbottom pair production in the well-tempered neutralino model where various decay modes ($\tilde{t}_1 \rightarrow b\tilde{\chi}_1^\pm$, $\tilde{t}_1 \rightarrow t\tilde{\chi}_1^0$, $\tilde{t}_1 \rightarrow t\tilde{\chi}_2^0$, $\tilde{b}_1 \rightarrow t\tilde{\chi}_1^\pm$, $\tilde{b}_1 \rightarrow b\tilde{\chi}_1^0$, and $\tilde{b}_1 \rightarrow b\tilde{\chi}_2^0$) are considered with different branching ratio for each signal point. Contours for the $m_{q3L} < m_{tR}$ and $m_{q3L} > m_{tR}$ hypotheses are shown separately as red and blue lines, respectively. For $m_{q3L} < m_{tR}$ hypothesis, both stop/sbottom pair productions are considered while for $m_{q3L} > m_{tR}$ hypothesis, only stop pair production is considered.

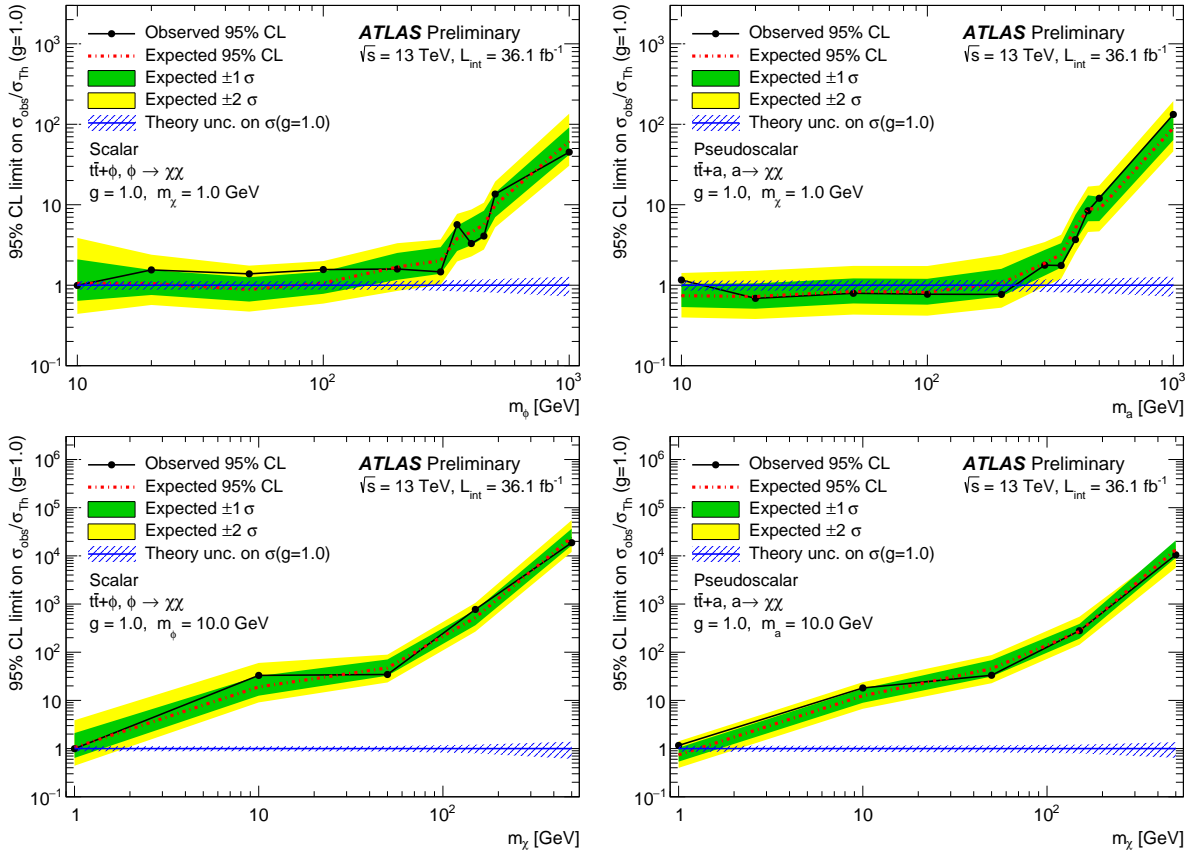


Figure 28: Upper limit on the ratio of the DM production cross-section to the simplified model expectation under the hypothesis of (left) a scalar or (right) a pseudoscalar mediator. The limit is shown as a function of: (top) the mediator mass for a fixed mass of the DM candidate of 1 GeV, or (bottom) the DM candidate mass for a fixed mediator mass of 10 GeV. The coupling of the mediator to SM and DM particles is assumed to be $g = 1$.

11 Summary and conclusions

This note presents searches for direct top squark pair production covering various SUSY scenarios and for a spin-0 mediator decaying into pair-produced dark matter particles in association with $t\bar{t}$ using the final state with one isolated lepton, jets, and E_T^{miss} . Thirteen signal-region selections are optimised for the discovery of the top-squark signature. The analysis also defines three signal-region selections for the spin-0 mediator models.

The search uses 36.1 fb^{-1} of pp collision data collected by the ATLAS experiment at a centre-of-mass energy of $\sqrt{s} = 13 \text{ TeV}$. No significant excess is observed over the estimated Standard Model backgrounds. Exclusion limits at 95% confidence level are derived for the models considered.

For the direct top squark pair production models the results extend previous exclusion limits by excluding the top-squark mass region up to 940 GeV for a massless lightest neutralino under the assumption of $\text{BR}(\tilde{t}_1 \rightarrow t\tilde{\chi}_1^0) = 100\%$. Exclusion limits are also extended in pMSSM models targeting various sparticle mass spectra. For the wino NLSP model, the top-squark mass region up to 885 GeV (940 GeV) is excluded in scenarios with $\mu < 0$ ($\mu > 0$) and a 200 GeV neutralino. For the higgsino LSP model, the top-squark mass region up to 860 GeV (800 GeV) is excluded in scenarios with $m_{q3L} < m_{tR}$ ($m_{tR} < m_{q3L}$). Furthermore, in a model with well-tempered neutralinos, the top-squark mass region up to 810 GeV is excluded in scenarios with $m_{q3L} < m_{tR}$ while no observed limit is set in scenarios with $m_{tR} > m_{q3L}$.

For the spin-0 mediator models, a scalar (pseudo-scalar) mediator mass of up to 65 GeV (220 GeV) is excluded at 95% confidence level, assuming a 1 GeV dark matter particle mass and a common coupling to SM and dark matter particles of $g = 1$.

Appendix

A Appendix

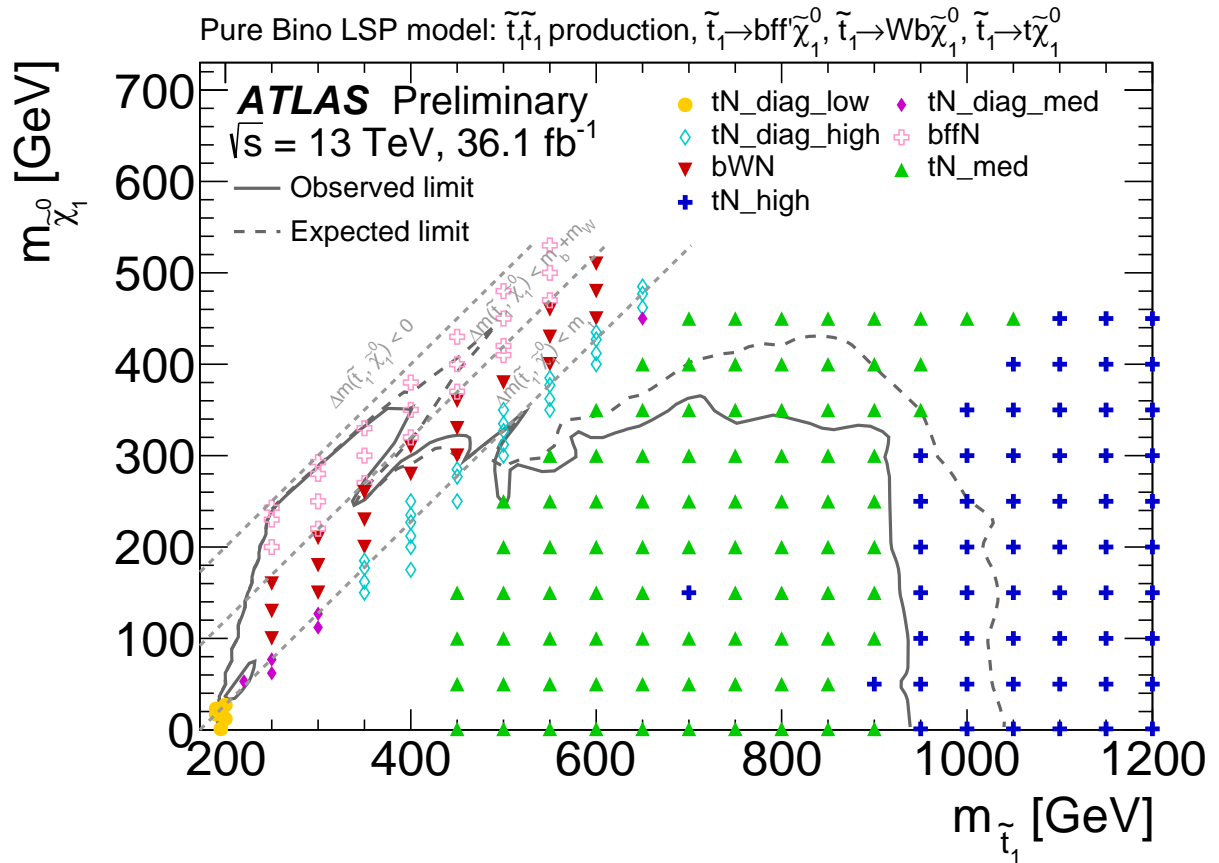


Figure 29: Selected (best-expected) signal regions for each grid point in the pure bino LSP scenario.

References

- [1] S. Weinberg, *Implications of Dynamical Symmetry Breaking*, *Phys. Rev. D* **13** (1976) 974.
- [2] E. Gildener, *Gauge Symmetry Hierarchies*, *Phys. Rev. D* **14** (1976) 1667.
- [3] S. Weinberg, *Implications of Dynamical Symmetry Breaking: An Addendum*, *Phys. Rev. D* **19** (1979) 1277.
- [4] L. Susskind, *Dynamics of Spontaneous Symmetry Breaking in the Weinberg-Salam Theory*, *Phys. Rev. D* **20** (1979) 2619.
- [5] *Observation of a new particle in the search for the Standard Model Higgs boson with the ATLAS detector at the LHC*, *Phys. Lett. B* **716** (2012) 1, arXiv: [1207.7214 \[hep-ex\]](https://arxiv.org/abs/1207.7214).
- [6] *Observation of a new boson at a mass of 125 GeV with the CMS experiment at the LHC*, *Phys. Lett. B* **716** (2012) 30, arXiv: [1207.7235 \[hep-ex\]](https://arxiv.org/abs/1207.7235).
- [7] L. Evans and P. Bryant, *LHC Machine*, *JINST* **3** (2008) S08001.
- [8] H. Miyazawa, *Baryon Number Changing Currents*, *Prog. Theor. Phys.* **36** (6) (1966) 1266.
- [9] R. Ramond, *Dual Theory for Free Fermions*, *Phys. Rev. D* **3** (1971) 2415.
- [10] Yu. A. Gol'fand and E. P. Likhtman, *Extension of the Algebra of Poincare Group Generators and Violation of p Invariance*, *JETP Lett.* **13** (1971) 323, [*Pisma Zh. Eksp. Teor. Fiz.* 13, 452 (1971)].
- [11] A. Neveu and J. Schwarz, *Factorizable dual model of pions*, *Nucl. Phys. B* **31** (1971) 86.
- [12] A. Neveu and J. Schwarz, *Quark Model of Dual Pions*, *Phys. Rev. D* **4** (1971) 1109.
- [13] J. Gervais and B. Sakita, *Field theory interpretation of supergauges in dual models*, *Nucl. Phys. B* **34** (1971) 632.
- [14] D. V. Volkov and V. P. Akulov, *Is the Neutrino a Goldstone Particle?*, *Phys. Lett. B* **46** (1973) 109.
- [15] J. Wess and B. Zumino, *A Lagrangian Model Invariant Under Supergauge Transformations*, *Phys. Lett. B* **49** (1974) 52.
- [16] J. Wess and B. Zumino, *Supergauge Transformations in Four-Dimensions*, *Nucl. Phys. B* **70** (1974) 39.
- [17] S. Dimopoulos and H. Georgi, *Softly Broken Supersymmetry and $SU(5)$* , *Nucl. Phys. B* **193** (1981) 150.
- [18] E. Witten, *Dynamical Breaking of Supersymmetry*, *Nucl. Phys. B* **188** (1981) 513.
- [19] M. Dine, W. Fischler and M. Srednicki, *Supersymmetric Technicolor*, *Nucl. Phys. B* **189** (1981) 575.
- [20] S. Dimopoulos and S. Raby, *Supercolor*, *Nucl. Phys. B* **192** (1981) 353.
- [21] N. Sakai, *Naturalness in Supersymmetric Guts*, *Zeit. Phys. C* **11** (1981) 153.
- [22] R. Kaul and P. Majumdar, *Cancellation of Quadratically Divergent Mass Corrections in Globally Supersymmetric Spontaneously Broken Gauge Theories*, *Nucl. Phys. B* **199** (1982) 36.
- [23] R. Barbieri and G. F. Giudice, *Upper Bounds on Supersymmetric Particle Masses*, *Nucl. Phys. B* **306** (1988) 63.

- [24] B. de Carlos and J. A. Casas, *One loop analysis of the electroweak breaking in supersymmetric models and the fine tuning problem*, *Phys. Lett. B* **309** (1993) 320, arXiv: [hep-ph/9303291 \[hep-ph\]](#).
- [25] K. Inoue, A. Kakuto, H. Komatsu and S. Takeshita, *Aspects of Grand Unified Models with Softly Broken Supersymmetry*, *Prog. Theor. Phys.* **68** (1982) 927, [Erratum: *Prog. Theor. Phys.* 70,330(1983)].
- [26] J. R. Ellis and S. Rudaz, *Search for Supersymmetry in Toponium Decays*, *Phys. Lett. B* **128** (1983) 248.
- [27] C. Regis et al., *Search for Proton Decay via $p \rightarrow \mu^+ K^0$ in Super-Kamiokande I, II, and III*, *Phys. Rev. D* **86** (2012) 012006, arXiv: [1205.6538 \[hep-ex\]](#).
- [28] P. Fayet, *Supersymmetry and Weak, Electromagnetic and Strong Interactions*, *Phys. Lett. B* **64** (1976) 159.
- [29] P. Fayet, *Spontaneously Broken Supersymmetric Theories of Weak, Electromagnetic and Strong Interactions*, *Phys. Lett. B* **69** (1977) 489.
- [30] G. R. Farrar and P. Fayet, *Phenomenology of the Production, Decay, and Detection of New Hadronic States Associated with Supersymmetry*, *Phys. Lett. B* **76** (1978) 575.
- [31] P. Fayet, *Relations Between the Masses of the Superpartners of Leptons and Quarks, the Goldstino Couplings and the Neutral Currents*, *Phys. Lett. B* **84** (1979) 416.
- [32] H. Goldberg, *Constraint on the Photino Mass from Cosmology*, *Phys. Rev. Lett.* **50** (1983) 1419, [Erratum: *Phys. Rev. Lett.* 103,099905(2009)].
- [33] J. R. Ellis, J. S. Hagelin, D. V. Nanopoulos, K. A. Olive and M. Srednicki, *Supersymmetric Relics from the Big Bang*, *Nucl. Phys. B* **238** (1984) 453.
- [34] ATLAS Collaboration, *Search for direct third-generation squark pair production in final states with missing transverse momentum and two b -jets in $\sqrt{s} = 8$ TeV pp collisions with the ATLAS detector*, *JHEP* **10** (2013) 189, arXiv: [1308.2631 \[hep-ex\]](#).
- [35] ATLAS Collaboration, *Search for direct top-squark pair production in final states with two leptons in pp collisions at $\sqrt{s} = 8$ TeV with the ATLAS detector*, *JHEP* **06** (2014) 124, arXiv: [1403.4853 \[hep-ex\]](#).
- [36] ATLAS Collaboration, *Search for top squark pair production in final states with one isolated lepton, jets, and missing transverse momentum in $\sqrt{s} = 8$ TeV pp collisions with the ATLAS detector*, *JHEP* **11** (2014) 118, arXiv: [1407.0583 \[hep-ex\]](#).
- [37] ATLAS Collaboration, *ATLAS Run 1 searches for direct pair production of third-generation squarks at the Large Hadron Collider*, *Eur. Phys. J. C* **75** (2015) 510, arXiv: [1506.08616 \[hep-ex\]](#).
- [38] ATLAS Collaboration, *Search for top squarks in final states with one isolated lepton, jets, and missing transverse momentum in $\sqrt{s} = 13$ TeV pp collisions with the ATLAS detector*, *Phys. Rev. D* **94** (2016) 052009, arXiv: [1606.03903 \[hep-ex\]](#).
- [39] CMS Collaboration, *Inclusive search for supersymmetry using razor variables in pp collisions at $\sqrt{s} = 7$ TeV*, *Phys. Rev. Lett.* **111** (2013) 081802, arXiv: [1212.6961 \[hep-ex\]](#).

[40] CMS Collaboration, *Search for supersymmetry in hadronic final states with missing transverse energy using the variables α_T and b-quark multiplicity in pp collisions at $\sqrt{s} = 8$ TeV*, *Eur. Phys. J. C* **73** (2013) 2568, arXiv: [1303.2985 \[hep-ex\]](#).

[41] CMS Collaboration, *Search for top-squark pair production in the single-lepton final state in pp collisions at $\sqrt{s} = 8$ TeV*, *Eur. Phys. J. C* **73** (2013) 2677, arXiv: [1308.1586 \[hep-ex\]](#).

[42] CMS Collaboration, *Search for top squark and higgsino production using diphoton Higgs boson decays*, *Phys. Rev. Lett.* **112** (2014) 161802, arXiv: [1312.3310 \[hep-ex\]](#).

[43] CMS Collaboration, *Search for top-squark pairs decaying into Higgs or Z bosons in pp collisions at $\sqrt{s} = 8$ TeV*, *Phys. Lett. B* **736** (2014) 371, arXiv: [1405.3886 \[hep-ex\]](#).

[44] CMS Collaboration, *Searches for pair production for third-generation squarks in $\sqrt{s} = 13$ TeV pp collisions*, *EPJC* (2016), arXiv: [1612.03877 \[hep-ex\]](#).

[45] T. Aaltonen et al., *Search for Pair Production of Supersymmetric Top Quarks in Dilepton Events from p anti-p Collisions at $\sqrt{s} = 1.96$ TeV*, *Phys. Rev. Lett.* **104** (2010) 251801, arXiv: [0912.1308 \[hep-ex\]](#).

[46] V. Abazov et al., *Search for the lightest scalar top quark in events with two leptons in p \bar{p} collisions at $\sqrt{s} = 1.96$ TeV*, *Phys. Lett. B* **675** (2009) 289, arXiv: [0811.0459 \[hep-ex\]](#).

[47] LEP SUSY Working Group, ALEPH, DELPHI, L3 and OPAL experiments, [LEPSUSYWG/04-02.1](#).

[48] J. Alwall, M.-P. Le, M. Lisanti and J. G. Wacker, *Searching for Directly Decaying Gluinos at the Tevatron*, *Phys. Lett. B* **666** (2008) 34, arXiv: [0803.0019 \[hep-ph\]](#).

[49] J. Alwall, P. Schuster and N. Toro, *Simplified Models for a First Characterization of New Physics at the LHC*, *Phys. Rev. D* **79** (2009) 075020, arXiv: [0810.3921 \[hep-ph\]](#).

[50] D. Alves, *Simplified Models for LHC New Physics Searches*, *J. Phys. G* **39** (2012) 105005, ed. by N. Arkani-Hamed et al., arXiv: [1105.2838 \[hep-ph\]](#).

[51] A. Djouadi et al., ‘The Minimal supersymmetric standard model: Group summary report’, *GDR (Groupement De Recherche) - Supersymetrie Montpellier, France, April 15-17, 1998*, 1998, arXiv: [hep-ph/9901246 \[hep-ph\]](#), URL: inspirehep.net/record/481987/files/arXiv:hep-ph_9901246.pdf.

[52] C. F. Berger, J. S. Gainer, J. L. Hewett and T. G. Rizzo, *Supersymmetry Without Prejudice*, *JHEP* **0902** (2009) 023, arXiv: [0812.0980 \[hep-ph\]](#).

[53] ATLAS Collaboration, *A Particle Consistent with the Higgs Boson Observed with the ATLAS Detector at the Large Hadron Collider*, *Science* **338** (2012) 1576.

[54] CMS Collaboration, *Observation of a new boson at a mass of 125 GeV with the CMS experiment at the LHC*, *Phys. Lett. B* **716** (2012) 30, arXiv: [1207.7235 \[hep-ex\]](#).

[55] ATLAS Collaboration, *Search for charginos nearly mass degenerate with the lightest neutralino based on a disappearing-track signature in pp collisions at $\sqrt{s} = 8$ TeV with the ATLAS detector*, *Phys. Rev. D* **88** (2013) 112006, arXiv: [1310.3675 \[hep-ex\]](#).

[56] G. F. Giudice, M. A. Luty, H. Murayama and R. Rattazzi, *Gaugino mass without singlets*, *JHEP* **9812** (1998) 027, arXiv: [hep-ph/9810442 \[hep-ph\]](#).

[57] L. Randall and R. Sundrum, *Out of this world supersymmetry breaking*, *Nucl. Phys. B* **557** (1999) 79, arXiv: [hep-th/9810155 \[hep-th\]](#).

[58] M. Dine and W. Fischler, *A Phenomenological Model of Particle Physics Based on Supersymmetry*, *Phys. Lett. B* **110** (1982) 227.

[59] L. Alvarez-Gaume, M. Claudson and M. B. Wise, *Low-Energy Supersymmetry*, *Nucl. Phys. B* **207** (1982) 96.

[60] C. R. Nappi and B. A. Ovrut, *Supersymmetric Extension of the $SU(3) \times SU(2) \times U(1)$ Model*, *Phys. Lett. B* **113** (1982) 175.

[61] A. H. Chamseddine, R. L. Arnowitt and P. Nath, *Locally Supersymmetric Grand Unification*, *Phys. Rev. Lett.* **49** (1982) 970.

[62] R. Barbieri, S. Ferrara and C. A. Savoy, *Gauge Models with Spontaneously Broken Local Supersymmetry*, *Phys. Lett. B* **119** (1982) 343.

[63] G. L. Kane, C. F. Kolda, L. Roszkowski and J. D. Wells, *Study of constrained minimal supersymmetry*, *Phys. Rev. D* **49** (1994) 6173, arXiv: [hep-ph/9312272 \[hep-ph\]](#).

[64] LEP SUSY Working Group, ALEPH, DELPHI, L3 and OPAL experiments, *LEPSUSYWG/01-03.1*.

[65] Michele Papucci, Joshua T. Ruderman, Andreas Weiler, *Natural SUSY Endures*, *JHEP* **09** (2012), arXiv: [1110.6926 \[hep-ex\]](#).

[66] N. Arkani-Hamed, A. Delgado and G. F. Giudice, *The Well-tempered neutralino*, *Nucl. Phys. B* **741** (2006) 108, arXiv: [hep-ph/0601041 \[hep-ph\]](#).

[67] R. Barbieri and G. Giudice, *Upper bounds on supersymmetric particle masses*, *Nucl. Phys. B* **306** (1988) 063.

[68] ATLAS Collaboration, *Summary of the ATLAS experiment's sensitivity to supersymmetry after LHC Run 1 — interpreted in the phenomenological MSSM*, *JHEP* **10** (2015) 134, arXiv: [1508.06608 \[hep-ex\]](#).

[69] Plank Collaboration, () .

[70] ATLAS Collaboration, *The ATLAS Experiment at the CERN Large Hadron Collider*, *JINST* **3** (2008) S08003.

[71] ATLAS Collaboration, *Optimisation of the ATLAS b-tagging performance for the 2016 LHC Run*, ATL-PHYS-PUB-2016-012, 2016, URL: <https://cds.cern.ch/record/2160731>.

[72] M. Aaboud et al., *Performance of the ATLAS Trigger System in 2015*, (2016), arXiv: [1611.09661 \[hep-ex\]](#).

[73] ATLAS Collaboration, *Improved luminosity determination in pp collisions at $\sqrt{s} = 7$ TeV using the ATLAS detector at the LHC*, *Eur. Phys. J. C* **73** (2013) 2518, arXiv: [1302.4393 \[hep-ex\]](#).

[74] S. Alioli, P. Nason, C. Oleari and E. Re, *A general framework for implementing NLO calculations in shower Monte Carlo programs: the POWHEG BOX*, *JHEP* **1006** (2010) 043, arXiv: [1002.2581 \[hep-ph\]](#).

[75] H.-L. Lai et al., *New parton distributions for collider physics*, *Phys. Rev. D* **82** (2010) 074024, arXiv: [1007.2241 \[hep-ph\]](#).

[76] T. Sjöstrand, S. Mrenna and P. Z. Skands, *PYTHIA 6.4 Physics and Manual*, *JHEP* **0605** (2006) 026, arXiv: [hep-ph/0603175](#).

[77] P. Z. Skands, *Tuning Monte Carlo Generators: The Perugia Tunes*, *Phys. Rev. D* **82** (2010) 074018, arXiv: [1005.3457 \[hep-ph\]](#).

[78] M. Czakon, P. Fiedler and A. Mitov, *Total Top-Quark Pair-Production Cross Section at Hadron Colliders Through $O(\alpha_S^4)$* , *Phys. Rev. Lett.* **110** (2013) 252004, arXiv: [1303.6254 \[hep-ph\]](#).

[79] M. Czakon and A. Mitov, *NNLO corrections to top pair production at hadron colliders: the quark-gluon reaction*, *JHEP* **1301** (2013) 080, arXiv: [1210.6832 \[hep-ph\]](#).

[80] M. Czakon and A. Mitov, *NNLO corrections to top-pair production at hadron colliders: the all-fermionic scattering channels*, *JHEP* **1212** (2012) 054, arXiv: [1207.0236 \[hep-ph\]](#).

[81] P. Bärnreuther, M. Czakon and A. Mitov, *Percent Level Precision Physics at the Tevatron: First Genuine NNLO QCD Corrections to $q\bar{q} \rightarrow t\bar{t} + X$* , *Phys. Rev. Lett.* **109** (2012) 132001, arXiv: [1204.5201 \[hep-ph\]](#).

[82] M. Cacciari, M. Czakon, M. Mangano, A. Mitov and P. Nason, *Top-pair production at hadron colliders with next-to-next-to-leading logarithmic soft-gluon resummation*, *Phys. Lett. B* **710** (2012) 612, arXiv: [1111.5869 \[hep-ph\]](#).

[83] M. Czakon and A. Mitov, *Top++: A Program for the Calculation of the Top-Pair Cross-Section at Hadron Colliders*, *Comput. Phys. Commun.* **185** (2014) 2930, arXiv: [1112.5675 \[hep-ph\]](#).

[84] N. Kidonakis, *Next-to-next-to-leading-order collinear and soft gluon corrections for t-channel single top quark production*, *Phys. Rev. D* **83** (2011) 091503, arXiv: [1103.2792 \[hep-ph\]](#).

[85] N. Kidonakis, *Two-loop soft anomalous dimensions for single top quark associated production with a W- or H-*, *Phys. Rev. D* **82** (2010) 054018, arXiv: [1005.4451 \[hep-ph\]](#).

[86] N. Kidonakis, *NNLL resummation for s-channel single top quark production*, *Phys. Rev. D* **81** (2010) 054028, arXiv: [1001.5034 \[hep-ph\]](#).

[87] T. Gleisberg, S. Höche, F. Krauss, M. Schönherr, S. Schumann et al., *Event generation with SHERPA 1.1*, *JHEP* **0902** (2009) 007, arXiv: [0811.4622 \[hep-ph\]](#).

[88] R. D. Ball et al., *Parton distributions for the LHC Run II*, *JHEP* **1504** (2015) 040, arXiv: [1410.8849 \[hep-ph\]](#).

[89] S. Catani, L. Cieri, G. Ferrera, D. de Florian and M. Grazzini, *Vector boson production at hadron colliders: a fully exclusive QCD calculation at NNLO*, *Phys. Rev. Lett.* **103** (2009) 082001, arXiv: [0903.2120 \[hep-ph\]](#).

[90] J. Alwall et al., *The automated computation of tree-level and next-to-leading order differential cross sections, and their matching to parton shower simulations*, *JHEP* **1407** (2014) 079, arXiv: [1405.0301 \[hep-ph\]](#).

[91] T. Sjöstrand, S. Mrenna and P. Z. Skands, *A Brief Introduction to PYTHIA 8.1*, *Comput. Phys. Commun.* **178** (2008) 852, arXiv: [0710.3820 \[hep-ph\]](#).

[92] ATLAS Collaboration, *ATLAS Pythia 8 tunes to 7 TeV data*, ATL-PHYS-PUB-2014-021, 2014, URL: <https://cds.cern.ch/record/1966419>.

[93] R. D. Ball et al., *Parton distributions with LHC data*, *Nucl. Phys. B* **867** (2013) 244, arXiv: [1207.1303 \[hep-ph\]](https://arxiv.org/abs/1207.1303).

[94] C. Borschensky et al.,
Squark and gluino production cross sections in pp collisions at $\sqrt{s} = 13, 14, 33$ and 100 TeV, *Eur. Phys. J. C* **74** (2014) 3174, arXiv: [1407.5066 \[hep-ph\]](https://arxiv.org/abs/1407.5066).

[95] E. Re,
Single-top Wt-channel production matched with parton showers using the POWHEG method, *Eur. Phys. J. C* **71** (2011) 1547, arXiv: [1009.2450 \[hep-ph\]](https://arxiv.org/abs/1009.2450).

[96] S. Frixione, P. Nason and G. Ridolfi,
A Positive-weight next-to-leading-order Monte Carlo for heavy flavour hadroproduction, *JHEP* **0709** (2007) 126, arXiv: [0707.3088 \[hep-ph\]](https://arxiv.org/abs/0707.3088).

[97] R. Frederix, E. Re and P. Torrielli, *Single-top t-channel hadroproduction in the four-flavour scheme with POWHEG and aMC@NLO*, *JHEP* **1209** (2012) 130, arXiv: [1207.5391 \[hep-ph\]](https://arxiv.org/abs/1207.5391).

[98] S. Alioli, P. Nason, C. Oleari and E. Re,
NLO single-top production matched with shower in POWHEG: s- and t-channel contributions, *JHEP* **0909** (2009) 111, [Erratum: *JHEP* 02,011(2010)], arXiv: [0907.4076 \[hep-ph\]](https://arxiv.org/abs/0907.4076).

[99] D. J. Lange, *The EvtGen particle decay simulation package*, *Nucl. Instrum. Meth. A* **462** (2001) 152.

[100] ATLAS Collaboration, *The ATLAS Simulation Infrastructure*, *Eur. Phys. J. C* **70** (2010) 823, arXiv: [1005.4568 \[hep-ex\]](https://arxiv.org/abs/1005.4568).

[101] ‘Simulation of top quark production for the ATLAS experiment at $\sqrt{s} = 13$ TeV’, tech. rep. ATL-PHYS-PUB-2016-004, CERN, 2016, URL: <https://cds.cern.ch/record/2120417>.

[102] S. Frixione, E. Laenen, P. Motylinski, B. R. Webber and C. D. White,
Single-top hadroproduction in association with a W boson, *JHEP* **0807** (2008) 029, arXiv: [0805.3067 \[hep-ph\]](https://arxiv.org/abs/0805.3067).

[103] M. Bahr et al., *Herwig++ Physics and Manual*, *Eur. Phys. J. C* **58** (2008) 639, arXiv: [0803.0883 \[hep-ph\]](https://arxiv.org/abs/0803.0883).

[104] J. Bellm et al., *Herwig 7.0/Herwig++ 3.0 release note*, *Eur. Phys. J. C* **76** (2016) 196, arXiv: [1512.01178 \[hep-ph\]](https://arxiv.org/abs/1512.01178).

[105] B. Allanach, *SOFTSUSY: a program for calculating supersymmetric spectra*, *Comput. Phys. Commun.* **143** (2002) 305, arXiv: [hep-ph/0104145 \[hep-ph\]](https://arxiv.org/abs/hep-ph/0104145).

[106] B. Allanach, P. Athron, L. C. Tunstall, A. Voigt and A. Williams, *Next-to-Minimal SOFTSUSY*, *Comput. Phys. Commun.* **185** (2014) 2322, arXiv: [1311.7659 \[hep-ph\]](https://arxiv.org/abs/1311.7659).

[107] A. Djouadi, J. Kalinowski and M. Spira, *HDECAY: A Program for Higgs boson decays in the standard model and its supersymmetric extension*, *Comput. Phys. Commun.* **108** (1998) 56–74, arXiv: [9704448 \[hep-ph\]](https://arxiv.org/abs/9704448).

[108] A. Djouadi, M. Muhlleitner and M. Spira, *Decays of supersymmetric particles: The Program SUSY-HIT (SUspect-SdecaY-Hdecay-InTerface)*, *Acta. Phys. Polon. B* **38** (2007) 635, arXiv: [0609292 \[hep-ph\]](https://arxiv.org/abs/0609292).

[109] P. Artoisenet, R. Frederix, O. Mattelaer and R. Rietkerk, *Automatic spin-entangled decays of heavy resonances in Monte Carlo simulations*, *JHEP* **03** (2013) 015, arXiv: [1212.3460 \[hep-ph\]](https://arxiv.org/abs/1212.3460).

[110] G. Belanger et al., *MicrOMEGAs 2.0: A Program to calculate the relic density of dark matter in a generic model*, *Comput.Phys.Commun.* **176** (2007) 367, arXiv: [0607059 \[hep-ph\]](https://arxiv.org/abs/0607059).

[111] G. Belanger et al., *micrOMEGAs: A Tool for dark matter studies*, *Nuovo Cim.* **C033N2** (2010) 111, arXiv: [1005.4133 \[hep-ph\]](https://arxiv.org/abs/1005.4133).

[112] W. Beenakker, M. Kramer, T. Plehn, M. Spira and P. M. Zerwas, *Stop production at hadron colliders*, *Nucl. Phys.* **B515** (1998) 3, eprint: [hep-ph/9710451](https://arxiv.org/abs/hep-ph/9710451).

[113] W. Beenakker et al., *Supersymmetric top and bottom squark production at hadron colliders*, *JHEP* **1008** (2010) 098, eprint: [arXiv:1006.4771 \[hep-ph\]](https://arxiv.org/abs/1006.4771).

[114] W. Beenakker et al., *Squark and gluino hadroproduction*, *Int. J. Mod. Phys.* **A26** (2011) 2637, arXiv: [1105.1110 \[hep-ph\]](https://arxiv.org/abs/1105.1110).

[115] Olivier Mattelaer, Eleni Vryonidou, *Dark matter production through loop-induced processes at the LHC: the s-channel mediator case*, *EPJC* (2015), arXiv: [1508.00564 \[hep-ph\]](https://arxiv.org/abs/1508.00564).

[116] M. Backovic et al., *Higher-order QCD predictions for dark matter production at the LHC in simplified models with s-channel mediators*, (2015), arXiv: [1508.05327 \[hep-ph\]](https://arxiv.org/abs/1508.05327).

[117] ATLAS Collaboration, *Electron identification measurements in ATLAS using $\sqrt{s} = 13$ TeV data with 50 ns bunch spacing*, ATL-PHYS-PUB-2015-041, 2015, URL: <https://cds.cern.ch/record/2048202>.

[118] ATLAS Collaboration, *Muon reconstruction performance of the ATLAS detector in proton–proton collision data at $\sqrt{s}=13$ TeV*, (2016), arXiv: [1603.05598 \[hep-ex\]](https://arxiv.org/abs/1603.05598).

[119] ATLAS Collaboration, *Muon reconstruction performance of the ATLAS detector in proton–proton collision data at $\sqrt{s} = 13$ TeV*, *Eur. Phys. J. C* **76** (2016) 292, arXiv: [1603.05598 \[hep-ex\]](https://arxiv.org/abs/1603.05598).

[120] ATLAS Collaboration, *Electron efficiency measurements with the ATLAS detector using the 2015 LHC proton–proton collision data*, ATLAS-CONF-2016-024, 2016, URL: <https://cds.cern.ch/record/2157687>.

[121] W. Lampl et al., *Calorimeter Clustering Algorithms: Description and Performance*, ATL-LARG-PUB-2008-002, 2008, URL: <https://cds.cern.ch/record/1099735>.

[122] ATLAS Collaboration, *Jet energy measurement with the ATLAS detector in proton–proton collisions at $\sqrt{s} = 7$ TeV*, *Eur. Phys. J. C* **73** (2013) 2304, arXiv: [1112.6426 \[hep-ex\]](https://arxiv.org/abs/1112.6426).

[123] M. Cacciari, G. P. Salam and G. Soyez, *The Anti- $k(t)$ jet clustering algorithm*, *JHEP* **0804** (2008) 063, arXiv: [0802.1189 \[hep-ph\]](https://arxiv.org/abs/0802.1189).

[124] M. Cacciari and G. P. Salam, *Pileup subtraction using jet areas*, *Phys. Lett. B* **659** (2008) 119, arXiv: [0707.1378 \[hep-ph\]](https://arxiv.org/abs/0707.1378).

[125] M. Cacciari, G. P. Salam and G. Soyez, *The Catchment Area of Jets*, *JHEP* **0804** (2008) 005, arXiv: [0802.1188 \[hep-ph\]](https://arxiv.org/abs/0802.1188).

[126] ATLAS Collaboration, *Performance of pile-up mitigation techniques for jets in pp collisions at $\sqrt{s} = 8$ TeV using the ATLAS detector*, *Eur. Phys. J. C* **76** (2016) 581, arXiv: [1510.03823 \[hep-ex\]](#).

[127] ATLAS Collaboration, *Jet energy measurement and its systematic uncertainty in proton–proton collisions at $\sqrt{s} = 7$ TeV with the ATLAS detector*, *Eur. Phys. J. C* **75** (2015) 17, arXiv: [1406.0076 \[hep-ex\]](#).

[128] M. Aaboud et al, *Jet energy scale measurements and their systematic uncertainties in proton-proton collisions at $\sqrt{s}=13$ TeV with the ATLAS detector*, (2016), arXiv: [1703.09665 \[hep-ex\]](#).

[129] ATLAS Collaboration, *Jet energy scale measurements and their systematic uncertainties in proton-proton collisions at $\sqrt{s}=13$ TeV with the ATLAS detector*, (2017), arXiv: [1703.09665 \[hep-ex\]](#).

[130] ATLAS Collaboration, *Characterisation and mitigation of beam-induced backgrounds observed in the ATLAS detector during the 2011 proton–proton run*, *JINST* **8** (2013) P07004, arXiv: [1303.0223 \[hep-ex\]](#).

[131] ATLAS Collaboration, *Selection of jets produced in 13 TeV proton–proton collisions with the ATLAS detector*, ATLAS-CONF-2015-029, 2015, URL: <https://cds.cern.ch/record/2037702>.

[132] ATLAS Collaboration, ‘Optimisation of the ATLAS b -tagging performance for the 2016 LHC Run’, tech. rep. ATL-PHYS-PUB-2016-012, CERN, 2016, URL: <http://cds.cern.ch/record/2160731>.

[133] ATLAS Collaboration, *Performance of b -Jet Identification in the ATLAS Experiment*, *JINST* **11** (2016) P04008, arXiv: [1512.01094 \[hep-ex\]](#).

[134] ATLAS Collaboration, *Commissioning of the reconstruction of hadronic tau lepton decays in ATLAS using pp collisions at $\sqrt{s} = 13$ TeV*, ATL-PHYS-PUB-2015-025, 2015, URL: <https://cds.cern.ch/record/2037716>.

[135] ATLAS Collaboration, *Reconstruction, Energy Calibration, and Identification of Hadronically Decaying Tau Leptons in the ATLAS Experiment for Run-2 of the LHC*, ATL-PHYS-PUB-2015-045, 2015, URL: <https://atlas.web.cern.ch/Atlas/GROUPS/PHYSICS/PUBNOTES/ATL-PHYS-PUB-2015-045>.

[136] ATLAS Collaboration, *Performance of missing transverse momentum reconstruction with the ATLAS detector in the first proton–proton collisions at $\sqrt{s} = 13$ TeV*, ATL-PHYS-PUB-2015-027, 2015, URL: <https://cds.cern.ch/record/2037904>.

[137] ATLAS Collaboration, *Expected performance of missing transverse momentum reconstruction for the ATLAS detector at $\sqrt{s} = 13$ TeV*, ATL-PHYS-PUB-2015-023, 2015, URL: <https://cds.cern.ch/record/2037700>.

[138] A. J. Barr, B. Gripaios and C. G. Lester, *Transverse masses and kinematic constraints: from the boundary to the crease*, *JHEP* **0911** (2009) 096, arXiv: [0908.3779 \[hep-ph\]](#).

[139] P. Konar, K. Kong, K. T. Matchev and M. Park, *Dark Matter Particle Spectroscopy at the LHC: Generalizing $M(T2)$ to Asymmetric Event Topologies*, *JHEP* **1004** (2010) 086, arXiv: [0911.4126 \[hep-ph\]](#).

[140] Y. Bai, H.-C. Cheng, J. Gallicchio and J. Gu, *Stop the Top Background of the Stop Search*, *JHEP* **1207** (2012) 110, arXiv: [1203.4813 \[hep-ph\]](https://arxiv.org/abs/1203.4813).

[141] C. G. Lester and B. Nachman, *Bisection-based asymmetric M_{T2} computation: a higher precision calculator than existing symmetric methods*, *JHEP* **1503** (2015) 100, arXiv: [1411.4312 \[hep-ph\]](https://arxiv.org/abs/1411.4312).

[142] C. G. Lester and D. J. Summers, *Measuring masses of semi-invisibly decaying particles pair produced at hadron colliders*, *Phys. Lett. B* **463** (1999) 99, arXiv: [hep-ph/9906349 \[hep-ph\]](https://arxiv.org/abs/hep-ph/9906349).

[143] A. Hoecker et al., *TMVA - Toolkit for Multivariate Data Analysis*, *PoS ACAT* (2007) 040, arXiv: [physics/0703039 \[PHYSICS\]](https://arxiv.org/abs/physics/0703039).

[144] H. An and L.-T. Wang, *Opening up the compressed region of top squark searches at 13 TeV LHC*, *Phys. Rev. Lett.* **115** (2015) 181602, arXiv: [1506.00653 \[hep-ph\]](https://arxiv.org/abs/1506.00653).

[145] S. Macaluso, M. Park, D. Shih and B. Tweedie, *Revealing Compressed Stops Using High-Momentum Recoils*, *JHEP* **03** (2016) 151, arXiv: [1506.07885 \[hep-ph\]](https://arxiv.org/abs/1506.07885).

[146] P. Jackson, C. Rogan and M. Santoni, *Sparticles in motion: Analyzing compressed SUSY scenarios with a new method of event reconstruction*, *Phys. Rev. D* **95** (2017) 035031, arXiv: [1607.08307 \[hep-ph\]](https://arxiv.org/abs/1607.08307).

[147] ATLAS Collaboration, ‘Search for top squarks in final states with one isolated lepton, jets, and missing transverse momentum in $\sqrt{s} = 13$ TeV pp collisions with the ATLAS detector’, tech. rep. ATLAS-CONF-2016-050, CERN, 2016, URL: <https://cds.cern.ch/record/2206132>.

[148] ATLAS Collaboration, *Observation and measurement of Higgs boson decays to WW^* with the ATLAS detector*, *Phys. Rev. D* **92** (2015) 012006, arXiv: [1412.2641 \[hep-ex\]](https://arxiv.org/abs/1412.2641).

[149] ATLAS Collaboration, *Jet Calibration and Systematic Uncertainties for Jets Reconstructed in the ATLAS Detector at $\sqrt{s} = 13$ TeV*, ATL-PHYS-PUB-2015-015, 2015, URL: <https://cds.cern.ch/record/2037613>.

[150] ATLAS Collaboration, *Calibration of b -tagging using dileptonic top pair events in a combinatorial likelihood approach with the ATLAS experiment*, ATLAS-CONF-2014-004, 2014, URL: <https://cds.cern.ch/record/1664335>.

[151] ATLAS Collaboration, *Calibration of the performance of b -tagging for c and light-flavour jets in the 2012 ATLAS data*, ATLAS-CONF-2014-046, 2014, URL: <https://cds.cern.ch/record/1741020>.

[152] A. L. Read, *Presentation of search results: the CL_s technique*, *Journal of Physics G: Nuclear and Particle Physics* **28** (2002) 2693, URL: <http://stacks.iop.org/0954-3899/28/i=10/a=313>.